UNIVERSIDADE FEDERAL DE MINAS GERAIS
Programa de Pós-Graduação em Engenharia Metalúrgica, Materiais e de Minas

Tese de Doutorado

Mecanismo Inédito de Imobilização de Arsênio Baseado em Agregação Orientada de Nanopartículas Cristalinas de (Hidr)óxidos de Ferro e Alumínio:
Evidências por Microscopia Eletrônica de Transmissão

Autor: Erico Tadeu Fraga Freitas
Orientadora: Professora Virginia S. T. Ciminelli
Co-orientador: Professor Massimo Gasparon
Co-orientador: Professor Luciano A. Montoro

Junho/2017

Erico Tadeu Fraga Freitas

Mecanismo Inédito de Imobilização de Arsênio Baseado em Agregação Orientada de Nanopartículas Cristalinas de (Hidr)óxidos de Ferro e Alumínio:
Evidências por Microscopia Eletrônica de Transmissão

Novel Mechanism of Arsenic Immobilization Based on Oriented Aggregation of Crystalline Nanoparticles of Iron- and Aluminium- (hydr)oxides:
Transmission Electron Microscopy Evidences

Tese de Doutorado apresentada ao Programa de Pós-Graduação em Engenharia Metalúrgica, Materiais e de Minas da Universidade Federal de Minas Gerais, como requisito parcial para obtenção do grau de Doutor em Engenharia Metalúrgica, Materiais e de Minas.

Área de concentração: Ciência e Engenharia de Materiais

Orientadora: Prof^{a}. Virginia S. T. Ciminelli
Co-orientador: Prof. Massimo Gasparon
Co-orientador: Prof. Luciano A. Montoro

Belo Horizonte
Universidade Federal de Minas Gerais
Escola de Engenharia da UFMG
2017

Dedicatória

Dedico este trabalho à minha esposa, Aline,
Aos meus fillhos, Júlia e Sávio. Amo muito vocês!

AGRADECIMENTOS

Agradeço a Deus por Jesus Cristo, por me dar uma “fé que pensa, e uma razão que crê”, e por minha família. À minha esposa, que sempre me auxilia com suas opiniões, críticas, sugestões, comentários e ponderações frente às decisões que a mim cabem tomar. Por seu suporte em todos os momentos necessários. Aline, amo muito você! Sou grato por meus filhos. Espero que um dia eles leiam estes agradecimentos e possam ter me tido como exemplo em suas vidas. À minha mãe, Rita, que sempre foi exemplo de esforço, perseverança e dedicação. Também quero mencionar a memória de meu pai, Ulisses, falecido durante meu doutoramento, no ano em que estive fora do País, realizando estágio de doutorado sanduíche. Não tive a honra de sepultá-lo, mas o menciono aqui para registrar sua memória.

Quero aqui expressar minha gratidão a todos aqueles que fizeram parte deste trabalho, e àqueles que de algum modo me auxiliaram até a finalização desta etapa. À minha orientadora, Professora Virginia Ciminelli pela oportunidade de realizar este doutorado e pelo constante apoio e suporte, pelos ricos momentos de aprendizado proporcionados. Aos meus coorientadores, Professor Luciano Montoro, pelas ricas discussões e contribuições para este trabalho, e Professor Massimo Gasparon, pela presença constante e eficiente durante o período de doutoramento, principalmente durante o estágio de doutorado sanduíche na Austrália. Pela hospitalidade, pelas caronas para a universidade, pela amizade e ricas contribuições para esta pesquisa.

Registro meu agradecimento aos colegas e à diretoria do Centro de Microscopia da UFMG (CM-UFMG). Agradeço ao Douglas Miquita, quem me iniciou em microscopia eletrônica de transmissão, e pelo suporte dado assumindo a maior parte das atividades relacionadas ao microscópio nos momentos que me foi necessário ausentar do CM-UFMG em função do doutorado. À Raque Maria pelo apoio na preparação de amostras. À direção, na pessoa do Professor Wagner Nunes Rodrigues, pelo apoio e incentivo na realização desta pesquisa na condição de servidor-estudante.

Sou grato a Claudia Caldeira pelas orientações técnicas durante os experimentos de sínteses realizados, bem como pelo auxílio em análises químicas. À Maria Dantas (Sica) pelo suporte nas análises de Raman. À Ilda Batista, pelo auxílio no laboratório, bem como por sua excelência na realização de medidas de área superficial. Expresso também minha gratidão a Christina Salvador e Glastone da Cruz, pelo apoio administrativo, e ao pessoal do Laboratório de Análise Químicas, Patrícia e Felipe, pela postura profissional e excelência na realização das medidas de ICP-OES. Não poderia deixar de agradecer à Gabriela Cordeiro, quem me introduziu neste campo de pesquisa junto à Professor Virgínia Ciminelli. À Daphne Chiara, Tassio Gontijo, e Clauson Souza, os quais, de várias formas, me auxiliaram em laboratório durante o doutorado.

Agradeço ao Centro de Microscopia da UFMG (CM-UFMG), Brasil, ao Laboratório Nacional de Nanotecnologia (LNNano/CNPEM), Brasil, ao *International Iberian Nanotechnology Laboratory* (INL), Portugal, e ao *Center for Microscopy and Microanalysis* (CMM) da *University of Queensland*, Austrália, pela instrumentação em microscopia eletrônica de transmissão disponibilizadas.

Agradeço a Kinross Brasil Mineração por fornecer as amostras de latossolo usadas nesta pesquisa.

Agradeço ao Curso de Pós-Graduação em Engenharia Metalúrgica e de Minas, às agências financiadoras: CNPq, INCT-Acqua, Fapemig, e CAPES pelo suporte e apoio na realização desta pesquisa.

SUMMARY

CHAPTER 4. Arsenic entrapment by nanocrystals of Al-magnetite: the role of Al in crystal growth and As retention 58

APPENDICES

LIST OF FIGURES

LIST OF TABLES

LIST OF ACRONYMS

ADF: Annular Dark Field
AMD: Acid Mine Drainage
BF: Bright Field
CBED: Convergent Beam Electron Diffraction
CCD: Charge Coupled Device
EDS: Energy Dispersive X-Ray Spectroscopy
EELS: Electron Energy Loss Spectroscopy
EFTEM: Energy Filter Transmission Electron Microscopy
ELNES: Energy-Loss Near Edge Structure
EXAFS: Extended X-ray Absorption Fine Structure
FEG: Field Emission Gun
FFT: Fast Fourier Transform
FOLZ: First Order Laue Zone
HAADF: High Angle Annular Dark Field
HG: Hydrate generation
HR-STEM: High Resolution Scanning Transmission Electron Microscopy
HRTEM: High Resolution Transmission Electron Microscopy
MC: Mesocrystal
MD: Microdiffraction
NBD: Nano Beam Electron Diffraction
OA: Oriented Aggregation
OAN: Oriented Aggregates of Nanoparticles
OR: Ostwal Ripening
TEM: Transmission Electron Microscopy or Transmission Electron Microscope
SAD: Selected Area Electron Diffraction
SADP: Selected Area Electron Diffraction Pattern
SI: Spectrum Image
SOLZ: Second Order Laue Zone
STEM: Scanning Transmission Electron Microscopy or Scanning Transmission Electron Microscope

WRL: White line Ratio

XRD: X-Ray Diffraction

XANES: X-ray Asorption Near Edge Structure

XAS: X-Ray Absorption Spectroscopy

ICP-OES: Inductively Coupled Oasma Optical Emission Spectrometry

ZA: Zone Axis

ZLP: Zero Loss Peak

ZOLZ: Zero Order Laue Zone

RESUMO

Hidróxidos e óxidos de ferro e alumínio têm um papel importante na imobilização de arsênio no meio ambiente devido à sua capacidade de fixação do arsênio por adsorção ou coprecipitaçao. Entretanto, os mecanismos responsáveis pela imobilização de arsênio em longo prazo nos (hidr)óxidos de ferro e alumínio, as transformações de fase e seu efeito na partição final do arsênio e, ainda, o papel do alumínio em todas as etapas do processo ainda não foram elucidadas, sendo objeto do presente trabalho. Foram investigadas amostras de latossolos ricos em alumínio e ferro, amostras sintetizadas de goethita (α-FeOOH), magnetita (Fe_3O_4) e ferrihidrita ($Fe_2O_3.0.5H_2O$), contendo diferentes teores de alumínio, e envelhecidas por até 120 dias em temperatura ambiente. Os resultados demonstram que a presença de alumínio na estrutura cristalina de ferrihidrita (i) retarda eventuais transformações e estabiliza esta fase; (ii) favorece o crescimento de mesocristais por agregação orientada de nanopartículas; e (iii) aumenta a densidade de carga média dos átomos de ferro na rede cristalina, o que pode favorecer a adsorção de anions. As fases contendo arsênio são predominantemente agregados orientados de nanopartículas (AON), onde o arsênio predomina nos interstícios das nanopartículas que formam os mesocristais de ferrihidrita. O teor de arsênio associado a ferrihidrita pura foi 5,4 ± 0,6 wt% (54.000 – 60.000 mg kg^{-1}) enquanto a amostra de ferrihidrita com maior teor de aumínio (21 ± 4% mol mol^{-1}) apresentou 6,9 ± 0,3 wt% de arsênio (66.000 – 72.000 mg kg^{-1}). Nos latossolos, o arsênio mostra-se predominantemente associado a AON de Al-hematita e em concentrações de até 1,6 ± 0,5 wt% de arsênio (11.000 – 21.000 mg kg^{-1}). Observa-se uma correlação positiva entre alumínio e arsênio na Al-hematita nanoestruturada. O arsênio, em concentrações de até 1,10 wt% (11.000 mg kg^{-1}), foi observado em AON Al-magnetita em amostras sintetizadas. O teor de arsênio nas amostras de Al-magnetita é relativamente maior que em magnetita pura e diminui com o aumento da substituição de alumínio por ferro na faixa (Al/(Al+Fe)) de 3,5 a 11,4% mol mol^{-1}, possivelmente devido ao aumento de sítios Fe^{2+} em relação a Fe^{3+} substituídos por Al^{3+}. Isso pode ter contribuído para enfraquecer a interação entre ferro e anions de arsênio. Agregados orientados de nanopartículas de Al-goethita contendo 13 a 32% mol mol^{-1} de alumínio apresentaram concentrações de arsênio aproximadamente igual ou inferior a 0,1 wt%. O mecanismo proposto de incorporação de arsênio em (hidr)óxidos bimetálicos de alumínio e ferro nanoestruturados basea-se em um processo não-clássico de crescimento de cristais por agregação orientada. O arsênio adsorvido em ferrihidrita é aprisionado por agregação orientada das nanopartículas. A fração de arsênio não dessorvida é irreversivelmente incorporada na estrutura à medida que os agregados passam a formar estruturas mais ordenadas. A combinação de diversas técnicas de microscopia eletrônica de transmissão permitiu investigar amostras altamente heterogêneas, típicas de solo, em escala nanométrica, bem como amostras sintetizadas, e, assim, trazer um entendimento mais aprofundado do mecanismo de incorporação de arsênio em materiais nanoestruturados. Este mecanismo, mostrado pela primeira vez neste trabalho, explica a imobilização do metalóide em processos de longo prazo com amostras de relevância ambiental, e amplia o entendimento da estabilidade de altos teores de arsênio em fases cristalinas de (hidr)óxidos bimetálicos de alumínio e ferro. Este entendimento pretende auxiliar no desenvolvimento de tecnologias de remediação para fixação de As águas residuais.

ABSTRACT

Iron and aluminium (hydr)oxides play a major role in arsenic fixation in the environment due to their capacity for arsenic uptake by adsorption or co-precipitation. Nevertheless, the mechanisms responsible for the arsenic long-term immobilization in Al- and Fe- (hydr)oxides, the phase transformations and their effects on arsenic partition, and the role of aluminium in the all steps of these processes are not yet elucidated, being studied in the present work. The investigated samples are Al- and Fe-rich Oxisols, synthesized Al-free and Al-containing goethite (α-FeOOH), magnetite (Fe_3O_4) and ferrihydrite ($Fe_2O_3.0.5H_2O$), aged for up 120 days at ambient temperature. The results showed that the presence of aluminum into the crystal structure of ferrihydrite (i) retards further phase transformations, thus stabilizing the original phase; (ii) favours the formation of mesocrystals produced by the mechanism of oriented aggregation and (iii) increases the average charge density of iron in the crystal lattice, which may favour anions adsorption. The As-containing phases are predominantly oriented aggregates of nanoparticles (OAN), where the arsenic is mainly found in the interstices of nanoparticles-building-units of ferrihydrite mesocrystals. The arsenic content associated to pure ferrihydrite was 5.4±0.6 wt% As (54.000 – 60.000 mg kg^{-1}). The ferrihydrite sample with larger aluminium substitution (21±4% mol mol^{-1}) presented 6.9±0.3 wt% As (66.000 – 72.000 mg kg^{-1}). In the Oxisols, the arsenic is predominantly associated to OAN of Al-hematite (α-Fe_2O_3), in concentration of 1.6±0.5 wt% As (11,000 – 21,000 mg kg^{-1}). A positive correlation between arsenic and aluminium was observed in nanostructured Al-hematite. The arsenic concentration up to 1.10 wt% As (11,000 mg kg^{-1}) was observed in OAN of Al-magnetite. The arsenic content in Al-magnetite is relatively larger than in pure magnetite, and decreases with an increase of Al-for-Fe substitution in the range (Al/(Al+Fe)) 3.5 to 11.4% mol mol^{-1}, likely due to the increase of Fe^{2+} sites relatively to Fe^{3+} substituted by Al^{3+}. This might contribute to weaken the interaction between arsenic anions and iron. Oriented aggregates Al-goethite nanoparticles with 13 to 32% mol mol^{-1} Al presented arsenic content approximately equal or less than 0.1 wt%. The proposed mechanism for arsenic incorporation in nanostructured Al-Fe-(hydr)oxides relies on a non-classical aggregation based crystal growth. The adsorbed arsenic on ferrihydrite is trapped upon the oriented aggregation of nanoparticles. The non-desorbed arsenic is irreversibly incorporated in the net-structure as the aggregates evolve to a more ordered structure. The combination of several transmission electron microscopy techniques made possible the investigation of markedly heterogeneous samples, typical of soils, at nanometre scale, thus bringing about a novel understanding of the mechanism for As incorporation in nanostructured materials. This mechanism, shown for the first time in this work, accounts for the process of long-term immobilization of arsenic in samples of environmental concern and highlights arsenic stability within nanostructured metal oxides. This understanding intends to help further developments of remediation technologies for arsenic uptake from wastewater.

CHAPTER 1. Introduction

1.1. Arsenic in the environment

Arsenic (As) is a metalloid of environmental concern. The toxicity of As depends on its predominant species, its content and mobility in different solid matrices – mainly to water environments, the main source for human and biota exposure – and finally on its bioavailability. The main sources of arsenic in soils are the parent rock. In soil, arsenic is often found in association with iron (Fe) and aluminium (Al) (hydr)oxides and the background concentrations can range from as low as 0.1 mg kg^{-1} to as high as 55 mg kg^{-1} Nevertheless, arsenic concentrations much higher than the baseline values are found where additional inputs are derived by anthropogenic activities The main anthropogenic sources for As exposure include mining activities, smelting, fossil-fuel combustion products, pesticides and phosphate fertilizers (Smedley and Kinniburgh, 2002). The concentration of As in soil near mineralized areas can be much larger, up to 8,000 mg kg^{-1} (Ciminelli et al. 2017). In soil affected by mining activities, the high concentrations are due to the primary sulfide sources as well as secondary iron arsenates and iron oxides formed by oxidation of the ore constituents. The gold extraction processes may produce large amount of As residues from which the metalloid can be mobilised to aqueous phase through the oxidation of minerals such as arsenopyrite (FeAsS). Therefore, arsenic should be immobilised and carefully disposed to avoid contamination of soil and groundwater. In drinking water, the provisional guideline value for As concentration established by the World Health Organization is 10 μg L^{-1}. This limit could be even lower as there is uncertainty in the risk assessment of low concentrations of arsenic in drinking water (WHO 2017). Nevertheless, there are practical difficulties either on determining As concentration in the range 1 – 10 mg kg^{-1} or in removal of arsenic below 10 mg kg^{-1}. Efficient remediation technologies for water treatment are then needed to comply with increasingly stringent guidelines.

1.2. Arsenic immobilization in Al-Fe-(hydr)oxides

The immobilization of As released by geogenic and anthropogenic sources is a major environmental concern due to the toxicity of this metalloid, which depends on the As species and their bioavailability in different matrices (Smith et al. 1998, 2008; Smedley and Kinniburgh 2002). A number of studies have investigated the processes of immobilization of this metalloid in iron or aluminum (hydr)oxides (Ladeira and Ciminelli 2004; Ona-Nguema et al. 2005, 2010; Violante et al. 2006, 2007; Morin et al. 2008, 2009; Duarte et al. 2012; Bolanz et al. 2013; Guo et al. 2013; Das et al. 2014; Doerfelf et al. 2015) or in mixed Al-Fe-(hydr)oxides (Masue et al. 2007; Violante et al. 2009; Silva et al. 2010; Adra et al. 2013, 2016; Freitas et al. 2015). Among Fe-(hydr)oxides, hematite has been widely applied in studies of arsenic immobilization by adsorption, precipitation or co-precipitation (Mohan and Pittman Jr. 2007; Das et al. 2011, 2014a; Cao et al. 2012; Hua et al. 2012; Carabante et al. 2014; Guo et al. 2016). Its effective performance and environmental friendly properties (Novoselova 2016) make hematite suitable for arsenic removal from polluted water. Hematite along with other Fe-(hydr)oxides, such as goethite, or their precursor ferrihydrite, are preferred for water treatment because metalloids such as arsenic can efficiently adsorb on and co-precipitate with these materials.

Magnetite sorbents are also materials of interest due to their removal capacity of trace contaminants from aqueous systems combined with the magnetic properties that helps the following stage of solid-liquid separation (Silva et al. 2012). Despite these recent advances, there is relatively little information on As-bearing Al-magnetite compared to other iron oxides. Al-free magnetite NPs have been shown to have high As adsorption capacity (Morin et al. 2009; Ona-Nguema et al. 2010; Akin et al. 2012; Farrell et al. 2014; Türk and Alp 2014; Liu et al. 2015) and are commonly used for the treatment of polluted water. Al-bearing magnetite-based materials have been proposed as new types of adsorbents for As removal from contaminated water (Zhang et al. 2012; Pizarro et al. 2015; Moradlou et al. 2016). In general, the increased loading capacity onto mixed Al- and Fe- (hydr)oxides has been ascribed to increased surface area due to the presence of Al. The effect of increasing amounts of Al over As sorption, however, is still debated.

The nano-adsorbents made of Fe-(hydr)oxides are relatively low-cost materials and show high efficient capacity for heavy metals uptake from wastewater (Smith et al. 1998; Smedley and Kinniburgh 2002; Hua et al. 2012; Carabante et al. 2014; Adeleye et al. 2016). The main concern about nano-adsorbents relies on the likely toxicity and environmental fate of nanomaterials. The toxicity of metal oxides' nanocomposites increases with their molar mass, with the exception for hematite out of other tested transition metal oxides. This is partly attributed to the fact that hematite is not significantly dissolved in cell culture system (Huang et al. 2010).

Several attempts have been made recently to enhance the As adsorption capacity on either synthesised Al-free and Al-bearing Fe-(hydr)oxides (Masue et al. 2007; Silva et al. 2010; Tang et al. 2011; Cao et al. 2012; Feng et al 2012; Adra et al. 2013, 2016) or from Fe-rich waste materials (Akin et al. 2012; Carabante et al. 2014), with the common understanding that As removal, especially from dilute solution, will rely primarily on adsorption. In addition, studies on co-precipitation of As with Fe (Violante et al. 2007; Pantuzzo et al. 2008; Wang et al. 2015) and along with Al and Fe (Violante et al. 2009) have been carried out to elucidate this mechanism of As fixation. Evidence for the stabilization of As-bearing ferrihydrite is shown in Wang et al. (2015) by the inhibition of thermal phase transformation towards hematite, when increasing the co-precipitates' As/Fe molar ratio from 0 to 0.5 mol mol^{-1}. The retarding in phase transformation from As-Al-Fe co-precipitates formed at circum-neutral pH was previously reported by Violante et al. (2009). Based on their data from arsenate removal by sorption of phosphate onto co-precipitates, as well as the X-ray photoelectron spectroscopy measurements, these authors suggested a partial incorporation of As(V) into the short-range ordered co-precipitates (mainly ferrihydrite) formed at As/(Al+Fe) molar ratios 0.01 and 0.1 mol mol^{-1}. Indeed, the maximum amount As(V) desorbed by phosphate was 23% (out of the total initial arsenate content) for co-precipitates formed at pH 4 – 10 at As/(Al+Fe) molar ratio of 0.1 mol mol^{-1}.The contribution of arsenate adsorption on co-precipitation experiments was also studied by Pantuzzo et al. (2008) by using a selective extraction protocol to quantify sorbed arsenate in synthetic Fe-As co-precipitates. The authors reported an increase in the amount of As(V) adsorption relatively to the total uptake (based on extraction with phosphate solutions) from 6% to

84% at pH 1.5 and 8, respectively. A nearly constant amount of As(V) adsorption (15 – 20%) was observed when decreasing the As/Fe molar ratio from 1 to 0.25 mol mol^{-1} at pH 4. These findings led Pantuzzo et al. (2008) suggesting the improvement of As removal from aqueous solution and its stability in the host phases may depend on the nature of the precipitates (composition, crystallographical phase, morphology, and grain size) rather than As fixation by adsorption/co-precipitation. Nevertheless, none of these works have proposed a different mechanism dependent on the precipitates' nature or phase transformation upon aging.

The adsorption/coprecipitation of As on/with Fe-(hydr)oxides or Al-(hydr)oxides is well studied (Ladeira and Ciminelli, 2001; Ona-Nguema et al. 2005, 2010; Violante et al. 2006, 2007; Wang et al. 2008; Morin et al. 2009; Tang et a. 2011; Cao et al. 2012; Feng et al. 2012; Duarte et al. 2012b; Guo et al. 2013), but the combination of Al and Fe in adsorption and co-precipitation experiments for waste water treatment has opened a discussion on the role of Al in such bi-metal (hydr)oxides when applied for As removal. Mixed Al-Fe-(hydr)oxides have been suggested as successful candidates for the long-term As immobilization due to the effects of Al-for-Fe substitution in these phases, as aluminium-bearing Fe-(hydr)oxides are ubiquitous in rocks, soils and acid mine drainage (AMD) water, and are also known to favour stable alpha- over gamma-phases (Taylor and Schwertmann 1978). The presence of Al may give more stability to Al-substituted Fe-(hydr)oxides such as ferrihydrite, goethite, hematite, and magnetite (Cornell and Schwertmann 2003), slowing down further phase transformation. The properties of mixed Al-Fe-(hydr)oxides have been explored in investigations on As immobilization and in water treatment. The works of Ladeira et al. (2002) and Ladeira and Ciminelli (2004), for instance, showed evidences for the higher efficiency in arsenic uptake by Al- and Fe- rich Oxisol, compared to other tested soils to be selected and used as liner for chemical barrier in tailings impoundments in a gold mine plant in Paracatu, Minas Gerais state, Brazil. The selected Oxisol was then used to seal facilities for the long-term disposal of As-rich sulfide tailings in this mine plant. After 10 years of disposal, these facilities were excavated to reprocess the tailings for gold extraction, and at that time samples from both aged tailings and Oxisol liners recovered for analysis (Duarte et al. 2012a; Silva et al. 2013). It was found that As(V) was the main species present in the aged tailings As(V), mainly as arsenopyrite, and As(V) on aged Oxisol (Duarte et al. 2012a), what indicated no significant oxidation of pyrite/arsenopyrite concentrates over the period of long-term disposal. A selection extraction protocol was applied in the analysis of the Oxisol liner, and it was shown that the majority of As(V) (60 – 69 % out of total arsenate measured) is associated to crystalline Al and Fe phases (Silva et al. 2013). However, the As-bearing crystalline Al- and Fe- (hydr)oxide phases in Oxisol had not been identified. The aged Oxisol liner samples are investigated in this present work and the results will be shown and discussed.

The understanding on the role of Al in As uptake by Al-containing Fe-(hydr)oxides is crucial to develop remediation technologies for As immobilization by such mixed phases. Nevertheless, there are few studies available in the up-to-date literature reporting investigations on either adsorption or co-precipitation of arsenic by mixed Al-Fe-(hydr)oxides (Masue et al. 2007; Violante et al. 2009; Silva et a. 2010; Adra et al. 2013, 2016). Investigations on As adsorption onto Al-substituted goethite were undertaken by Silva et al. (2010). The high loading capacity of Al-goethite with respect to As(V) relative to pure goethite and hematite was ascribed to increased surface area of the former. Masue et al. (2007) and Adra et al. (2016) reported different findings in similar investigations on As(V) adsorption onto Al-bearing ferrihydrite at neutral pH. Adra et al. (2016) observed an increase of As(V) sorption densities when increasing Al:Fe molar ratio, whilst Masue et al. (2007) reported no significant change in As(V) adsorption when increasing Al:Fe molar ratio up to 20% mol mol^{-1}. As for arsenite (As(III)) sorption, Masue et al. (2007) and Adra et al. (2016) found similar results, reporting a decrease of As(III) adsorption when increasing Al:Fe molar ratio. In these studies, however, Masue et al. (2007) and Adra et al. (2016) have not investigated the behaviour of adsorbed As over the time. To the authors knowledge no up-to-date literature have reported the partitioning of adsorbed arsenic onto the Al-bearing ferrihydrite and its fate upon ageing at neutral pH and ambient temperature. Moreover, the detailed ageing/recrystallization mechanisms taking place following the initial adsorption/co-precipitation of As and the role of Al in these processes remain to be fully understood. In addition, the mechanism of As fixation in these bi-metal (hydr)oxides in the environment and its fate during the transformation of the As-host phases lack understanding.

1.3. The incorporation of As into the Fe-Al-(hydr)oxides

Arsenic adsorbed onto, or co-precipitated with, metal (hydr)oxides may incorporate into the structure of the precipitates and into the crystal products upon further phase transformation. There are few investigations in the up-to-date literature, including ours, that have shown evidences for the As incorporation in the structure of the host phases, following an initial adsorption/co-precipitation step (Violante et al. 2009; Bolanz et al. 2013; Das et al 2014b; Freitas et al. 2015, 2016). Violante et al. (2009) reported that As(V) is mainly incorporated in short-range ordered As-Al-Fe co-precipitates such as ferrihydrite based on indirect experimental evidences. To assesss the chemical composition of co-precipitates, Violante et al. (2009) treated samples to solubilise As, Al and Fe with both 6 mol L^{-1} HCl and 0.2 mol L^{-1} oxalic acid/ammonium oxalate at pH 3 to determine the amount of ferrihydrite. Their data show a slightly decrease in the amount of As(V) in ferrihydrite as samples aged, suggesting the incorporation of arsenate. The decrease in As(V) concentration at the surface of co-precipitated products was followed by an increase in pH and ageing time (Violante et al. 2009), which the authors attributed to a decrease of the solids' surface area (from 192 to 135 m^2 g^{-1}) as they evolved to a more ordered structure. The work of Das et al. (2014b) showed a decrease from 1.48 to 0.51 mg L^{-1} of aqueous As(V) when ageing ferrihydrite suspensions at pH ~10 and 75 ºC for 7 days. Das et al. (2014b) argued that the reduction in the concentration of aqueous arsenate in suspension could not be explained by adsorption of As(V) onto the formed hematite at the end of their experiments, because the specific surface area of precipitates decreased from 241 to 112 m^2 g^{-1} as sample aged. It is reported that 55% of ferrihydrite transformed into hematite (Das et al. 2014b). Their analysis from the extended X-ray absorption fine structure (EXAFS) spectra for samples at days 0 and 7 indicated an additional As-Fe shell (coordination number CN = 1.1, and bond distance $R = 2.83 \pm 0.02$ Å) for the sample at day 7 compared to sample at day 0. Das et al. (2014b) then concluded that the difference in the coordination environment of As(V) in sample at day 7 is an evidence for the incorporation of As(V) into the formed hematite by both bidentate-mononuclear and bidentate-binuclear complexes. However, this is not a conclusive evidence, as the adsorption of As(V) onto the formed hematite could not be dismissed. Indeed, the above bond distance and coordination number correspond to the coordination environment of As(V) adsorbed onto hematite (CN = 0.9 and R = 2.84 Å) shown in the same work for a stand-alone As(V)-adsorbed hematite sample (Das et al. 2014b). As both ferrihydrite and hematite nanoparticles coexisted in Das et al.' sample at day 7, and both phases are not likely separated from each other (what could be easily demonstrated by transmission electron microscopy – TEM), the further adsorption of aqueous As(V) onto both phases upon ageing suspension could not be excluded.

Bolanz et al. (2013) studied two series of As(V)-adsorbed ferrihydrites aged for 16 days at 70 ºC (series 1), and for 7 days at 200 ºC (series 2). After precipitation of ferrihydrite, As(V) stock solution was added to suspensions to have initial As/Fe molar ratios 0, 0.005, 0.015 and 0.045 mol mol^{-1} (in series 1), and equal 1 mol mol^{-1} (in series 2). The removal of the remaining ferrihydrite and excess As(V) onto precipitates is reported to be achieved by washing samples with 15% HCl (non-selective extraction) solution for 2 hours (Bolanz et al. 2013), although no further evidences were shown for the complete ferrihydrite and adsorbed As(V) removal. Indeed, other precipitates apart from hematite can be seen in the TEM micrograph published in Bolanz et al. (2013). Evidences for the incorporation of the As(V) in the formed hematite is shown by the increase of the lattice parameter c (from 1.37690 ± 0.00007 to 1.37943 ± 0.00005 nm) with the increase As content (from 0 to 1.80 wt%) in hematite crystals (Bolanz et al. 2013). The lattice parameter refinement was done by Rietveld method, and the As(V) quantified by TEM energy dispersive X-ray (TEM-EDX) spectroscopy. These estimated standard deviations for the lattice paramters based on Rietveld refinement may be underestimated though, if they were measures of accuracy only based on statistical dispersions (Scott 1983; Berar and Lelann 1991).

By combining XRD, TEM, and XAS analyses and theoretical modelling, Bolanz et al. (2013) proposed a mechanism for As incorporation where clusters of angelellite ($Fe_4As_2O_{11}$) along (210) plane may have intergrown epitaxialy onto the (0001) plane of hematite. However, this mechanism lacks evidence as their TEM and XRD data do not support the presence of angelellite. Furthermore, the EXAFS spectra for As-bearing hematite, produced by ageing As(V)-adsorbed ferrihydrite, shown in Bolanz et al. (2013) and Das et al. (2014b) are in aggrement, but there is a relative shift of about 0.4 Å between them, what can be attributed to the fact that these spectra are uncorrected for phase shift. Moreover, the X-ray absorption spectroscopy (XAS) measurement of one single nanocrystalline phase in a non-homogeneous sample is unfeasible, as the XAS lateral resolution is about 30 nm, if the synchrotron based radiation is used (Egerton 2008). Therefore, the XAS data and EXAFS spectra published by Bolanz et al. (2013) and Das et al (2014b) are probably a combination of signals from As(V) adsorbed onto both ferrihydrite and on the co-existed formed hematite. Another hypothesis, not arisen neither by Bolanz et al. (2013) nor Das et al. (2014b), but in this present work, is that the hematite may have formed by the aggregation based crystal growth (Cölfen and Antonietti 2008) of As(V)-adsorbed ferrihydrite.

The non-classical oriented aggregation crystal growth process starts with oriented attachment events of primary nanoparticles. These events lead to the formation of larger mesocrystals that evolve to oriented aggregates (Niederberger and Cölfen 2006; Cölfen and Antonietti 2008; De Yoreo et al. 2015) and may undergo phase transformation. The mesocrystals are superstructures consisted of self-assembly oriented nanoparticles (buiding units) crystallographically aligned (Niederberger and Cölfen 2006). The mesocrystals may be kinectically stabilised by adsorbates and/or fuse to form single-crystals-like oriented aggregates (De Yoreo et al. 2015). The driving force for the oriented aggregation is the energy change following an oriented attachement. The more negative the energy difference upon an attachment on a particular (hkl) surface, the higher the driving force (Zhang and Banfield 2012).

The pioneering work of Waychunas et al. (2005) had pointed out a likely remediation process for contaminants scavenging based on aggregation of nanoparticles. Potential structural incorporation of equeous Zn(II) and Cu(II) into the structure of crystal products from aged iron oxyhydroxides, for example, has been shown by the aggregation-mediated crystal growth of primary metal-adsorbed nanoparticles

(Stegemeier et al. 2015; Dale et al. 2015). Nevertheless, the mechanism for the scavenging of aqueous arsenic based on oriented aggregation of Al- and Fe-(hydr)oxides has not been proposed or shown so far, being demonstrated in this present work for the first time, with the help of high spatial resolution (scanning) TEM techniques combined with EDX and electron energy-loss (EEL) spectroscopies. In the present work, TEM evidences for the As(V) incorporation in natural nanostructured Al-hematite identified in environmental samples (Freitas et al. 2015), and into Al-magnetite and Al-goehite co-precipitated in the presence of As(V) (Freitas et al. 2016) will be shown. The proposed mechanism for arsenate incorporation into these Al-bearing Fe-(hydr)oxide crystalline phases will be discussed.

1.4. Relevance and Objective

The present thesis reports a careful investigation of As-bearing natural and synthetic samples of environmental concern. The natural samples are from Al- and Fe- rich Oxisol layers used as chemical barrier in tanks for the disposal of As-rich sulfide tailings in a gold mine plant in Paracatu city, northwestern Minas Gerais state, Brazil. The Oxisol liners had been exposed to the As tailings for 10 to 15 years. After this period, the tailings were reprocessed for gold extraction and the Oxisol liner samples recovered for analysis. It had been demonstrated the majority (> 60%) of arsenic (As(V)) found in the Oxisol samples is strongly bonded to crystalline phases of Al-Fe-(hydr)oxides (Duarte et al. 2012a; Silva et al. 2013), but the mechanism responsible for the long-term As immobilization in the crystalline phases remained to be understood. This mechanism was investigated in this present work by studing the Oxisol samples as well aged synthesised As-Al-Fe co-precipitates and As-adsorbed Al-Fe co-precipitates.

It is known that nanostructured Al- and/or Fe- (hydr)oxides have high arsenic adsorption capacity (Smith et al. 1998; Smedley and Kinniburgh 2002; Adeleye et al. 2016), and that co-precipitation of As along with Al and/or Fe is efficient for As uptake (Violante et al. 2007, 2009; Pantuzzo et al. 2008; Wang et al. 2015). Arsenic can also be incorporated in the structure of the crystal products upon phase transformation of the As-host phases after adsorption/co-precipitation steps (Violante et al. 2007, 2009;

Bolanz et al. 2013, Das et al. 2014). However, the As partition and its stability during phase transformation of the host-phases is still scarcely studied. The mechanism of As incorporation into (Al-)Fe-(hydr)oxides as well as the actual role of Al in this process are yet to be elucidated.

The main objective in this research is to investigate the mechanism for As incorporation into nanocrystalline Al-bearing Fe-(hydr)oxides, and to study the role of Al in this process. This mechanism accounts for the long-term immobilizaiton of As in the environment. The research questions are listed as follows:

i) What As-bearing crystalline Al- and Fe- (hydr)oxide phases are present in the Oxisol liners exposed to the As-rich sulphide tailings?
ii) What eventual phase transformations occur in this process of As incorporation following adsorption/co-precipitation steps?
iii) What are the effects of Al in process?

To accomplish this purpose, both natural and synthetic samples of Al-free and Al-containing Fe-(hydr)oxides were investigated by combining XRD, Raman spectroscopy and inductively coupled plasma with optical emission spectrometry (ICP-OES), with high spatial resolution (S)TEM, EDX and EEL spectroscopies.

1.5. Thesis structure and organization

The present thesis is organized in six chapters. In Chapter 1, the work is contextualized by means of critical review of the up-to-date literature on the mechanisms of arsenic uptake by Al-free and Al-containing Fe-(hydr)oxides. The major lacks regarding (i) the incorporation of either adsorbed or co-precipitated arsenic in (Al-)Fe-(hydr)oxides, (ii) the role of Al in As uptake by the bi-metal (hydr)oxides, and (iii) the As partitioning during phase transformation are highlighted. The relevance and objectives, as well as the main contributions of this Thesis are presented.

Chapter 2 presents a brief description of some (S)TEM techniques used in this research to investigate As-bearing Al-Fe-(hydr)oxides in both environmental and synthetic samples. The aim of this chapter is to highlight main features that make (S)TEM a relatively less explored, but very powerful and unique technique to investigate arsenic in environmental samples. The advantages and drawbacks of the techniques applied are also discussed.

Chapter 3 presents the results and discussion from the analysis of Oxisol samples of environmental concern. The Oxisol samples, collected in a gold mine plant in state of Minas Gerais, Brazil, were used as chemical barrier in facilities for the disposal of As-sulfide concentrates for over a decade. This chapter originated the publication “Natural attenuation of arsenic in the environment by immobilization in nanostructured hematite”, published in 2015 in the journal Chemosphere, volume 138, pages 340-347 (DOI: 10.1016/j.chemosphere.2015.05.101). This article reports for the first time evidences of arsenic incorporation in the crystal structure of natural Al-containing nanostructured hematite in environmental samples. The findings reported in Chapter 3 indicate that natural nanostructured Al-hematite is a secondary phase likely formed from As-bearing natural ferrihydrite that may have undergone an aggregation-based crystal growth.

Chapter 4 is dedicated to the investigation of As-Al-Fe co-precipitates aged for 120 days at pH ~ 11 and ambient temperature. These co-precipitates are As-bearing Al-free and Al-containing goethite (α-FeOOH) and magnetite (Fe_3O_4). This chapter originated the paper “Arsenic entrapment by nanocrystals of Al-magnetite: the role of Al in crystal growth and As retention”, published in 2016 in the journal Chemosphere, volume 158, pages 91-99 (DOI: 10.1016/j.chemosphere.2016.05.044). In this article, evidence for the As incorporation in nanostructured Al-containing magnetite is reported for the first time. The results show that larger amounts of As is uptaken by Al-magnetite relatively to pure magnetite. Nevertheless, a negative correlation between As and Al is reported, and explanations provided.

Chapter 5, entitled “The fate of adsorbed arsenic onto pure and aluminous ferrihydrite upon ageing” presents the investigation of arsenic immobilization in Al-free and Al-containing nanocrystalline ferrihydrite ($Fe_2O_30.5H_2O$). The hypothesis of As entrapment during attachment events to form self-assembly aggregates of ferrihydrite nanoparticles is tested. The results reported in chapters 3 and 4 are highlighted. A mechanism of As incorporation into the net-structure of the crystalline oriented aggregates of Al-Fe-(hydr)oxides is proposed. New evidences on the effects of Al in the improvement of As uptake is shown. Finally, in Chapter 6 the final considerations on the research project are presented. It includes original contributions and main conclusions, as well as suggestions for further investigations.

1.6. References

Adeleye, A. S., Conway, J. R., Garner, K., Huang, Y., Su, Y., Keller, A. A. (2016). Engineered nanomaterials for water treatment and remediation: Costs, benefits, and applicability. *Chem. Eng. J.* vol. 286, 640–662. DOI: 10.1016/j.cej.2015.10.105.

Adra, A., Morin, G., Ona-Nguema, G., Brest, J. (2016). Arsenate and arsenite adsorption onto Al-containing ferrihydrites. Implications for arsenic immobilization after neutralization of acid mine drainage. *Appl. Geochem*. vol. 64, 2-9. DOI: 10.1016/j.apgeochem.2015.09.015.

Adra, A., Morin, G., Ona-Nguema, G., Menguy, N. Maillot, F. Casiot, C. Bruneel, O., Lebrun, S., Juillot, F., Brest, J. (2013). Arsenic scavenging by aluminum-substituted ferrihydrites in a circumneutral pH river impacted by acid mine drainage. *Environ. Sci. Technol*. vol. 47 (22), 12784–12792. DOI: 10.1021/es4020234.

Akin, I., Arslan, G., Tor, A., Ersoz, M., Cengeloglu, Y. (2012). Arsenic(V) removal from groundwater water by magnetic nanoparticles synthesized from waste red mud. *J. Harzard. Mater*. vol. 235-236, 62-68. DOI: 10.1016/j.hazmat.2012.06.024.

Berar, J. -F., Lelann, P. (1991). E.S.D.’s and estimated probable error obtained in Rietveld refinements with local correlations. *J. Appl. Cryst.* vol. 24: 1-5. DOI: 10.1107/S0021889890008391.

Bolanz, R. M., Wierzbicka-Wieczorek, M., Čaplovičová, M., Uhlík, P., Göttlicher, J., Steininger, R., Majzlan, J. (2013). Structural incorporation of As^{5+} into hematite. *Environ. Sci. Technol.* vol. 47 (16): 9140–47. DOI: 10.1021/es305182c.

Cao, C. Y., Qu, J., Yan, W. S., Zhu, J. F., Wu, Z. Y., Song, W. G. (2012). Low-cost synthesis of flowerlike α-Fe_2O_3 nanostructures for heavy metal ion removal: Adsorption property and mechanism. *Langmuir* vol. 28 (9), 4573–4579. DOI: 10.1021/la300097y.

Carabante, I., Mouzon, J., Kumpiene, J., Gran, M., Fredriksson, A., Hedlund, J. (2014). Reutilization of porous sintered hematite bodies as effective adsorbents for arsenic (V) removal from water. *Ind. Eng. Chem. Res.*, vol. 53, 12689–12696.

Ciminelli, V. S. T., Antônio, D. C., Caldeira, C. L., Gasparon, M., Ng, J., Freitas, E. T. F., Delbem, I. D., Fernandes, M. M. (2017). Low arsenic bioaccessibility by fixation in nanostructured iron (hydr)-oxides: a quantitative identification of As-bearing phases. Manuscript in preparation.

Cölfen, H., Antonietti, M. (2008). *Mesocrystals and nonclassical crystallization*. Chichester: England. John Wiley & Sons, Ltd.

Dale, J. G., Stegemeier, J. P., Kim, C. S. (2015). Aggregation of nanoscale iron oxyhydroxides and corresponding effects on metal uptake, retention, and speciation: I. Ionic-strength and pH. *Geochim. Cosmochim. Acta*. vol. 148: 100-112. DOI: 10.1016/j.gca.2014.08.029.

Das, S., Hendry, M. J., Essilfie-Dughan, J. (2011). Effects of adsorbed arsenate on the rate of transformation of 2-line ferrihydrite at pH 10. *Environ. Sci. Technol.* vol. 45: 5557–5563.

Das, S., Essilfie-Dughan, J., Hendry, M. J. (2014a). Arsenate adsorption onto hematite nanoparticles under alkaline conditions: effects of aging. *J. Nanoparticle Res.* vol. 16 (7): 2490. DOI: 10.1007/s11051-014-2490-3.

Das, S., Essilfie-Dughan, J., Hendry, M. J. (2014b). Arsenate partitioning from ferrihydrite to hematite: Spectroscopic evidence. *Am. Mineral.* vol. 99, 749–754. DOI: 10.2138/am.2014.4657.

De Yoreo, J., Gilbert, P. U. P. A., Sommerdijk, N. A. J. M., Penn, R. L.,Whiteam, S., Joester, D., Zhang, H., Rimer, J. D., Navrotsky, A.,Banfield, J. F., Wallace, A. F., Michel, F. M., Meldrum, F. C., Cölfen, H., Dove, P. M. (2015). Crystallization by particle attachment in synthetic, biogenic, and geologic environments. *Science*. vol 349 (6247): aaaa6760.

Ding, Z., Fu, F., Cheng, Z. Lu, J., Tang, B. (2017). Novel mesoporous Fe-Al bimetal oxides for As(III) removal: performance and mechanism. *Chemosphere* vol. 169: 297-307. DOI: 10.1016/j.chemosphere.2016.11.057.

Duarte, G., Ciminelli, V. S. T., Gasparon, M., Mello, J. W. V. (2012). Evaluation of 10 years stability of concentrated As-sulfide tailings. In: Jack, C. N., Noller, B N., Naidu, R., Bundschuh, J., Bhattacharya, P. *Proceedings of the 4th International Congress on Arsenic in the Environment* - Understanding the Geological and Medical Interface of Arsenic – As 2012. Cairns, Australia. 423–425.

Feng, L., Cao, M., Ma, X., Zhu, Y., Hu, C. (2012). Superparamagnetic high-surface-area Fe 3O 4 nanoparticles as adsorbents for arsenic removal. *J. Hazard. Mater*. vol. 217–218, 439–446. DOI: 10.1016/j.jhazmat.2012.03.073.

Freitas, E. T. F., Montoro, L. A., Gasparon, M., Ciminelli, V. S. T. (2015). Natural attenuation of arsenic in the environment by immobilization in nanostructured hematite. *Chemosphere* vol. 138: 340–47. DOI: 10.1016/j.chemosphere.2015.05.101.

Freitas, E. T. F., Stroppa, D. G., Montoro, L. A., Mello, J. W. V., Gasparon, M., Ciminelli, V. S. T. (2016). Arsenic entrapment by nanocrystals of Al-magnetite: The role of al in crystal growth and As retention. *Chemosphere* vol. 158: 91–99. DOI: 10.1016/j.chemosphere.2016.05.044.

Guo, H., Ren, Y., Liu, Q., Zhao, K., Li, Y. (2013). Enhancement of arsenic adsorption during mineral transformation from siderite to goethite: mechanism and application. *Envi. Sci. Technol*. vol. 47 (2): 1009-1016. DOI: 10.1021/es303503m

Guo, X., Yang, Z., Dong, H., Guan, X., Ren, Q., LV, X., JIN, X. (2016). Simple combination of oxidants with zero-valent-iron (ZVI) achieved very rapid and highly efficient removal of heavy metals from water. *Water Res.*, vol. 88, 671–680. DOI: 10.1016/j.watres.2015.10.045.

Hua, M., Zhang, S., Pan, B., Zhang, W., LV, L., Zhang, Q. (2012). Heavy metal removal from water/wastewater by nanosized metal oxides: A review. *J. Hazard. Mater*, vol. 211–212, 317–331. DOI: 10.1016/j.jhazmat.2011.10.016.

Huang, Y. W., Wu, C. H., Aronstam, R. S. (2010). Toxicity of transition metal oxide nanoparticles: Recent insights from in vitro studies. *Materials*, vol. 3 (10): 4842–4859. DOI: 10.3390/ma3104842.

Ladeira, A. C. Q., Ciminelli, V. S. T., Duarte, H. A., Alves, M. C. M., Ramos, A. Y. (2001). Mechanism of anion retention from EXAFS and density functiona calculations: arsenic (V) adsorbed on gibbsite. *Geochim. Cosmochim. Acta*. vol. 65 (8): 1211-1217. DOI: 10.1016/S0016-7037(00)00581-0.

Ladeira, A. C. Q., Ciminelli, V. S. T., Nepomuceno, A. L. (2002). Seleção de solos para a imobilização de arsênio. *Rem: R. Esc. Minas* vol. 55 (3): 215-221. DOI: 10.1590/S0370-44672002000300009.

Ladeira, A. C. Q., Ciminelli, V. S. T. (2004). Adsorption and desorption of arsenic on na Oxisol and its constituents. *Water Res*. vol. 38 (8):; 2087-2094. DOI: 10.1016/j.watres.2004.02.002.

Masue, Y., Loeppert, R.H., Kramer, T.A. (2007). Arsenate and arsenite adsorption and desorption behavior on coprecipitated aluminum iron hydroxides. *Environ. Sci. Technol.* vol. 41 (3): 837–842. DOI: 10.1021/es061160z.

Mehta, D., Mazumdar, S., Singh, S. K. (2015). Magnetic adsorbents for the treatment of water/wastewater - A review. *J. Water Process Eng.* vol. 7: 244–265. DOI: 10.1016/j.jwpe.2015.07.001.

Mohan, D., Pittman Jr., C. U. (2007). Arsenic removal from water/wastewater using adsorbents-A critical review. *J. Hazard. Mater.* vol. 142 (1–2), 1–53. DOI: 10.1016/j.jhazmat.2007.01.006.

Morin, G., Wang. Y., Ona-Nguema, G., Julliot, F., Calas, G., Menuy, N., Aubry, E., Bargar, J. R., Brown Jr., G. E. (2009). EXAFS and HRTEM evidence for As(III)-containing surface precipitates on nanocrystalline magnetite: impications for As sequestration. *Langmuir* vol. 25 (16): 9119-9128. DOI: 10.1021/la900655v.

Niederberger, M., Cölfen, H. (2006). Oriented attachment and mesocrystals: non-classical crystallization mechanisms based on nanoparticles assembly. *Phys. Chem. Chem. Phys*. vol. 8: 3271-3287. DOI: 10.1039/b604589h.

Novoselova, L. Y. (2016). Hematite nanopowder obtained from waste: Iron-removal sludge. *Powder Technol.*, vol. 287: 364–372. DOI: 10.1016/j.powtec.2015.10.020

Ona-Nguema, G., Morin, G., Julliot, F., Calas, G., Brown Jr., G. E. (2005). EXAFS analysis of arsenite adsorption onto two-line ferrihydrite, hematite, goethite, and lepidocrocite. *Environ. Sci. Techno*. vol. 39: 9147-9155. DOI: 10.1021/es050889p.

Ona-Nguema, G., Morin, G., Wang, Y., Foster, A. L., Juillot, F., Calas, G., Brown, G. E. (2010). XANES evidence for rapid arsenic(III) oxidation at magnetite and ferrihydrite surfaces by dissolved O(2) via Fe(2+)-mediated reactions. *Environ. Sci. Technol*. vol. 44 (14): 5416–5422. DOI: 10.1021/es1000616.

Pantuzzo, F. L., Ciminelli, V. S. T., Brito, W. (2008). New Evidences for the Role of Precipitation and Adsorption during Fe(III)-As(V) Coprecipitation. In: Young, C.A., Taylor, P. R., Anderson, C. G. *Hydrometallurgy: Proceedings of the Sixth International Symposium*. Society for Mining, Metallurgy, and Exploration, Inc. Littleton, Colorado, USA. 130–139.

Pizarro, C., Rubio, M. A., Escudey, M., Albornoz, M. F., Muñoz, D., Denardin, J., Fabris, J. D. (2015). Nanomagnetite-zeolite composites in the removal of arsenate from aqueous system. *J. Braz. Chem. Soc.* vol. 26(9): 1887-1896. DOI: 10.5935/0103-5053.20150166.

Scott, H. G. (1983). The estimation of standard deviations in powder diffraction Rietveld refinements. *J. Appl. Cryst.* vol. 16: 159-163. DOI: 10.1107/S0021889883010195.

Silva, G. C., Almeida, F. S., Ferreira, A. M., Ciminelli, V. S. T. (2012). Preparation and application of a magnetic composite (Mn_3O_4/Fe_3O_4) for removal of As(III) fro aqueous solutions. *Mat. Res.* vol. 15 (3): 403-408. DOI: 10.1590/S1516-14392012005000041.

Silva, G. C., Paula, J. A., Duarte, G., Ciminelli, V. S. T. (2013). Avaliação da estabilidade de rejeitos concentrados em sulfeto após 10 anos de disposição. In: XXV Encontro Nacional de Tratamento de Minérios e Metalurgia Extrativa & VIII

Meeting of the Southern Hemisphere on Mineral Technology, Goiânia. Anais do XXV Encontro Nacional de Tratamento de Minérios e Metalurgia Extrativa. vol.3: 259-266.

Silva, J., Mello, J. W. V., Gasparon, M., Abrahão, W. A. P., Ciminelli, V. S. T., Jong, T. (2010). The Role of Al-Goethites on Arsenate Mobility. *Water Res.* vol. 44 (19): 5684–5692. DOI: 10.1016/j.watres.2010.06.056.

Smedley, P. L., Kinniburgh, D. G. (2002). A Review of the Source, Behaviour and Distribution of Arsenic in Natural Waters. *Appl. Geochemistry* vol. 17 (5): 517–568. DOI: 10.1016/S0883-2927(02)00018-5.

Smith, E., Naidu, R., Alston, M. (1998). Arsenic in the Soil Environment: A Review. *Adv. Agron.* vol. 64: 149–195. DOI: http://dx.doi.org/10.1016/S0065-2113(08)60504-0.

Stegemeier, J. P., Reinsch, B. C., Lentini, C. J., Dale, J. G., Kim, C. S. (2015). Aggregation of nanoscae iron oxyhydroxides and corresponding effects on metal uptake, retention, and speciation: II. Temperature and time. *Geochim. Cosmochim. Acta*. vol. 148: 113-129. DOI: 10.1016/j.gca.2014.08.031.

Tang, W., Li, Q., Gao, S., Shang, J. K. (2011). Arsenic (III,V) removal from aqueous solution by ultrafine α-Fe2O3 nanoparticles synthesized from solvent thermal method. *J. Hazard. Mater.* vol. 192 (1): 131–138. DOI: 10.1016/j.jhazmat.2011.04.111.

Violante, A., Ricciardella, M., Del Gaudio, S., Pigna, M. (2006). Coprecipitation of arsenate with metal oxides: nature, mineralogy, and reactivity of aluminum precipitates. *Environ. Sci. Technol.* vol. 40: 4961-4967. DOI: 10.1021/es052321m.

CHAPTER 2. Transmission electron microscopy techniques applied to the characterization of environmental and synthetic samples

2.1. Introduction

Amongst the available techniques for solid phase analyses and characterization, transmission electron microscopy (TEM) is unique in allowing the investigation of both elemental and (crystalline or amorphous) phase composition of samples down to nanometre or even atomic scale. The TEM techniques are not to be used in exploratory studies of solid phases as a very minor part of a given sample is investigated, unless the nature of the sample being studied requires so. It would rather be necessary previous bulk analyses of the sample, such as chemical characterization, X-ray fluerescense and diffraction analyses to assess its main composition. On the other hand, there is no better technique to completely characterize solid phases down to nanometre scale than TEM with high spatial and analytical resolution. Of course, one must be aware of the drawbacks and the instrument limitations. In this chapter, some TEM thechniques (high-resolution TEM, electron diffraction, energy dispersive X-ray and electron energy-loss spectroscopies) used to characterize both environmental and synthetic samples in this research are briefly described to give a clearer idea about TEM for readers not familiar with these techniques.

The very nature of the environmental samples imposes drawbacks to the accurate identification of the trace-contaminated host phases. These samples are consisted of several phases (e.g. phyllosilicates, sulfides, aluminium and iron (hydr)oxides, and carbonates and not rarely organic matter), and particle sizes from few nanometres to several micrometres. The smaller particles are very often tangled with each other or with larger particles such as phyllosillicates (see Figures 2.1), and their complete separation are difficult and often unfeasible by physical or chemical methods (Elsass et al. 2008). Therefore, the structural characterization of phases with trace metals contaminants, such as arsenic and antimony, in environmental samples is not trivial due to particles’ heterogeneity, small grain size and low concentrations. Synchroton-based analytical techniques such as X-ray absorption spectroscopy (XAS), which has lateral resolution of about 30 nm (Egerton 2008), is often combined with theoretical molecular modelling or with other spectroscopic techniques to investigate As distribution, speciation, and bonding characteristics. However, the needed spatial resolution down to tenths of nanometre can be achieved by TEM. Indeed, one can perfom electron energy-loss spectroscopy (EELS) analysis in a transmission electron microscope, and much of the information obtained in EEL spectra is similar to that given by XAS. The use of TEM techniques is very powerfull to fully characterize a given sample, because it allows the combination of image analysis, electron diffraction, energy dispersive X-ray spectroscopy (EDS), and EELS, for example, all in one machine and with better spatial resolution, even down to atomic scale in modern TEMs, than any other scattering technique. The aim of this chapter is to introduce some TEM techniques used in samples' characterization in this present Thesis. Few exemples of the analysis of environmental samples collected in different gold mine plants are given.

2.2. TEM techniques

2.2.1. High resolution transmission imaging

The images of a given sample observed at the transmission electron microscope screen are made from electrons transmitted through the sample. These electrons are then scattered by the atoms and molecules as they travel through the specimen. The first aspect to be mentioned here is the suitable thickness of samples to allow electrons travelling through their structure. It does depend on the electron's mean free path in each material, but generaly speaking the sample thickness should be <100 nm for TEM. For high resolution TEM the specimen should be as thinner as possible (<50 nm). One might also be aware of the electron dose because a high energetic electron beam (200 – 300 keV) may demage the sample. If this is the case, low electron dose or even cryo-TEM is advisable to avoid beam-damage. In a TEM, the primary electrons are scattered: (i) elastically, by the nuclei of atoms in the sample – Rutherford scattering; (ii) inelastically, by the electrons bond to atoms of the sample; and (iii) diffracted by the lattice, no matter the sample is crystalline or not. The transmitted electrons and other signals generated in the sample-beam interaction, carry various types of information that can be assessed if the microscope is coupled with the proper detectors.

As for transmitted electron imaging, three mechanisms of contrast in the process of image formation will affect it – thickness, mass and diffraction contrast. In TEM, electrons travelling through thicker regions of the specimen will be less transmitted and that area will appear darker in the formed image at the screen. Figure 2.1 shows particles of several phases of an Oxisol liner sample dispersed on a thin holey carbon-coated TEM Cu-support grid.

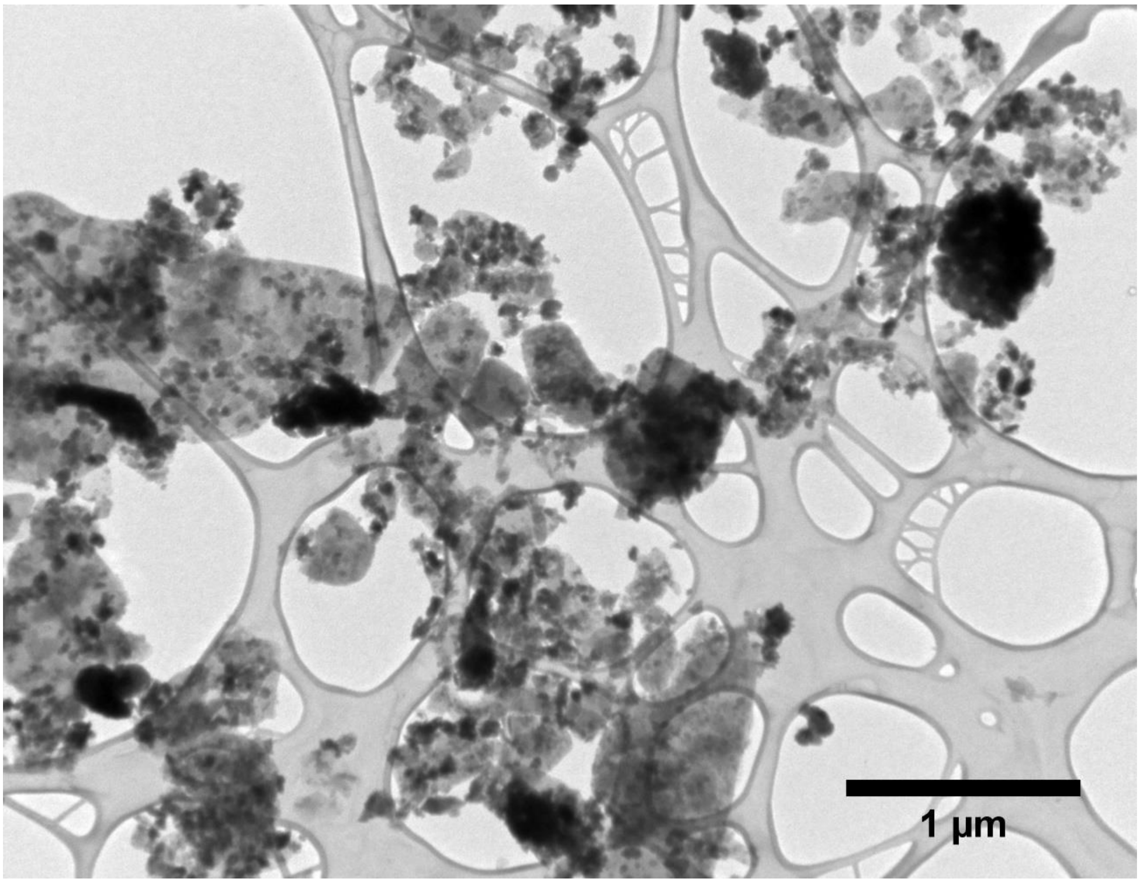

Figure 2.1. TEM image of an Oxisol liner sample that was exposed to As-sulfide concentrate for over a decade.

As the sample is heterogeneous, several particles are seen superimposed and appear darker in the image shown in Figure 2.1. Thickness contrast is dominant for larger particles. Mass contrast is also clearly seen in bright field (BF) TEM images when electrons travel through an area in the sample with different chemical composition and no considerable thickness variation. The interaction of the primary electron beam with the heavier atomic nuclei will generate darker areas in the image as the transmitted electrons will be scattered at higher angles.

As for diffraction contrast, the transmitted electrons coming out from the sample interfere constructively and destructively thus having a periodic maximum and minimum intensities distribution, respectively, at a certain plane (called back focal plane) where the diffraction pattern is formed (Figure 2.2).

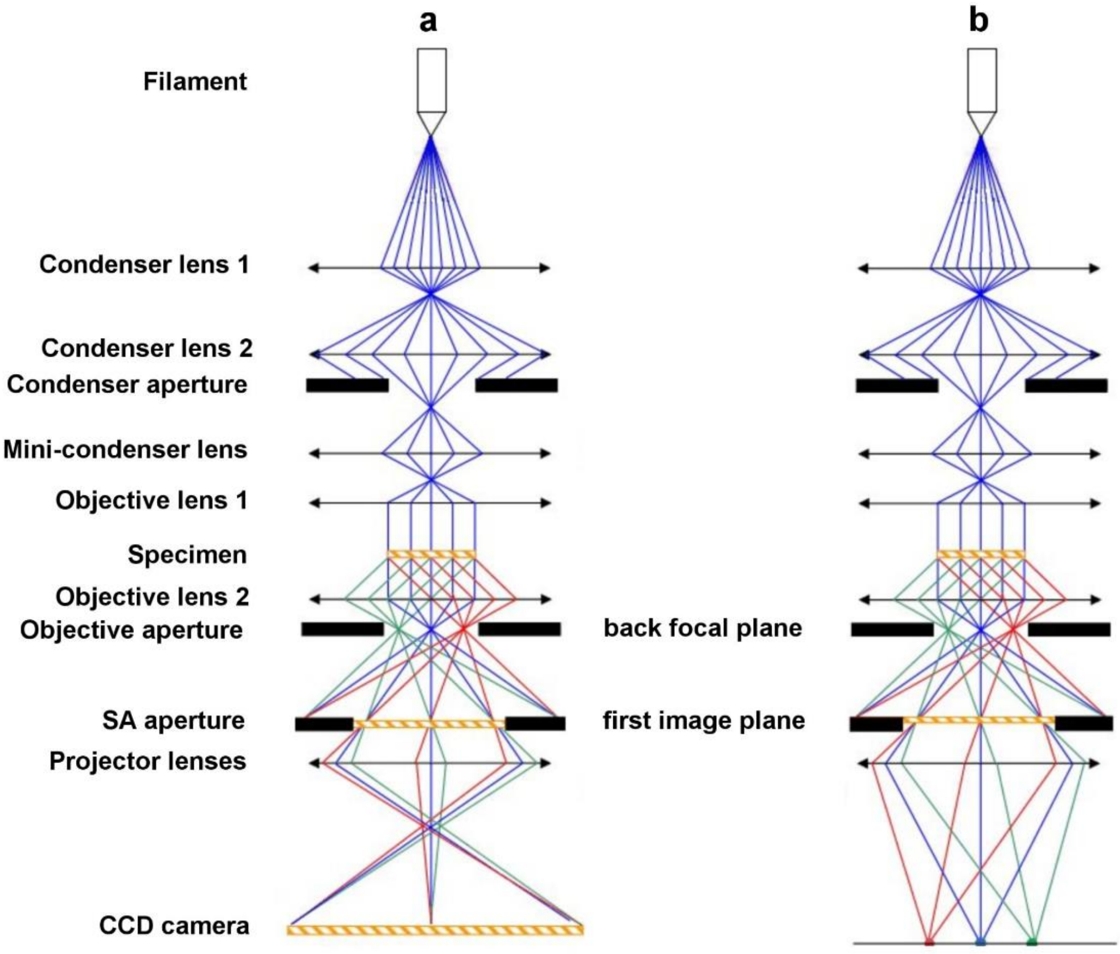

Figure 2.2. Schematics of lenses (double-head arrows) and apertures (black filled rectangles) in a conventional TEM showing beam path (blue lines) from the filament tip all the way down to the TEM (CCD camera) screen in bright field image mode (a) and diffraction mode (b). The red and green segment of lines represent the diffracted beam by the specimen. The diffracted beam scattered at the same Bragg angle interfere at the back focal plane to form the diffraction pattern. In image mode, the projector lenses are set up to project the first image plane to the TEM screen. In diffraction mode, the diffraction pattern formed at the back focal plane is projected to the screen when the projector lenses' currents are changed.

The diffracted electrons also form images of periodic dark and bright fringes clearly seen at high magnifications. If the sample is well oriented along a certain crystallographic direction, the lattice atomic planes parallel to the electron beam can be imaged and the periodic fringes observed in the high resolution TEM (HRTEM) image will correspond to the lattice planes of the sample, as seen in Figure 2.3. Brighter or darker points seen in a HRTEM image does not show the actual atomic position, but the crystalline sctructure and lattice defects or dislocations can be assessed.

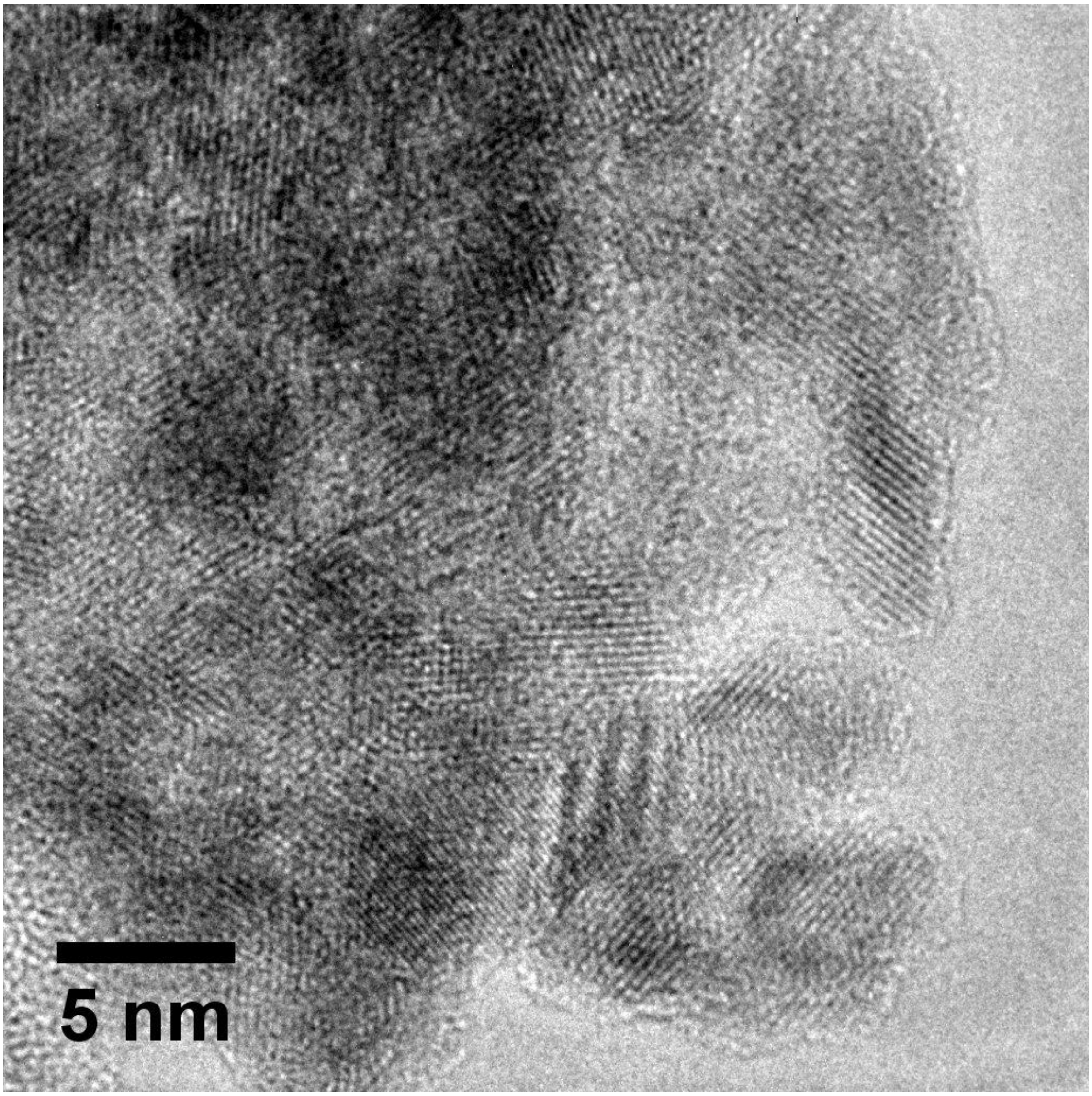

Figure 2.3. HRTEM image showing an aggregate of As-bearing Al-hematite nanopartices found in Oxisol sample.

In scanning TEM (STEM), the contribution of diffraction contrast is reduced, so the most predominant contrast mechanism depends on mass and thickness. In STEM mode, a focused beam rasters the sample sitting at each point for few microseconds per frame. The images performed by using the annular dark field (ADF) STEM detector have an opposite contrast to that of BF-TEM image, and heavier regions of the sample will appear brighter in the image (Figure 2.4.a). The diffraction contrast can be negligible in STEM by using a high-angle annular dark field (HAADF) detector, because the angle range of the scattered electrons by the atom nuclei are larger than the Bragg angles. Figure 2.4.b shows a HAADF-STEM image where mass contrast is predominant.

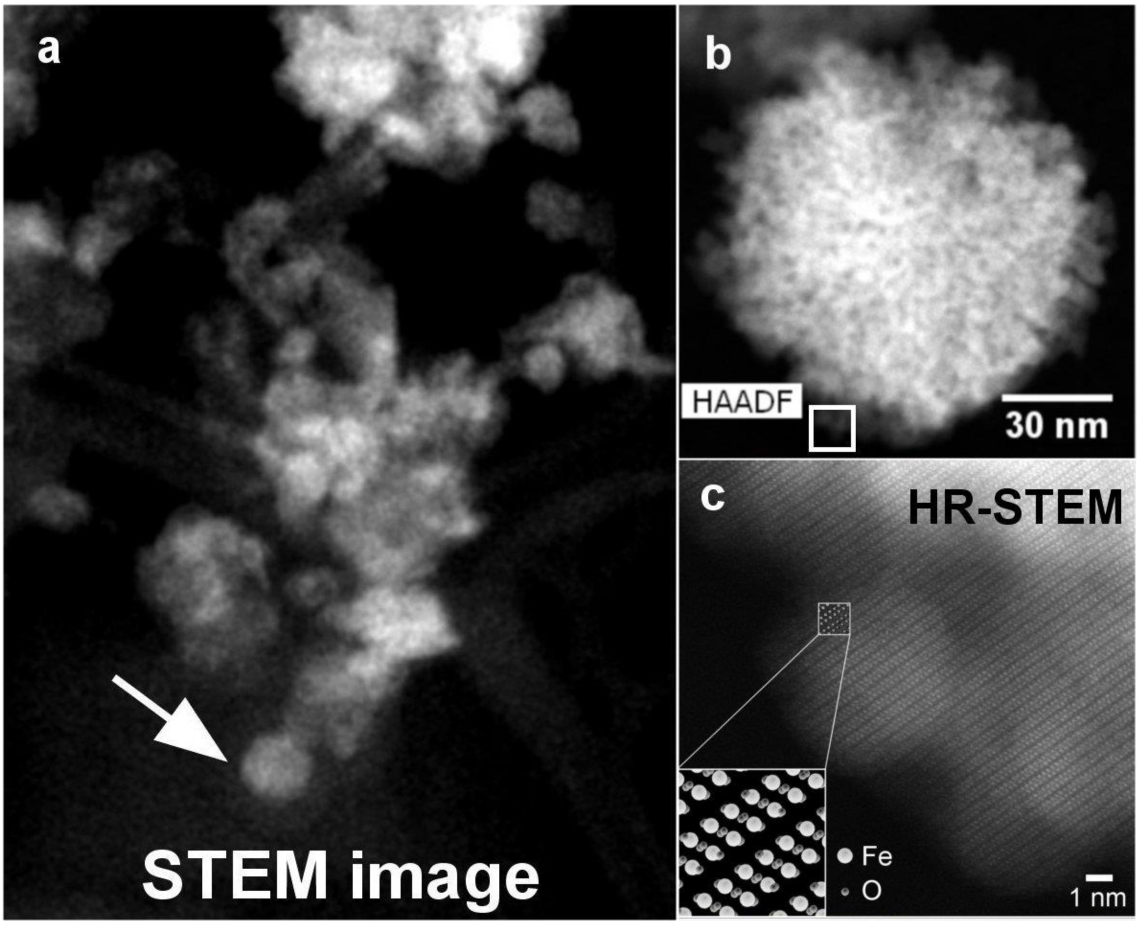

Figure 2.4. (a) Annular dark field STEM image of an Oxisol sample. (b) High-angle annular dark field (HAADF) STEM image of the particle pointed by the arrow in (a). (c) High resolution STEM image taken in the area inside the white square indicated in (b). The oriented nanoparticles' aggregate is shown in detail. The white spots in the image correspond to the Fe atom columns along [221]. The simulated Fe and O atomic positions for hematite along this crystallographic direction is shown in the inset.

The features observed in HAADF-HR-STEM images performed in aberration corrected microscopes can be directly related to the atomic structure, because the electron probe scanning the sample can be smaller than an atom size. In this case, brighter spots in images will correspond to the exact positon of an atom column of the specimen as shown in Figure 2.4.c.

2.2.2. Electron diffraction

Diffraction analysis at the TEM can be performed in different ways as illustrated in Figure 2.5, which depend on the beam illumination system. The conventional selected area electron diffraction (SAD), convergent-beam electron diffraction (CBED), and nano-beam electron diffraction (NBD) are briefly described as follows.

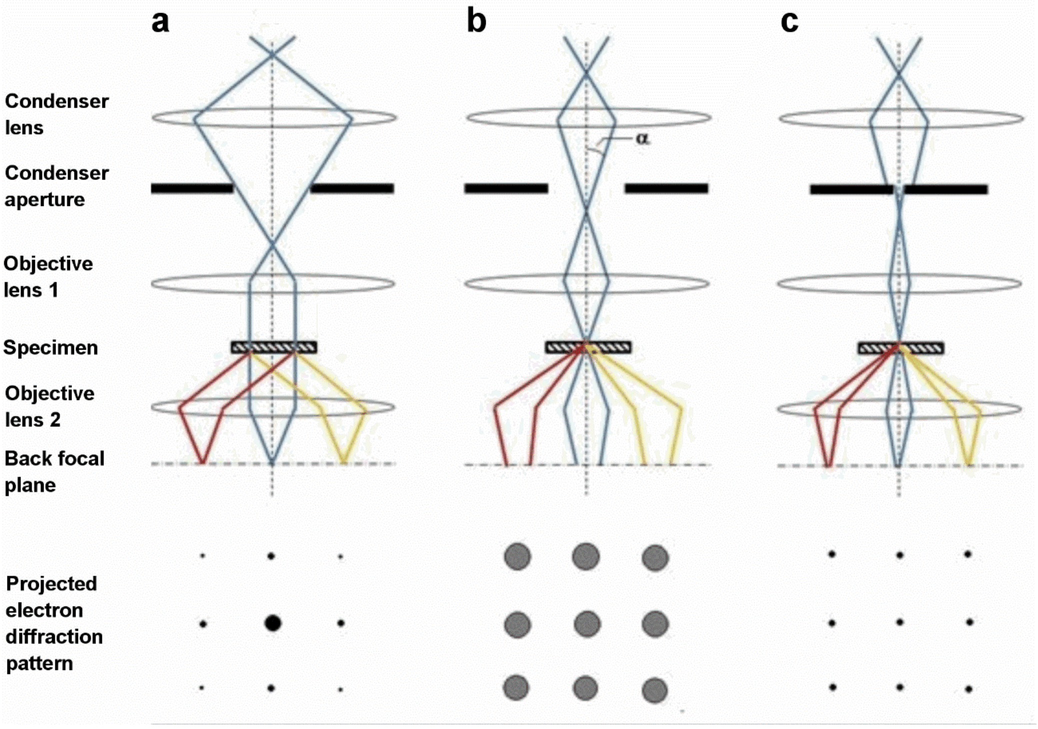

Figure 2.5. Schematics showing the illumination system for (a) selected area electron diffraction (SAD), (b) convergent-beam electron diffraction (CBED), and (c) nano-beam electron diffraction (NBD). Some diffracted beams are depicted in red, blue and green below the specimen. The diffraction pattern is formed at the back focal plane. In SAD mode, the lenses are set up to that a parallel beam illuminates the specimen. In CBED mode, the convergence semi-angle (α) is changed so that a narrower focused beam illuminates a very minor area in the sample. In NBD, a smaller condenser aperture size (10 μm) is placed to decrease the semi-angle α down to 1 mrad or smaller, to have a narrower nearly parallel beam.

The SAD measuremets are done by illuminating the sample with parallel beam (Figure 2.5.a). A selected area (SA) of the sample is chosen by placing an SA aperture that is located at the first image plane formed in the microscope (see Figure 2.2). In practice, due to imperfections in the objective lens, the minimum suitable area that can be selected is about 400 nm (Williams and Carter 2009). This selected area can be smaller for spherical aberration corrected TEMs, but still limited by the SA aperture size. To assess structural information of a smaller area of the sample (tens of nanometers), one needs to perform CBED or NBD. The basic difference from SAD is that a narrow-focused beam is used to illuminate the desirable area of the sample (Figure 2.5.b). Visually, the SADP consist of small spots while in the CBEDP the diffracted disks are seen at the screen. The centre of the disks corresponds to the exact *hkl* Bragg reflection position. The diameter of the *hkl* disks depends on the convergence semi-angle (α). When selecting a smaller condenser apearture size (10 μm), the semi-angle is significanty reduced (<1 mrad) so that the narrower beam becomes nearly parallel. This condition is used to perform NBD to access crystallographic information of an area of few nanometres depending on the beam probe size (<50 nm). These diffraction techniques can be applied to assess fundamental crystallographic information such as crystal system, Bravais lattice, point and space groups, to study dislocations and defects, to do thickness measurement, and lattice parameters refinement (Morniroli and Steeds 1992; Morniroli and Jacob 2012; Saitoh et al. 2013).

2.2.3. Spectroscopy

The beam-sample interaction in an electron microscope generates several signals such as Auger electrons, secondary and backscattered electrons, X-ray, and cathodoluminescence. However, most commercially available TEMs are not coupled with detectors to collect all these signals, but energy dispersive X-ray (EDX) detectors are very common in TEM, used for chemical analysis. The elemental identification is possible by collecting the X-ray with specific energies. When the electron beam hits the sample, an inner-shell electron of an atom can be knocked out, and an outher-shell electron will fill the vacancy in the inner-shell. In this process, X-ray with characteristic energies are emitted. In practice, almost all elements above about C (Z = 6) can be detected by EDX spectroscopy (or simply EDS) in a TEM, but light elements are difficult to measure as valence electrons are involved in characteristics X-ray emission. In addition, semi-quantification analysis should not be done for light elements (Z < 11), as low fluorescence produce absorption within the sample (Williams and Carter 2009).

For light elements, it is better to perform EELS analysis as further discussed. Chemical information and elemental distribution across the sample can be obtained by both EDS and EELS analyses as they are complementary techniques. Elemental maps can be performed through STEM-EDS, TEM-EELS or STEM-EELS. The advantages, drawbacks and differencces between these techniquies are discussed in the following paragraphs.

The EDS mapping is performed having the microscope in STEM mode. While the focused beam rasters an area of the sample, EDX spectra of each point of the scanned area are collected and summed up. The elemental map is then performed via software by forming red-green-blue (RGB) images which show the signal intensity distribution of a given energy.

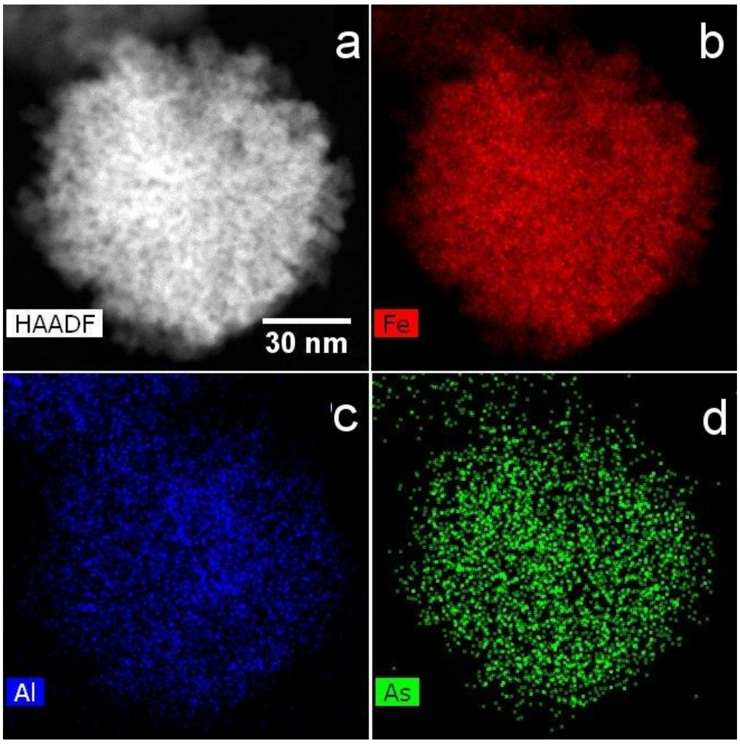

Figure 2.6. (a) High-angle annular dafk field (HAADF) STEM image of an oriented aggregate of Al-hematite nanoparticles. (b-d) EDS maps showing the distribution of Fe, Al and As in the Al-hematite.

Figures 2.6 shows the STEM-EDS maps for Fe, Al and As performed in the hematite nanoparticles' aggregate. There is no segregation of either Al or As. In this case, the homogenous distribution of As and Al along with Fe suggests they may be incorporated in the hematite structure. It is unlike that Al or As is present as impurities or forming clusters. Indeed, the HR-STEM image of the hematite nanoparticles' aggregate (see Figure 2.4.c) shows the well aligned columns of atoms and no defect in the lattice.

The advantages of STEM-EDS analysis are the wide range or elements that can be identified, as characteristics X-ray up to 40 keV can be displayed in the EDX spectrum, and the spatial resolution that is nearly the probe size. Once a given element content in the sample is above the EDS detection limit, the suitable X-ray counts will ultimately depend on electron source, the probe current on the specimen, the EDS detector and the X-ray collection angle. There is a compromise between X-ray signals and spatial resolution, which is related to the minimum mass fraction of an element that can be detected (Williams and Carter 2009). In general, the EDS detection limit is around 1 wt% for thermoionic electron sources (W or LaB_6), and about 0.1 wt% for field emission gun (FEG) microscopes. Nonetheless, EDS analysis for light elemments ($Z < 11$) is not reliable for the reasons mentioned earlier, but for EELS analysis. In addition, the EELS sensitivity for light elements can be ten times better compared to EDS, and for heavier elements ($10 < Z < 25$) EELS detection limit is still lower than for EDS if the $L_{2,3}$ edges are analysed (Leapman and Hunt 1991).

The transmitted beam loses energy due to the inelastic scattering by the electrons in the atoms of the specimen. The core energy-loss is due to the interaction of the beam with inner-shell electrons and gives rise to ionization edges. The energy-losses for the ionization edges are characteristics for each element, and can be used for elemental identification, oxidation state measurement, and phase identification by analysing the energy-loss near edge structure (ELNES) approx. 50 eV beyond the edge threshold (Egerton 2008). Figures 2.7.c, 2.7.e, and 2.7.g, show the ionization edges for O, Fe, and Al, respectively, found in the oriented aggregate of Al-hematite nanoparticles. This phase was confirmed by the O K-near edge spectrum and electron diffraction (not shown).

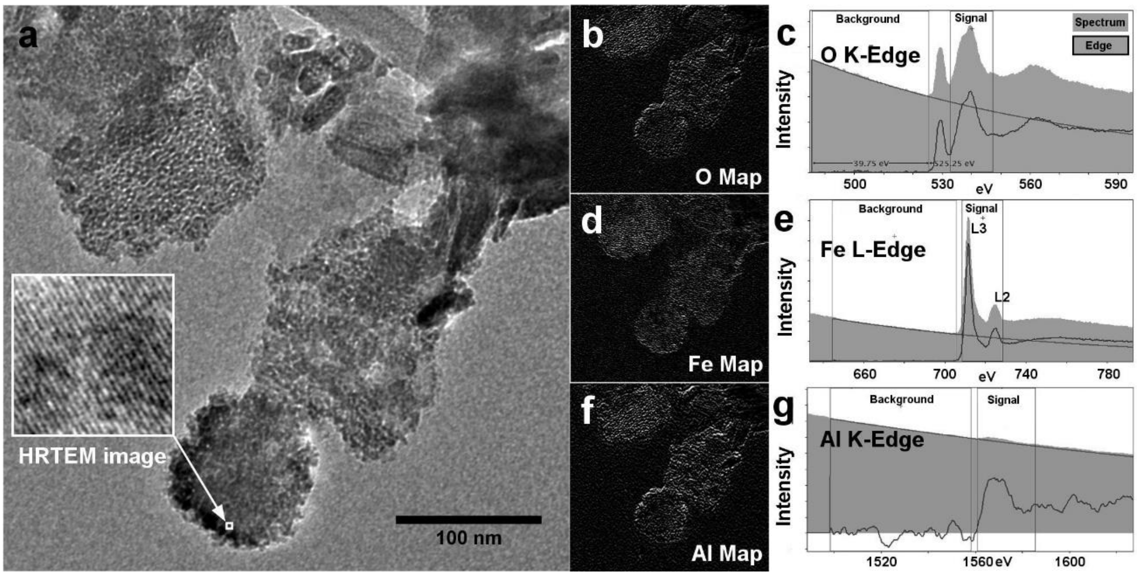

Figure 2.7. (a) Bright field TEM image of some Al-Fe-(hydr)oxide particles found in an Oxisol liner sample. The inset shows the HRTEM image taken at point indicated by the arrow. (b-g) Elemental maps performed by energy-filtered TEM (EFTEM) analysis and the correspondent peak in the EEL spectra for O K-edge (b-c), Fe L-edge (d-e), and for Al K-edge (f-g). The maps show the broadly distribution of Al across the particles. The images (b,d,f) were performed by integrating electrons with energy-losses shown in the signal integration windows (above the background) in each correspondent spectrum.

The advantage of TEM-EELS or STEM-EELS analyses is that not only elemental composition can be assessed, but structure, chemical bonding environment and oxidation state can be measured and mapped. The TEM-EELS mapping is performed by using the transmitted electrons with characteristics energy-losses. It is basically done by placing a narrow slit in the projected spectrum plane to select a small energy window, i.e. a signal window as shown in EELS spectra in Figures 2.7. (c,e,g), for exemple. For more details in EELS instrumentation, see Egerton (2008) and Williams and Carter (2009). The electrons with the characteristic energy-loss selected by the slit are then used to project the energy-filtered TEM (EFTEM) image at the CCD camera. The signal/background ratio can be improved by subtracting the background image from the signal image. The background image is performed by placing the slit to select an energy window right before the ionization egde of the element (see Figure 2.7). All this is automatically done by choosing the called two or three windows methods when performing EFTEM analysis at the microscope.

Elemental mapping can also be carried out by STEM-EELS. An entire EEL spectrum is taken at each point of the area in the sample while it is scanned by the focused electron beam. The spectra correspondent to each (x, y) pixel coordinate form a called spectrum image (SI). This technique has been successfully applied in a wide range of studies both in materials and life sciences (Colliex 2017; Leapman 2017). All the information in the STEM-EELS-SI can be assessed afterward – elemental maps, phase and even oxidation state maps can be generated by post-processing data. Figure 2.8 shows the results of the EELS-SI analysis for a sample from the taillings produced in a gold mine in Minas Gerais state, Brazil. The interest is to investigate the association of antimony (Sb) with Fe. A relatively fast mapping (approx. 3 minutes) was performed to avoid drifting effects. The results show Sb associated with Fe-(hydr)oxides. The EELS mapping for Fe M-, Al L-, and Sb N- edges were performed from the SI data. The Sb M-Edge at 528 eV was not used for mapping because it overlaps with the pre-peak at the O K-edge for Fe-(hydr)oxides, but the presence of Sb was confirmed by the EDS analysis (Figure 2.8.g).

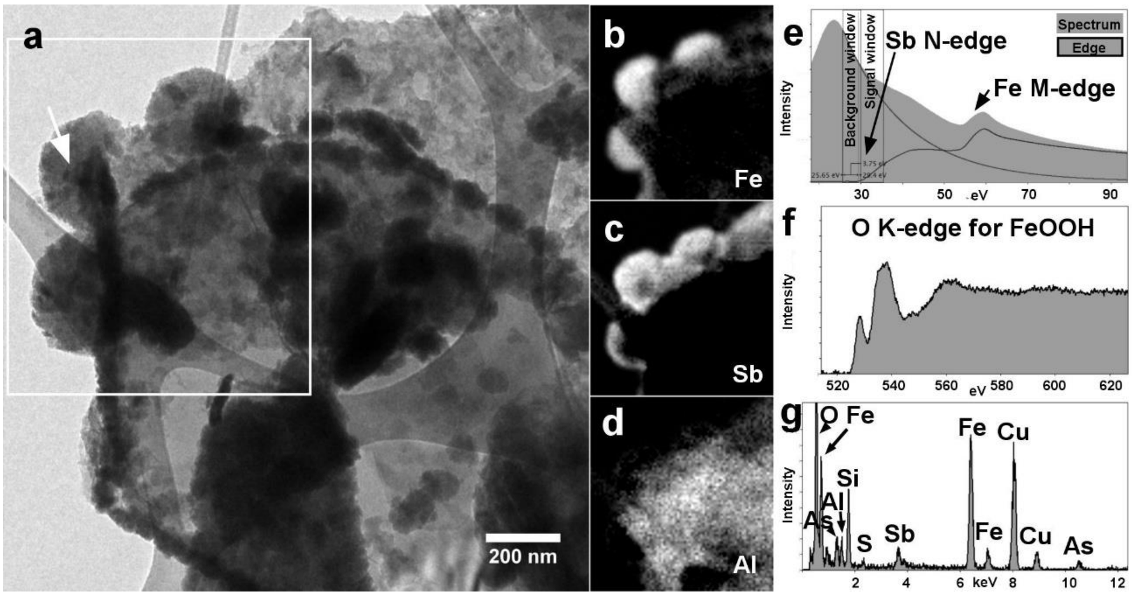

Figure 2.8. (a) Bright field TEM image showing precipitates of Fe-(hydr)oxides (darker particles) among an Al-silicate. (b-d) EELS maps for Fe, Sb and Al taken from STEM-EELS-SI analysis of the area inside the white rectangle in (a). (e, f) EELS spectra taken from the precipitate is indicated by the arrow in (a). The spectrum in (e) shows the Sb N- and Fe M- edges at 31 eV and 54 eV, respectively. The spectrum in (f) shows the O K-edge at 532 eV. (g) EDX spectrum taken from the precipitate pointed in (a). The Cu signal arises from the X-ray generated from the interaction of stray electrons with the support TEM Cu-grid.

2.3. Final remarks

The (S)TEM techniques have been successfully applied in a wide range of studies in many fields. The techniques briefly described here were used to investigate both environmental and synthetic samples in the investigation reported in the present thesis. Most of them are available at the multi-user Center of Microscopy at the Universidade Federal de Minas Gerais, Belo Horizonte, Brazil. TEM allows the fully solid phase characterization with high spatial and energy resolution, down to few tenths of nanometres or even lower, by combining transmitted electrons image analysis, electron diffraction, EDX and EEL spectroscopies. Previous bulk analyses such X-ray fluorescence, X-ray diffraction, or even scanning electron microscopy are very helpful though. Any effort to use TEM in an exploratory study or to analyse an unknown sample is time consuming, and at the end it can become an expensive technique as the average academic user fee around the world is about US$ 45.00/hour.

2.4. References

Colliex, C. (2017). From a Physicist's Toy to an Indispensable Analytical Tool in Many Fields of Science: A Personal View of the Leading Contribution of Ondrej Krivanek to the Spectacular Successes of EELS Spectroscopy in the Electron Microscope. *Ultramicroscopy* (In press). DOI: 10.1016/j.ultramic.2016.11.007.

Colliex, C., Manoubi, T., Ortiz, C. (1991). Electron-Energy-Loss-Spectroscopy near-Edge Fine Structures in the Iron-Oxygen System. *Phys. Rev. B* vol. 44 (20): 11402–11.

Egerton, R. F. (2008). Electron Energy-Loss Spectroscopy in the TEM. *Reports Prog. Phys.* vol.72 (1): 16502. DOI: 10.1088/0034-4885/72/1/016502.

Elsass, F., Chenu, C., Tessier, D. (2008). Transmission Electron Microscoy for Soil Samples: Preparation Method and Use. In: Ulrey, A. L.; Drees, L. R. *Methods of Soil Analysis:* Part 5 – Mineralogial Methods. Madison: Soil Science Society of America. 235–268. DOI: 10.2136/sssabookser5.5c9.

Leapman, R. D. (2017). Application of EELS and EFTEM to the Life Sciences Enabled by the Contributions of Ondrej Krivanek. *Ultramicroscopy* (In press) DOI: 10.1016/j.ultramic.2017.01.002.

Leapman, R. D.; Hunt, J. A. (1991). Comparison of the detection limit for EELS and EDXS. *Microsc. Microanal. Microstruct.* vol. 2: 231-244. DOI: 10.1051/mmm:0199100202-3023100.

Morniroli, J. P., Ji, G., Jacob, D. (2012). A Systematic Method to Identify the Space Group from PED and CBED Patterns Part I - Theory. *Ultramicroscopy* vol. 121: 42–60. DOI: 10.1016/j.ultramic.2012.04.008.

Morniroli, J. P., Steeds, J. W. (1992). Microdiffraction as a Tool for Crystal Structure Identification and Determination. *Ultramicroscopy* vol. 45 (2): 219–239. DOI: 10.1016/0304-3991(92)90511-H.

Saitoh, K., Nakahara, H., Tanaka, N. (2013). Improvement of the Precision of Lattice Parameter Determination by Nano-Beam Electron Diffraction. *Microscopy* vol. 62 (5): 533–539. DOI: 10.1093/jmicro/dft023.

Williams, D. B.; Carter, C. B. (2009). Transmission Electron Microscopy; Second Edition. New York, USA: Springer New York.

CHAPTER 3. Natural attenuation of arsenic in the environment by immobilization in nanostructured hematite

Abstract

Iron (hydr)oxides are known to play a major role in arsenic fixation in the environment. The mechanisms for long-term fixation into their crystal structure, however, remain poorly understood, especially arsenic partitioning behaviour during transformation from amorphous to crystalline phases under natural conditions. In this study, these mechanisms are investigated in Al-Fe-rich Oxisols exposed over a period of 10 years to a sulfide concentrate in tailings impoundments. The spatial resolution necessary to investigate the markedly heterogeneous nanoscale phases found in the Oxisols was achieved by combining three different high resolution electron microscopy techniques – nano-beam electron diffraction (NBD), electron energy-loss spectroscopy (EELS), and high resolution transmission electron microscopy (HRTEM). Arsenic (1.6 ± 0.5 wt%) was unambiguously and precisely identified in mesocrystals of Al-hematite with an As/Fe atomic ratio of 0.026 ± 0.006 mol mol^{-1}. The increase in the *c*-axis ($c = 1.379 \pm 0.009$ nm) compared to standard hematite ($c = 1.372$ nm) is consistent with the presence of arsenic in the Al-hematite structure. The As-bearing Al-hematite is interpreted as a secondary phase formed from oxyhydroxides, such as ferrihydrite, during the long-term exposure to the As-sulfide tailings. The proposed mechanism of arsenic fixation in the Al-hematite structure involves adsorption onto Al-ferrihydrite nanoparticles, followed by Al-ferrihydrite aggregation by self-assembly oriented attachment and coalescence that ultimately produces larger crystals of Al-hematite. Our results illustrate for the first time the process of formation of stable arsenic bearing Al-hematite for the long-term immobilization of arsenic in environmental samples.

Keywords: Arsenic fixation, As partitioning, As speciation, long-term stability

3.1. Introduction

The release of As into the environment from geogenic sources is ultimately controlled by the chemical stability of As-bearing mineral phases. Therefore, the thorough structural and chemical characterization of these phases is necessary to fully assess As mobility in different environmental matrices. The chemical stability of solid As-bearing phases in aqueous systems is conventionally established using extraction methods designed to measure the degree of mobilization under specified environmental conditions, such as the toxicity characteristic leaching procedure – TCLP (Ghosh et al. 2004; Jong and Parry 2005, and sequential extraction methods and bioaccessibility tests (Cappuyns et al. 2002; Guo et al. 2007; Anawar et al. 2008; Karak et al. 2011; Larios et al. 2012a, 2012b). These procedures, however, provide only indirect evidence for As association with its host mineral phases while the actual nature of these phases remains unknown.

The structural characterization of As-bearing phases by traditional analytical techniques is not trivial, and in view of these difficulties, synchrotron-based analytical techniques combined with theoretical molecular modelling or with other spectroscopic techniques have been increasingly applied to investigate As distribution, speciation, and bonding characteristics, with advances in our understanding of As stability (Paktunc et al. 2008; Morin et al. 2009; Chakraborty et al. 2011; Duarte et al. 2012a). Transmission electron microscopy (TEM) techniques are especially useful for the characterization of solid phases at the nanoscale, with better spatial resolution than any other technique. However, few TEM investigations of As-bearing minerals have been described in the literature (Carlson et al. 2002; Ouvrard et al. 2005; Paktunc et al. 2008; Morin et al. 2009; Adra et al. 2013; Kendall et al. 2013). The difficulties in the accurate characterization of As compounds in environmental samples by conventional techniques lie in the markedly particles heterogeneity and small grain size. To overcome these dificulties we combined different TEM techniques such as nano-beam electron diffraction (NBD), energy dispersive X-ray spectroscopy (EDS), electron energy-loss spectroscopy (EELS), and high resolution transmission electron mmicroscopy

(HRTEM), which give the highest spatial resolution needed in the analyses of phases at nanoscale.

In this work, we used HRTEM, NBD, EDS and EELS to investigate the As-bearing phases and the distribution of As in Al-Fe-rich Oxisols used as liners in sulfide tailings disposal facilities. A recent study from our group (Duarte et al. 2012b) investigated As speciation in the same Oxisol liners as well as in the tailings after 10 years of disposal. The bulk analyses were done using a sequential extraction procedure (SEP), X-ray diffraction (XRD) and X-ray absorption spectroscopy near edge structure (XANES) analyses. Arsenic was found mainly as As(V) in the Oxisol samples and as arsenopyrite in the tailings. Up to 69% of the total As content in the Oxisol was found associated with Fe and Al crystalline phases, which were not dissolved even under strongly acidic and reduction conditions. This crystalline fraction of the Al-Fe-rich Oxisol liners is investigated in this present study, and it will be demonstrated that As is immobilized in the structure of secondary crystalline Al-hematite.

3.2. Materials and Methods

3.2.1. Samples description

The environmental samples investigated in this present Thesis are Al- and Fe- rich Oxisols provided by Kinross Brasil Mineração, from Morro do Ouro mine in Paracatu, northwestern Minas Gerais state, Brazil. The Morro do Ouro is an open mine whose ore deposits are mainly pyrite (Fe_2S) and arsenopyrite (FeAsS). Large amount of As-sulfide tailings is produced at the flotation step in the hydrometallurgical processing plant in this gold mine, and the concentrates of As-rich sulfide disposed in tailings impoundments. The Oxisol liners samples analysed in this present work had been used to seal tailings dams (hereafter called specific tanks) working as chemical barrier for arsenic uptake. The Oxisol had been selected out of other tested materials due to its high performance in As fixation (Ladeira et al. 2002; Ladeira and Ciminelli 2004). In 2011 and 2012, after about 10 years of As-sulfide tailings disposal, two of these specific tanks (namely T2 and T3) were excavated to reprocessed, and samples from both aged tailings and Oxisol liners recovered for analysis. Arsenate (As(V)) was the predominant specie in the aged tailings, mainly arsenopyrite and minor scorodite ($FeAsO_4.2H_2O$), which indicated there was no significant oxidation of As during the long-term disposal (Duarte et al. 2012b). Arsenate was also the arsenic specie found in the Oxisol liners (Duarte et al. 2012b; Silva et al. 2013). Table 3.1 shows the chemical composition of Oxisol liners exposed to the As-tailings as well as the geographical coordinates where they were sampled.

Table 3.1. Arsenic, aluminium and iron content (mg kg^{-1}) determined for Oxisol liner samples and the respective geographical coordinates, in the Universal Transverse Marcator (UTM) system, at zone 23 S. The samples are named after the date (ddmm) they were collected at the site. Data from Silva et al. (2003).

Oxisol liner sample (ddmm)	**UTM coordinates (metres)**		**As**	**Al**	**Fe**
	E	**W**		**(mg kg^{-1})**	
3105[a]	301800	8099150	3,101	13,478	12,823
1506[a]	301824	8090151	2,375	12,125	7,471
2106[a]	301900	8090208	3,660	146,012	153,352
2406[a]	301934	8090261	2,326	159,572	179,601
2706[a]	301927	8099209	2,761	136,032	143,388
3006[a]	301916	8099228	1,920	78,043	45,702
0507[a]	301925	8099208	2,160	87,826	84,873
1307[a]	301935	8099231	1,950	53,998	42,993
2806[b]	-	-	6,375	14,068	255,427

a) Samples collect in 2011 during the excavation of a specific tank T3; b) Sample collected in the specific tank T2, excavated in 2012. The UTM coordinates had not been measured for sample 2806.

The Oxisol liners (OL) samples had been analysed following a modified selection extraction procedure (SEP) after Pantuzzo and Ciminelli (2010) in order to assess the As partitioning. Table 3.2 shows the results reported in Silva et al. (2013) for samples 1307, 2106 and 2806 for which the mass balance was reached. These samples, henceforth named OL1, OL2, and OL3, respectively, include the Oxisol liners with the largest and lower As content.

Table 3.2. Sequention extraction procedure (SEP) for As extraction from Oxisol liner samples. Data from Silva et al. (2013).

SEP step	**Fraction**	**OL1**	**OL2**	**OL3***
		As extracted (%)		
1	Exchangeable (25 mL $NaNO_3$ 1 mol L^{-1}; 1 h shaker 25 ºC)	0.07	0.22	-
2	Adsorbed (25mL HCl 3 mol L^{-1}; 24 h shaker 70 ºC and washing)	8.50	9.70	11.66
3	Associated fo Fe- and Al- amorphous phases (25mL HNO_3 1:1 v v^{-1}; 3 h shaker 50 ºC)	5.00	4.90	3.15
4	Associated fo Fe- and Al- crystaline phases (HCl / HNO_3 / HF (4:2:2) v v^{-1}; 3 h shaker 80 ºC)	69.00	60.00	66.43
5	Residual (microwave digestion)	16.50	22.90	14.04
	Total	99.07	97.72	95.28

*A slightly different SEP was applied to As extraction from sample OL3, whose adsorbed fraction was extracted by phosphate

The majority of arsenic was found associated to crystalline Al- and Fe- phases (Silva et al. 2013). However, the actual As-containing crystalline phases in OL remained uknown. The crystalline fraction of samples OL1, OL2 and OL3 are then investigated in the present work, as well as a *fresh* Oxisol (FO) sample collected in the same mine area in 2014, which represents the Oxisol before the contact to the As-sulfide tailings.

3.2.2. XRD analysis

XRD analyses for mineral identification were performed using a Shimadzu 7000 (samples OL2 and OL3) or a Philips (PW 1710) Cu anode diffractometer (OL1 and FO) with a wavelength of 1.54 Å. The obtained diffractograms were compared with the database from the ICDD (International Centre for Diffraction Data).

3.2.3. Chemical analysis

To establish the As content, 0.5 g of sample was fused with sodium tetraborate in platinum crucibles at 900 °C in a muffle furnace and dissolved with 1:1 hydrochloric acid. Arsenic concentrations were measured in triplicate using a Perkin Elmer 7300 inductively coupled plasma with optical emission spectrometer (ICP-OES). Precision and accuracy measured against international reference materials were better than 95%.

3.2.4. TEM sample preparation and analysis

Suspension of the four samples was achieved by dispersion in distilled water in Eppendorf® tubes, and by sonication in an ultrasound bath for three minutes. Before sample loading, the carbon-coated Cu-TEM support grids (300 mesh) were subjected to a glow discharge process (Bal-Tec Sputter MD20) for approximately 15 seconds, using an Ar plasma to ionize the grids (Ayache et al. 2010). A drop of particle suspension was placed on the surface of a Petri dish filled with distilled water to form a thin film of fine particles (Langmuir film) on the water surface, and then the carbon film side of the TEM grid was placed in contact with the fine particles spread on the water surface to pick up the solids.

The four samples were analysed using four different transmission electron microscopy techniques: HRTEM, NBD, EDX and EEL spectroscopies. The HRTEM, NBD and Spot EDS analyses were performed in the Centre of Microscopy at the Universidade Federal de Minas Gerais (UFMG), Brazil, using a LaB_6-TEM Tecnai G^2 20 SuperTWIN (FEI), at 200 kV, equipped with a Si(Li) EDS detector (EDAX) with a 30mm² window. The EDS mapping and the EELS analyses were performed in the Brazilian Nanotechnology National Laboratory (LNNano/LNLS) using a FEG-TEM JEM 2100F (JEOL), at 200 kV, equipped with EDS (Noran), high-angle annular dark field (HAADF) detector and a Gatan Imaging Filter (GIF) Tridiem system. The JEMS software (Stadelmann 1987) was used for the electron diffraction analysis.

After the phase identification, the indexed NBD patterns were used to refine the lattice parameters following a recently developed method (Saitoh et al. 2013) which takes into account the *hkl* reflections observed in the zeroth-order Laue zone (ZOLZ) and first-order Laue zone (FOLZ). The *hkl* reflection positions of the NBD pattern are displaced due to the distortion in the projector lens system of the TEM. Nevertheless, these displacements (Δx, Δy) are proportional to the distortion coefficients (C_{radial}, C_{spiral}, and $C_{elliptical}$) of the projector lenses and can be calculated as follows (Saitoh et al. 2013)

$$\begin{cases} \Delta x = C_{radial}.r^3.cos\emptyset - C_{spiral}.r^3.sin\emptyset + C_{elliptical}.r.cos(\emptyset - \emptyset_{ell}) \\ \\ \Delta y = C_{radial}.r^3.sin\emptyset + C_{spiral}.r^3.cos\emptyset - C_{elliptical}.r.sin(\emptyset - \emptyset_{ell}) \end{cases} \tag{3.1}$$

where r and ϕ are the radial coordinate and the azimuthal angle, respectively, of the *hkl* spot, whose origin is the coordinate of the microscope optical axis (x_{opt}, y_{opt}). The parameter ϕ_{ell} is the angle between the main axis of elliptical distortion and the horizontal axis (x) on the CCD.

The distortion coefficients were determined prior to analysis by fitting the spot positions between the experimental and simulated NBD patterns (See Appendix 1) of a known sample of silicon (Si; *F*d-3m, a = 5.4309 Å), along the ⟨111⟩ zone axis. The fit was done by minimizing the *chi*-square residual sum defined as follows (Saitoh et al. 2013)

$$X^2 = \sum_{i=1}^{N} \left\{ \left(\frac{x_i^{exp} - x_i^{sim}}{\sigma_{xi}} \right)^2 + \left(\frac{y_i^{exp} - y_i^{sim}}{\sigma_{yi}} \right)^2 \right\} \tag{3.2}$$

where (x^{exp}, y^{exp}) and (x^{sim}, y^{sim}) are the spot position coordinates, in pixel units, of the experimental and simulated NBD patterns, respectively. The parameters σ_{xi} and σ_{yi} are the errors in the measurement of each spot position, in pixel units, in the experimental NBD pattern, and were equivalent to 2 pixels, or 0.19 nm^{-1} on average.

The distortion coefficients, C_{radial}, C_{spiral}, and $C_{elliptical}$, were estimated as 10^{-9}, 10^{-9} and 10^{-2}, respectively. Once the distortion coefficients were determined, the same procedure was followed to calculate the displacements (Δx, Δy) of *hkl* reflections observed in the NBD patterns performed for the Oxisol liner samples. These NBD patterns were performed using the same experimental conditions used for the Si sample (200 kV, camera length of 300 mm, and convergence semi-angle of 1.3 mrad).

3.3. Results and discussion

3.3.1. Fresh Oxisol

The chemical analysis showed that the arsenic content in the FO sample was 12 ± 7 mg kg^{-1}. The main phases identified by XRD analysis (Figure 3.1) were quartz, kaolinite, gibbsite, muscovite, hematite, and goethite. TEM analysis showed the presence of ferrihydrite, hematite (Figure 3.2), and goethite. Aluminium was identified in all these phases by the EDS analysis. Arsenic was below the EDS detection limit (approx. 1 wt%).

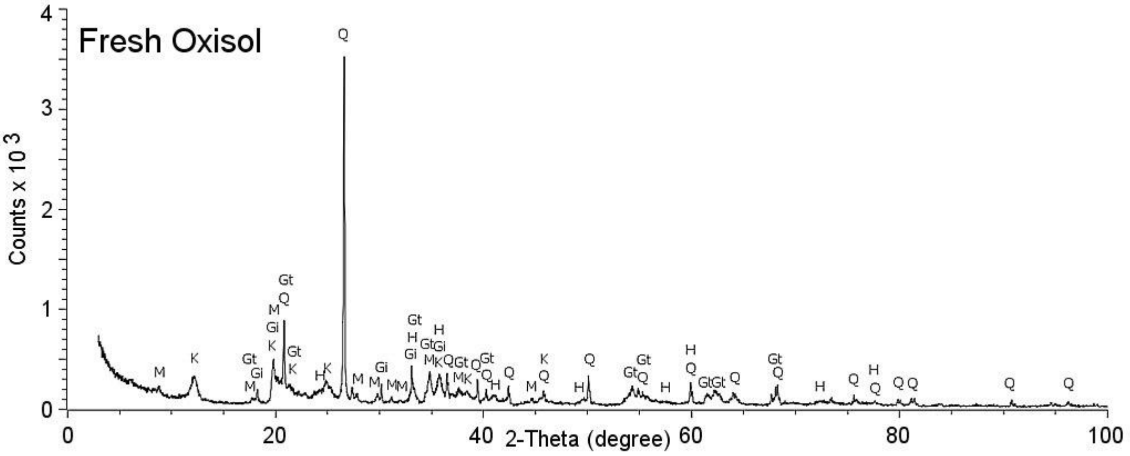

Figure 3.1. X-ray diffractogram of *fresh* Oxisol sample. Q – quartz; K – kaolinite; Gi – gibbsite; M – muscovite; H – hematite; Gt – goethite.

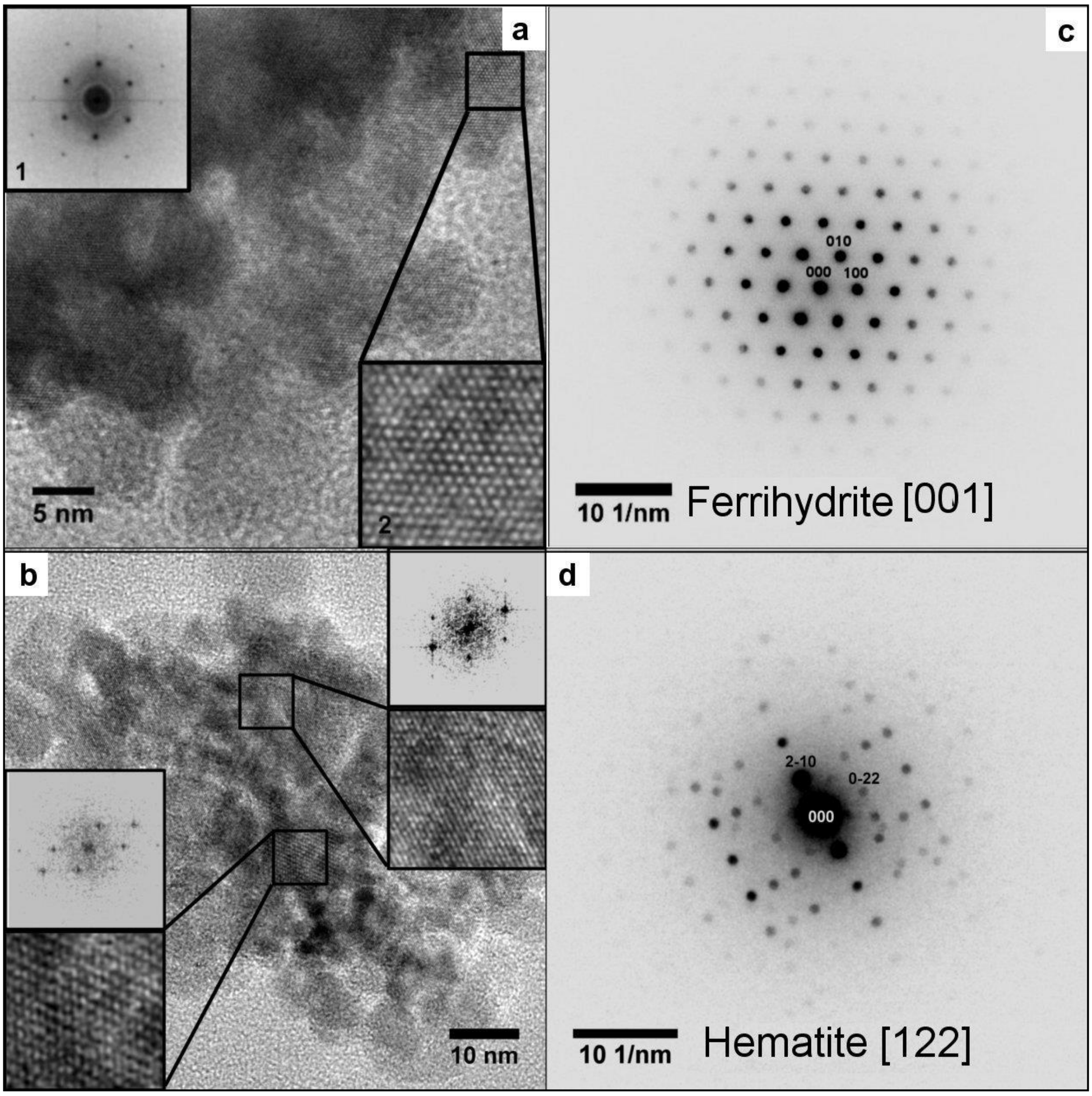

Figure 3.2. HRTEM images of a (a) ferrihydrite and (b) hematite nanoparticle aggregates in sample FO. Insets in images (a) and (b) show the detailed HRTEM images inside the indicated square and the corresponding FFT taken from these areas. (c) [001] zone axis NBD pattern of the ferrihydrite nanoparticle aggregate shown in image (a); (d) [122] zone axis NBD pattern of the hematite nanoparticle aggregate shown in image (b).

3.3.2. Oxisol liner

The main mineral phases identified by XRD analysis of the bulk Oxisol liner samples (OL1, OL2 and OL3) were quartz, mica, albite, hematite, goethite, kaolinite, siderite, and gibbsite. To investigate which phase bears As, the TEM analysis were performed. The TEM analyses showed that the crystalline fraction of Oxisol liner samples are composed of phyllosilicates and crystalline nanoparticle aggregates of Al-Fe-(hydr)oxides. Figure 3.3 shows the typical bright field TEM images of these phyllosilicates and the Al-Fe-(hydr)oxides' aggregates, and the EDX spectra of the regions where As was found. The C and Cu signals in such EDX spectra originated from the carbon-coated Cu-TEM support grids due stray electrons.

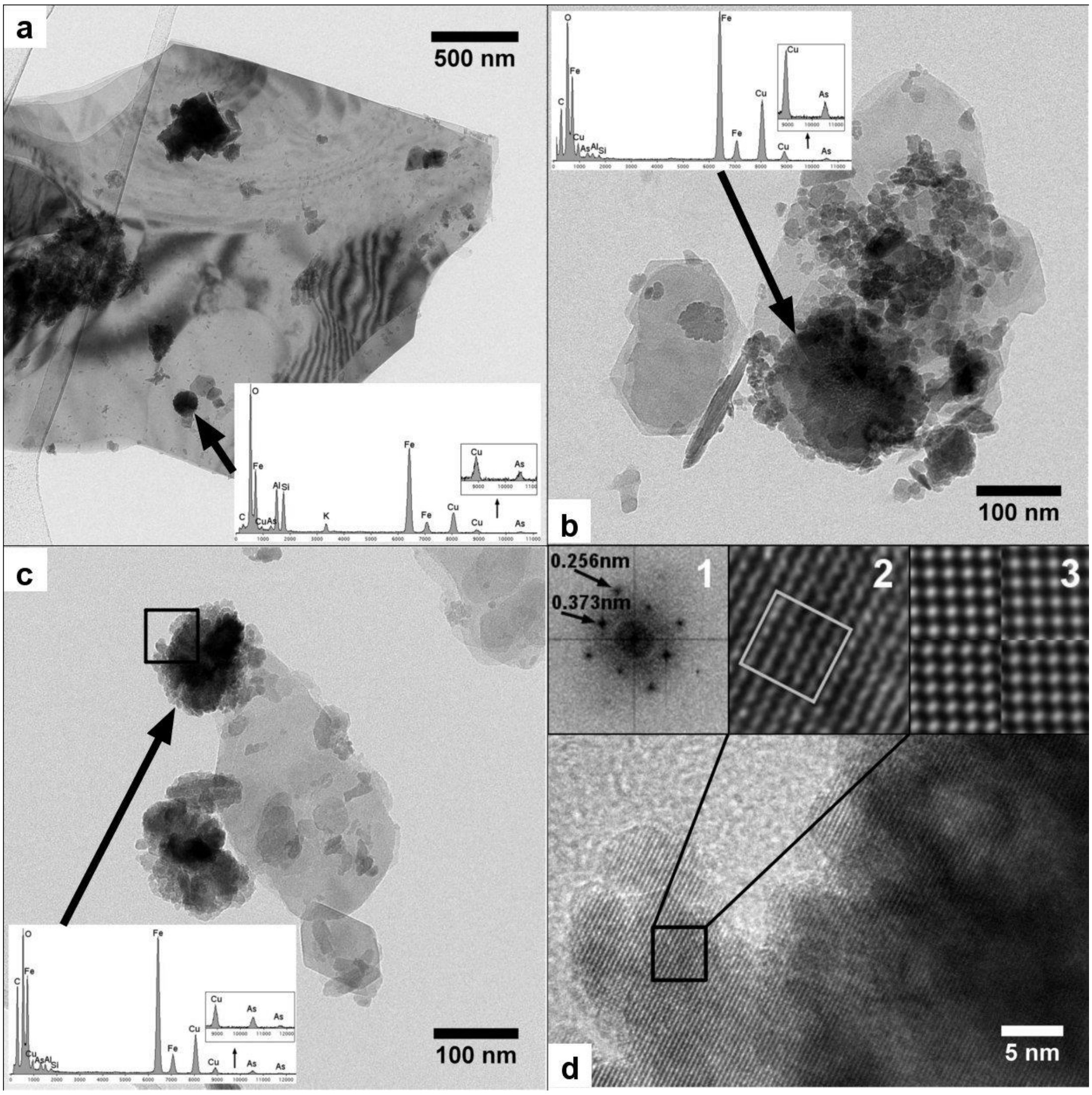

Figure 3.3. Typical Bright Field TEM images of Oxisol liner samples showing phyllosilicate plates and some Fe-Al-(hydr)oxide aggregates. EDX spectra taken from different nanoparticle aggregates are shown in image (a) for sample OL1, and in images (b-c) for sample OL3. (d) HRTEM image of the area inside the black square in (c). Insets 1, 2 and 3 in (d) show, respectively, the FFT of the whole image (b), the magnified HRTEM of the region inside the black square in (d), and four simulated HRTEM images of the $[\bar{4}\,\bar{2}\,1]$ zone axis of hematite, in different defocus values. The experimental HRTEM (d.2) is rotated in relation to the simulated images.

EDX spectra taken from many different points showed that As was found only in the crystalline Al-Fe aggregates, as indicated by the arrows in Figures 3.3.a-c. The EDS maps of a typical aggregate not associated to phyllosilicates (Figure 3.4) show As and

Al well dispersed within the crystal, suggesting they may be incorporated in structure of the Al-Fe-(hydr)oxide.

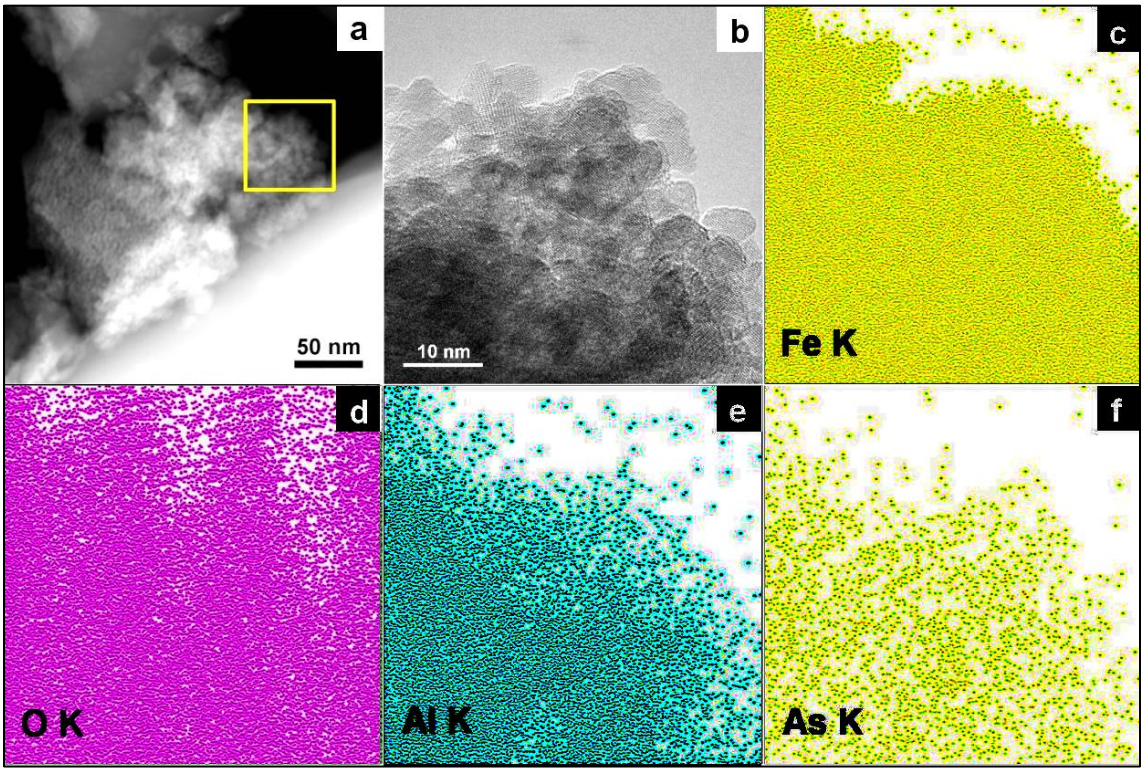

Figure 3.4. (a) HAADF of a crystalline particle aggregate in sample OL1; (b) HRTEM of the region highlighted in (a) showing the aggregate; (c) to (f) EDS maps of (b). The O K signal extends beyond the sample due instrumental noise.

The aggregate shown in Figure 3.3.d was further investigated by HRTEM analysis. The interlayer distances were measured from the Fast Fourier Transform (FFT) of the HRTEM image (Inset 1 of Figure 3.3.d). The distances of 0.373 nm and 0.256 nm correspond to the d_{hkl} of hematite reflections (102) and (110), respectively. Based on these (hkl) planes, the aggregate was identified as hematite, along the $[\bar{4}\bar{2}1]$ zone axis. In addition, HRTEM image simulations were done for a standard hematite crystal structure (R-3c, a_{std} = 0.5035 nm and c_{std} = 1.372 nm) along the $[\bar{4}\bar{2}1]$ zone axis using the JEMS software (Stadelmann 1987). Inset 3 in Figure 3.3.d shows that the four simulated HRTEM in different defocus conditions are in good agreement with the experimental HRTEM image (inset 2 in Figure 3.3.d), thus confirming the identification of hematite.

The aggregates shown in Figures 3.3.a and 3.3.b were also identified as hematite by the NBD analysis. The NBD patterns of these aggregates were indexed as the ⟨301⟩ and ⟨001⟩ zone axes of hematite (Figures 3.5.a.1 and 3.5.b.1). The refinement of the lattice parameters of hematite found in samples OL1 and OL3 followed the method described above (Saitoh et al. 2013), and the *a* and *c* unit-cell lengths were calculated based on the corrected *hkl* reflection positions observed in the NBD patterns. The refinement showed an excellent fit (99.38% precision, consistent with a 0.62% error as reported by Saitoh et al. 2013) with fifty-two and twenty-five reflections, respectively (See Appendix 1). The lattice parameters were determined as $a = 0.498 \pm 0.003$ nm and $c = 1.379 \pm 0.009$ nm for the hematite identified in sample OL1. For the calculation of the *c* lattice parameter, the standard *a* value ($a_{\text{std}} = 0.5035$ nm) was kept constant. A slightly larger lattice parameter ($a = 0.503 \pm 0.004$ nm) was determined for the sample in OL3. The *c* value could not be calculated because the Miller index *l* of all the indexed ZOLZ reflections was equal to zero (The lattice parameters were calculated by using the Equations A.2 and A.3; See Appendix 1)

The *a*-unit-cell length of hematite found in sample OL1 ($a = 0.498 \pm 0.003$ nm) is shorter than the standard value ($a_{\text{std}} = 0.5035$ nm), and this is attributed to the substitution of the larger Fe^{3+} with the smaller Al^{3+} ions. Based on EDS analysis, the ratio Al/(Al+Fe) found for hematite in sample OL1 was 24.26 mol%. This value is larger than the maximum Al-substitution (~16% mol mol^{-1}) of hematite synthesised at 100 ºC (Schwertmann et al. 1979, 2000; Cornell and Schwertmann 2000). Our results, however, are consistent with the linear relationship described in the literature (Cornell and Schwertmann 2000) between the *a*-axis length and the Al-substitution in hematite, whose expected *a*-values for 24.26% mol mol^{-1} of Al are 0.5004 nm or 0.5001 nm for hematite formed at 25 ºC and 70 ºC, respectively (Schwertmann et al. 1979, 2000; Cornell and Schwertmann 2000). The *a* parameter ($a = 0.503 \pm 0.004$ nm) calculated for hematite in sample OL3 with Al/(Al+Fe) = 1.95% mol mol^{-1} (i.e., relatively low Al content) is also consistent with $a = 0.50342$ nm for Al-hematite with 1.8% mol mol^{-1} Al substitution formed from Al-ferrihydrite aged for 77 days at pH 7 and 70 ºC (Schwertmann et al. 1979).

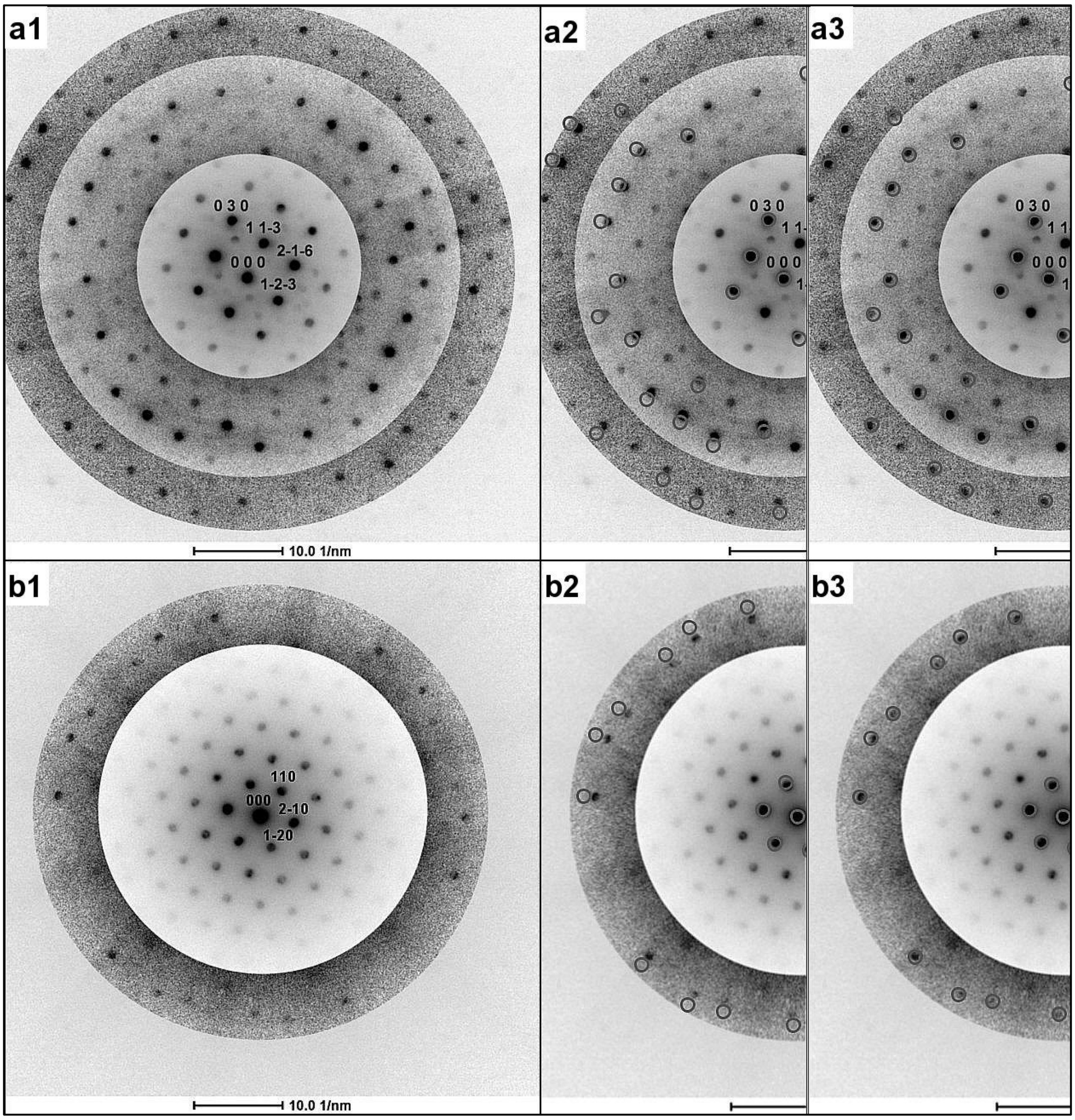

Figure 3.5. NBD patterns of the aggregates of sample OL1 (a1) shown in Figure 3.2.a, indexed as [301] ZA of hematite (α-Fe_2O_3), and of sample OL3 (b1) shown in Figure 3.2.b, indexed as [001] ZA of hematite; (a2) and (b2): NBD patterns of (a1) and (b1), respectively, with some spots overlaid with simulated reflection positions without distortion correction; (a3) and (b3): NBD patterns of (a1) and (b1), respectively, with some spots overlaid with reflection positions with distortion correction.

Values of *a* between 0.503 nm and 0.504 nm have also been reported for 0-3.0 mol% Al-substitution in hematite formed from ageing ferrihydrite for 17-19 years at 25 ºC and pH 5-7 (Schwertmann et al. 2000). These values may approximate the natural conditions for Al-hematite formation.

The Al for Fe substitution in synthetic hematite affects the *a*-unit-cell length, but does not seem to affect significantly the *c* length of unheated Al-hematite (Schwertmann et al. 1979, 2000). On the other hand, the presence of As within the hematite structure increases the *c*-axis, but does not seem to affect the *a*-axis (Bolanz et al. 2013b). The *c* lattice parameter refined for the As-bearing hematite (As ~1.7 wt%) in sample OL1 (c = 1.379 ± 0.009 nm) is slightly larger than that of standard hematite (c_{std} = 1.372 nm). This result is consistent with the increase in the *c*-axis of hematite (1.3769 nm to 1.3785 nm) observed for increasing As(V) concentrations (0.00 wt% to 2.64 wt%) reported in the literature (Bolanz et al. 2013b). The detailed understanding of the As distribution pattern and its mechanisms of incorporation within the Al-hematite is being further investigated.

Hematite was also identified by EELS performed in the Al-As-bearing aggregate shown in Figure 3.4.a, in the sample OL1. The EELS O K-edge of Fe-oxides are reported as being a fingerprint of each phase (Colliex et al. 1991; Golla-Schindler et al. 2006). Many Fe-oxides can be identified through the distinct peaks in the O K-edge, and these have been labelled in Figure 3.6. Hematite was identified by comparing the experimental spectra with those reported in the literature (Colliex et al. 1991). Indeed, hematite was confirmed by HRTEM and NBD analyses.

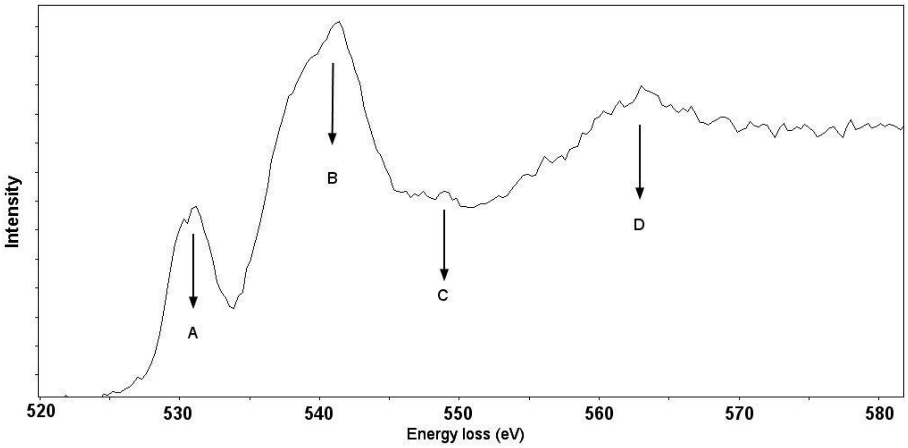

Figure 3.6. EELS O K-edge experimental spectrum of hematite in sample OL1, taken of the same region shown in Figure 2.a. The achieved energy resolution was 1 eV. A, B, C and D are the main peaks of hematite according to Colliex et al. (1991).

The As/Fe atomic ratio (R) was determined from the EDS analysis performed for 26 different Fe and Al aggregates from samples OL1 (R = 0.028 ± 0.007 mol mol^{-1}), OL2 (R = 0.027 ± 0.006 mol mol^{-1}) and OL3 (R = 0.024 ± 0.003 mol mol^{-1}). The error in the EDS peak identification is around 1% (Williams and Carter 2009). The As/Fe molar ratio of approximately 0.03 mol mol^{-1} found in Oxisol liner samples is in agreement with the range reported in the literature (Galvez et al. 1999; Violante et al. 2007; Bolanz et al. 2013a, 2013b; Wang et al. 2015). These ratios seem to be crucial for hematite crystallization from As-doped ferrihydrite; hematite crystallizes instead of goethite at neutral pH for As/Fe molar ratio between 0.01 and 0.06 mol mol^{-1}, with saturation at molar ratio of 0.06 mol mol^{-1} (Bolanz et al. 2013a). Even though the controlled laboratory experiments do not reproduce the actual environmental conditions, it is noteworthy that the same association between As and synthetic hematite has been observed in the Oxisol liners considered in this study.

Arsenic-bearing Al-goethite was also identified in sample OL1 using selected area electron diffraction (SAD) and EDS analyses (Figure 3.7), but Al-hematite was the predominant As-bearing phase in all the Oxisol liners. In average, larger amount of As was found in Al-goethite relatively to Al-hematite, though the largest As content (3.23 wt%) was found for Al-hematite (Table 3.3). In addition, the increased As content (wt%) is observed for Al-hematite with an increase in the Al/(Al+Fe) molar ratio, but no trend is observed for Al-goethite.

Table 3.3. As and Al content found in hematite (H) and goethite (G) crystals from EDS analysis of the Oxisol samples, and the molar ratios As/(As+Fe) and Al/(Al+Fe) calculated from EDS data.

Phase	**H1**	**H2**	**H3**	**H4**	**H5**	**G1**	**G2**	**G3**	**G4**	**G5**
As (wt%)	0.90	0.99	1.50	1.84	3.23	1.20	1.50	1.70	2.30	2.40
Al/(Al+Fe) (% mol mol^{-1})	4.00	4.85	6.50	7.30	10.18	18.03	10.95	19.84	17.10	16.11

Co-precipitation of Al with Fe in 16-19 year-long experiments affected not only the unit cell parameters, but also influenced the phase transformation process (Schwertmann et al. 2000). In a series of experiments carried out at pH 4-7 at 25 °C, it was shown that hematite is the dominant or only crystalline phase, and that the presence of Al in the system (Al/(Fe+Al) between 0 and 0.17 mol mol^{-1}) hampers the crystallization of goethite from ferrihydrite and favours the formation of Al-hematite (Schwertmann et al. 2000). The lesser occurrence of goethite relative to hematite in the Oxisol liners exposed to As-tailings for over ten years in our study is therefore consistent with the findings for synthetic samples aged for 16-19 years (Schwertmann et al. 1979, 2000, 2004). It is also consistent with findings of an investigation on co-precipitation of As, Al and Fe (Violante et al. 2009). The presence of up to 1.8 wt% As(V) in hematite nanocrystals synthesised from ferrihydrite has been reported (Bolanz et al. 2013b), however the incorporation of As in naturally-formed hematite has been documented for the first time in this study. The mechanism of As incorporation into Al-hematite will be considered in the next paragraphs.

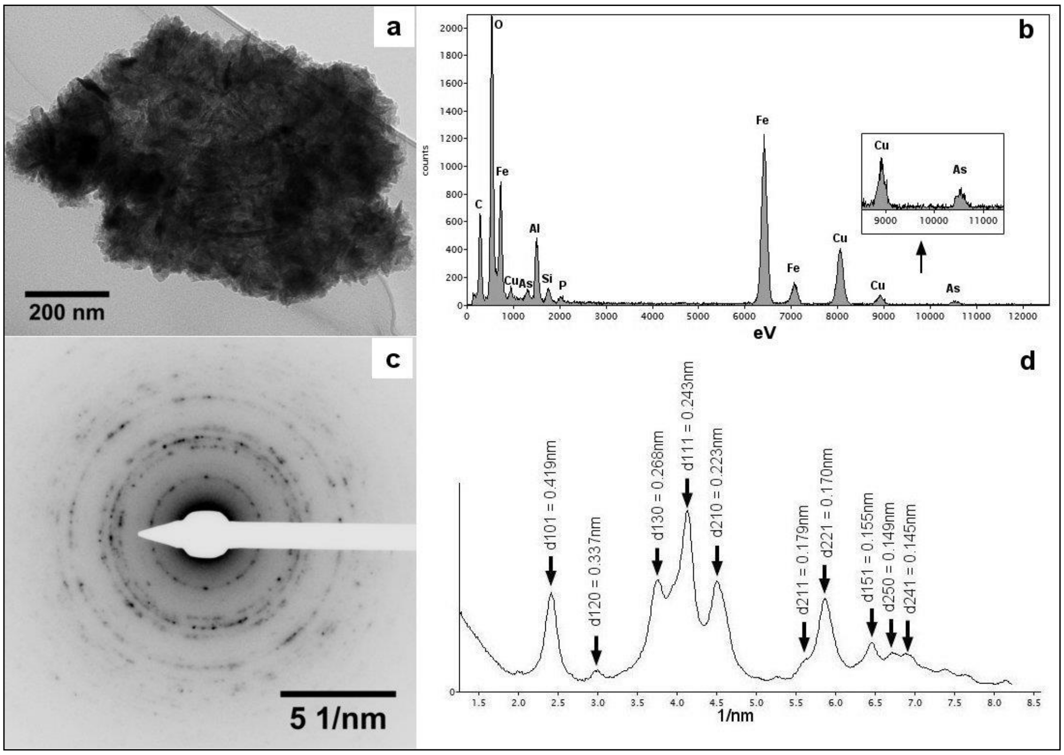

Figure 3.7. (a) Bright Field TEM image of and aggregate of Al-Goethite; (b) EDS spectra taken of the whole aggregate; (c) SED pattern of the Al-Goethite shown in image (a); (d) Profile of the rotational average performed in image (c), and showing the *d*hkl distances of Al-Goethite.

The direct incorporation of As into existing hematite tetrahedral interstices is unlikely to happen due to the close packed hematite structure. In a recent work, Bolanz et al. (2013b) proposed a mechanism to explain the incorporation of As(V) in the hematite, in which the (210) planes of angelellite ($Fe_4As_2O_{11}$) might be grown epitaxially interlaid with the (0001) planes of hematite. This model fitted their XANES and extended X-ray absorption fine structure (EXAFS) data, although neither the X-ray nor the electron diffraction analyses could confirm the presence of angelellite.

The morphology of the As-bearing Al-hematite crystals in the Oxisol liners suggests a mechanism of crystal growth different from that proposed by Bolanz et al. (2013b). The Al-hematite phase consists of well-oriented crystalline nanoparticles, very similar to hematite mesocrystals grown by a non-classical oriented aggregation based crystal growth process (Niederberger and Cölfen 2006; Cai et al. 2014, Lv et al. 2014). A mechanism is proposed for the incorporation of As into hematite, in which Al-ferrihydrite nanoparticles act as a template. According to this mechanism illustrated in Figure 3.8, As is adsorbed onto existing or newly-formed Al-ferrihydrite, thus modifying its surface properties. The Al-ferrihydrite nanoparticles then aggregate through a self-assembling oriented attachment process, ultimately resulting in oriented aggregates’ crystals of hematite by ageing. During attachment events the nanoparticles of Al-ferrihydrite collide with each other, and accommodate in a self-assembly aggregation. This process acts as trap for As, and once the attachment takes place, the As is immobilized in the new formed mesocrystal structure and never escapes it. The formation of goethite as an intermediate step in the transformation of ferrihydrite to hematite cannot be dismissed.

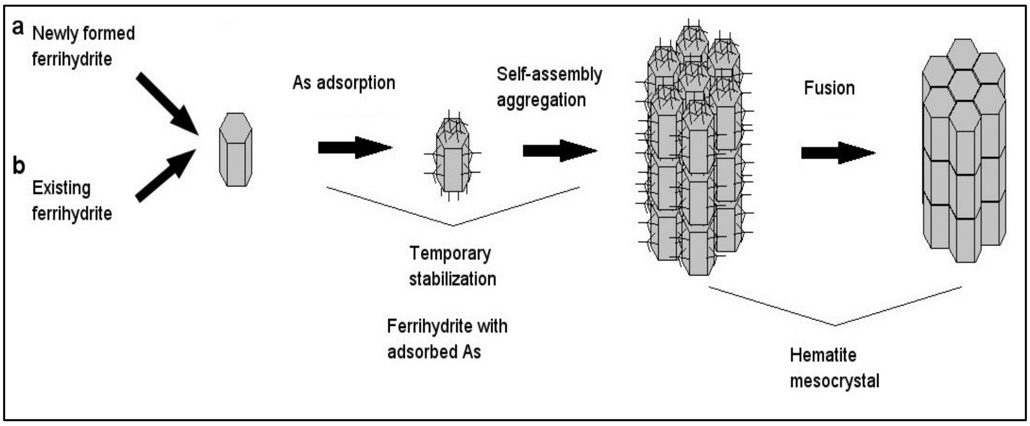

Figure 3.8. Schematic models for hematite formation from ferrihydrite nanoparticles *via* oriented attachment processes. (a) Newly formed or (b) existing ferrihydrite nanoparticles adsorb As, thus promoting instability in the nanoparticle by changing its surface energy. The irreversible self-assembly aggregation of the nanoparticles takes place to reduce their surface energy, and adsorbed As is then trapped inside the mesocrystal. The aggregation leads to interface elimination and hematite mesocrystals are ultimately formed by ageing.

The mechanism of oriented aggregation (OA) describes how primary nanoparticles assemble and aggregate following the same crystallographic direction (Niederberger and Cölfen 2006; Zhang and Banfiel 2012; Cai et al. 2014; Lv et al. 2014; Penn and Soltis 2014; Xue et al. 2014). The driving force for crystal growth through OA is surface energy reduction following nanoparticle attachment. In general, two nanoparticles in solution may collide and rotate until they face each other in a particular plane, and make an attachment in order to reduce the total energy of the formed compound. In the same way, other nanoparticles will be attached to the newly formed compound following a particular crystallographic direction, thus forming mesocrystals. Upon ageing, the mesocrystals evolve to more crystalline oriented aggregates. In the natural environment, other aggregation-based mechanisms of crystal growth, such as Ostwald Ripening (OR) and coarsening, can take place simultaneously along with OA, but the HRTEM results support OA as the mechanism able to account for the formed secondary Al-hematite and the likely process of As immobilization in its crystal structure.

The uptake of metals and contaminants in aqueous solution through the aggregation-based crystal growth mechanism was discussed by Waychunas et al. (2005), who pointed out that adsorbed species may be trapped within the Fe-(hydr)oxide nanoparticle aggregates. Part of the trapped species will be released again into the solution only if the solid is dissolved and the sorbate surfaces are exposed again to the solid/water interface. Primary nanoparticles are deemed to be attached in an irreversible way (Penn and Soltis 2014; Xue et al. 2014). The adsorption of some species can either promote or inhibit the aggregation of nanoparticles by OA (Xue et al. 2014), however it is believed that the As species adsorbed onto the existing or newly formed Al-ferrihydrite nanoparticles favoured the aggregation-based crystal growth of the Al-hematite mesocrystals in the Oxisol samples. This hypothesis is supported by our HRTEM data and also by the findings of Violante et al. (2009), who showed that co-precipitated products of As, Al and Fe at low As/(Al+Fe) molar ratios of 0.01 and 0.1 mol mol^{-1} transform from short-ranged phases to more ordered and crystalline phases by ageing. Violante et al. (2009) reported the formation of hematite from Al-ferrihydrite and other separate Al-oxide phases as well, which is attributed to the relatively high initial concentration of Al in their experiments (Al:Fe = 1 mol mol^{-1}). The actual role of Al needs further investigation, but it is known that Al in the system increases the surface area of ferrihydrite, thus improving its adsorption capacity (Masue et al. 2007; Violante et al. 2009), slows down phase transformation into hematite, and gives more stability to these phases (Taylor and Schwertmann 1978; Schwertmann et al. 1979; Violante et al. 2009).

The Oxisol liners samples considered in this study were shown to contain As(V) in association with Fe and Al crystalline phases, while no As(III) was identified (Duarte et al. 2012b), however the nature of these phases had not been established. This As-bearing mineral phase has now been identified as Al-hematite. It is noteworthy that the As species in the ore and in the As-sulfide tailings before hydrometallurgical processing was predominantly arsenopyrite with minor scorodite. It is assumed that As was released from the tailings by a process involving the dissolution of scorodite or arsenopyrite oxidation, and then infiltrated the Oxisol liners. Arsenic adsorption on Fe-(hydr)oxiders followed by oriented attachment and ageing led to As fixation in the Al-hematite structures.

3.4. Environmental implications

The proposed mechanism for As fixation into the Al-hematite structure accounts for As immobilization in Al- Fe-(hydr)oxides present in the Oxisols, and can be viewed as a natural remediation process. The high concentrations of Al in Oxisols enhance As uptake by increasing the surface area of ferrihydrite, and may improve the long-term stability of As-bearing hematite under reducing conditions. An intermediate Al-goethite phase is likely to form at some stage of the process, but hematite is the stable, end product of this Fe-(hydr)oxides phase transformation at neutral pH. Our findings support a mechanism of As fixation in the crystal structure of Al-hematite responsible for the immobilization of the largest amount of As in the aged Al-Fe-rich Oxisol used as liner and chemical barrier for long-term disposal of As-sulfide tailings.

3.5. Conclusions

The mechanism of As immobilization in natural Al-Fe-rich Oxisol was investigated. An Oxisol liner was exposed to As-bearing sulfide tailings for over 10 years in a gold mine site. Although the role of Al- or Fe-(hydr)oxides in As fixation is well established, our work showed for the first time significant amounts of As (1.6±0.5 wt%) distributed in crystalline Al-hematite with an As/Fe atomic ratio of 0.026 ± 0.006 mol mol^{-1}. The presence of As in the Al-hematite structure is consistent with a slight increase of the *c*-axis (c = 1.379 ± 0.009 nm) compared to the standard hematite structure (c=1.372 nm), which is interpreted as a secondary phase formed from Al-ferrihydrite during the long-term exposure of the Oxisol liner to As-bearing sulfide tailings.

The spatial resolution necessary to investigate markedly heterogeneous nanoscale phases in environmental samples was achieved through a combination of three different electron microscopy techniques (HRTEM, NBD and EELS). Arsenic was unambiguously and precisely identified in association with oriented aggregates of Al-hematite. This finding supports a mechanism of As fixation in the Al-hematite structure that involves As adsorption onto Al-ferrihydrite nanoparticles, followed by Al-ferrihydrite aggregation in a process of self-assembly oriented attachment to produce

Al-hematite mesocrystals. Our results demonstrate for the first time the existence of As-bearing Al-hematite in environmental samples. The mechanism proposed in this study highlights the role of Al-hematite in the long-term immobilization of arsenic.

3.6. References

Adra, A.; Morin, G.; Ona-Nguema, G; Menguy, N.; Maillot, F.; Casiot, C.; Bruneel, O.; Lebrun, S.; Juillot, F.; Brest, J. (2013). Arsenic Scavenging by Aluminum-Substituted Ferrihydrites in a Circumneutral pH River Impacted by Acid Mine Drainage. *Environ. Sci. Technol*. vol 47 (22): 12784–12792. DOI: 10.1021/es4020234.

Anawar, H. M., Garcia-Sanchez, A., Santa Regina, I. (2008). Evaluation of Various Chemical Extraction Methods to Estimate Plant-Available Arsenic in Mine Soils. *Chemosphere* vol. 70: 1459–1467. DOI: 10.1016/j.chemosphere.2007.08.058.

Ayache, J., Beaunier, L., Boumendil, J., Ehret, G., Laub, D. (2010). *Sample Preparation Handbook for Transmission Electron Microscopy*. New York, USA: Springer New York. DOI: 10.1007/978-1-4419-5975-1.

Bolanz, R. M., Bläss, U., Ackermann, S., Ciobotă, V., Rösch, P., Tarcea, N., Popp, J., Majzlan, J. (2013a). The Effect of Antimonate, Arsenate, and Phosphate on the Transformation of Ferrihydrite to Goethite, Hematite, Feroxyhyte, and Tripuhyite. *Clays Clay Miner*. vol. 61 (1): 11–25. DOI: 10.1346/CCMN.2013.0610102.

Bolanz, R. M., Wierzbicka-Wieczorek, M., Čaplovičová, M., Uhlík, P., Göttlicher, J., Steininger, R., Majzlan, J. (2013b). Structural Incorporation of As5+ into Hematite. *Environ. Sci. Technol*. vol. 47 (16): 9140–9147. DOI: 10.1021/es305182c.

Cai, J., Chen, S., Ji, M., Hu, J., Ma, J., Qi, J.. (2014). Organic Additive-Free Synthesis of Mesocrystalline Hematite Nanoplates via Two-Dimensional Oriented Attachment. *Cryst. Eng. Comm*. vol. 16: 1553-1559. DOI: 10.1039/c3ce41716f.

Cappuyns, V., Van Herreweghe, S., Swennen, R., Ottenburgs, R., Deckers, J. (2002). Arsenic Pollution at the Industrial Site of Reppel-Bocholt (north Belgium). *Sci. Total Environ*. vol. 295: 217–240.

Carlson, L., Bigham, J. M., Schwertmann, U., Kyek, A., Wagner, F. (2002). Scavenging of As from Acid Mine Drainage by Schwertmannite and Ferrihydrite: A Comparison with Synthetic Analogues. *Environ. Sci. Technol.* vol. 36 (8): 1712–1719. DOI: 10.1021/es0110271.

Chakraborty, S., Bardelli, F., Mullet, M., Greneche, J-M., Varma, S., Ehrhardt, J-J., Banerjee, D., Charlet, L. (2011). Spectroscopic Studies of Arsenic Retention onto Biotite. *Chem. Geo*. vol. 281: 83–92. DOI: 10.1016/j.chemgeo.2010.11.030.

Colliex, C., Manoubi, T., Ortiz, C. (1991). Electron-Energy-Loss-Spectroscopy near-Edge Fine Structures in the Iron-Oxygen System. *Phys. Rev. B* vol. 44 (20): 11402–11411.

Cornell, R.M., Schwertmann, U. (2000). *The Iron Oxides*: Structure, Properties, Reactions, Occurrences and Uses. Second Edition. Weinheim, Germany. Wiley-VHC.

Duarte, G., Ciminelli, V. S. T., Dantas, M. S. S., Duarte, H. A., Vasconcelos, I. F., Oliveira, A. F., Osseo-Asare, K. (2012a). As(III) Immobilization on Gibbsite: Investigation of the Complexation Mechanism by Combining EXAFS Analyses and DFT Calculations. *Geochim. Cosmochim. Acta* vol. 83: 205–216. DOI: 10.1016/j.gca.2011.12.019.

Duarte, G., Ciminelli, V. S. T., Gasparon, M., Mello, J. W. V. (2012b). Evaluation of 10 Years Stability of Concentrated As-Sulfide Tailings. In: Jack, C. N., Noller, B N., Naidu, R., Bundschuh, J., Bhattacharya, P. *Proceedings of the 4th International Congress on Arsenic in the Environment* - Understanding the Geological and Medical Interface of Arsenic – As 2012. Cairns, Australia. 423–425.

Galvez, N., Barron, V., Torrent, J. (1999). Effect of Phosphate on the Crystallization of Hematite, Goethite, and Lepidocrocite from Ferrihydrite. *Clays Clay Miner*. vol. 47 (3): 304–311.

Ghosh, A., Mukiibi, M., Ela, W. (2004). TCLP Underestimates Leaching of Arsenic from Solid Residuals under Landfill Conditions. *Environ. Sci. Technol*. vol. 38 (17): 4677–4682. DOI: 10.1021/es030707w.

Golla-Schindler, U., Hinrichs, R., Bomati-Miguel, O., Putnis, A. (2006). Determination of the Oxidation State for Iron Oxide Minerals by Energy-Filtering TEM. *Micron* vol. 37 (5): 473–477. DOI: 10.1016/j.micron.2005.11.002.

Guo, H., Stüben, D., Berner, Z. (2007). Adsorption of arsenic(III) and arsenic(V) from Groundwater Using Natural Siderite as the Adsorbent. *J. Colloid Interface Sci.* vol. 315 (1): 47–53. DOI: 10.1016/j.jcis.2007.06.035.

Jong, T., Parry, D. L. (2005). Evaluation of the Stability of Arsenic Immobilized by Microbial Sulfate Reduction Using TCLP Extractions and Long-Term Leaching Techniques. *Chemosphere* vol. 60: 254–265. DOI: 10.1016/j.chemosphere.2004.12.046.

Karak, T., Abollino, O., Bhattacharyya, P., Das, K. K., Paul, R. K. (2011). Fractionation and Speciation of Arsenic in Three Tea Gardens Soil Profiles and Distribution of As in Different Parts of Tea Plant (Camellia Sinensis L.). *Chemosphere* vol. 85: 948–960. DOI: 10.1016/j.chemosphere.2011.06.061.

Kendall, M. R., Madden, A. S., Elwood Madden, M. E., Hu, Q. (2013). Effects of Arsenic Incorporation on Jarosite Dissolution Rates and Reaction Products. *Ceochim. Cosmochim. Acta* vol. 112: 192–207. DOI: 10.1016/j.gca.2013.02.019.

Ladeira, A. C. Q., Ciminelli, V. S. T., Nepomuceno, A. L. (2002). Seleção de solos para a imobilização de arsênio. *Rem: R. Esc. Minas* vol. 55 (3): 215-221. DOI: 10.1590/S0370-44672002000300009.

Ladeira, A. C. Q., Ciminelli, V. S. T. (2004). Adsorption and desorption of arsenic on na Oxisol and its constituents. *Water Res*. vol. 38 (8):; 2087-2094. DOI: 10.1016/j.watres.2004.02.002.

Larios, R., Fernández-Martínez, R., Rucandio, I. (2012a). Comparison of Three Sequential Extraction Procedures for Fractionation of Arsenic from Highly Polluted Mining Sediments. *Anal. Bioana. Chem*. vol. 402 (9): 2909–2921. DOI: 10.1007/s00216-012-5730-3.

Larios, R., Fernández-Martínez, R., Álvarez, R., Rucandio, I. (2012b). Arsenic Pollution and Fractionation in Sediments and Mine Waste Samples from Different Mine Sites. *Sci. Total Environ*. vol. 431: 426–435. DOI: 10.1016/j.scitotenv.2012.04.057.

Lv, W., He, W., Wang, X., Niu, Y., Cao, H., Dickerson, J.H., Wang., Z. (2014). Understanding the Oriented-Attachment Growth of Nanocrystals from an Energy Point of View: A Review. *Nanoscale* vol. 6: 2531–2547. DOI: 10.1039/c3nr04717b.

Masue, Y., Loeppert, R. H., Kramer, T.A. (2007). Arsenate and Arsenite Adsorption and Desorption Behavior on Coprecipitated Aluminum: Iron Hydroxides. *Environ. Sci. Technol*. vol. 41 (3): 837–842. DOI: 10.1021/es061160z.

Morin, G., Wang, Y., Ona-Nguema, G., Calas, G., Menguy, N., Aubry, E., Bargar, J. R., Brown, G. E. (2009). EXAFS and HRTEM Evidence for As(III)-Containing Surface Precipitates on Nanocrystalline Magnetite: Implications for As Sequestration. *Langmuir vol.* 25 (16): 9119–9128. DOI: 10.1021/la900655v.

Niederberger, M., Cölfen, H. (2006). Oriented Attachment and Mesocrystals: Non-Classical Crystallization Mechanisms Based on Nanoparticle Assembly. *Phys. Chem. Chem. Phys.* vol. 8 (28): 3271–3287. DOI: 10.1039/b604589h.

Ouvrard, S., Donato, Ph. de, Simonnot, M. O., Begin, S., Ghanbaja, J., Alnot, M., Duval, Y. B., Lhote, F., Barres, O., Sardin, M. (2005). Natural Manganese Oxide: Combined Analytical Approach for Solid Characterization and Arsenic Retention. *Ceochim. Cosmochim. Acta* vol. 69 (11): 2715–2724. DOI: 10.1016/j.gca.2004.12.023.

Pantuzzo, F. L., Ciminelli, V. S. T. (2010). Arsenic Association and Stability in Long-Term Disposed Arsenic Residues. *Water Res.* vol. 44 (19): 5631–5640. DOI: 10.1016/j.watres.2010.07.011.

Paktunc, D., Dutrizac, J., Gertsman, V. (2008). Synthesis and Phase Transformations Involving Scorodite, Ferric Arsenate and Arsenical Ferrihydrite: Implications for Arsenic Mobility. *Ceochim. Cosmochim. Acta* vol. 72 (11): 2649–2672. DOI: 10.1016/j.gca.2008.03.012.

Penn, R. L., Soltis, J. A. (2014). Characterizing Crystal Growth by Oriented aggregation. *Cryst. Eng. Comm.* vol. 16: 1409-1418. DOI: 10.1039/c3ce41773e.

Saitoh, K., Nakahara, H., Tanaka, N. (2013). Improvement of the Precision of Lattice Parameter Determination by Nano-Beam Electron Diffraction. *Microscopy* vol. 62 (5): 533–539. DOI: 10.1093/jmicro/dft023.

Schwertmann, U., Fittzpatrick, R. W., Taylor, R. M., Lewis, D. G. (1979). The Influence of Aluminum on Iron Oxides. Part Ii. Preparation and Properties of a1-Substituted Hematites. *Clays Clay Miner*. vol. 27 (2): 105–112.

Schwertmann, U., Friedl, J., Stanjek, H., and Schulze, D. G. (2000). The Effect of Al on Fe Oxides. XIX. Formation of Al-Substituted Hematite from Ferrihydrite at 25^oC and pH 4 to 7. *Clays Clay Miner*. vol. 48 (2): 159–172.

Schwertmann, U., Stanjek, H., Becher, H. H. (2004). Long-Term in Vitro Transformation of 2-Line Ferrihydrite to Goethite/hematite at 4, 10, 15 and 25^oC. *Clay Miner*. vol. 39: 433–438. DOI: 10.1180/0009855043940145.

Silva, G. C., Paula, J. A., Duarte, G., Ciminelli, V. S. T. (2013). Avaliação da estabilidade de rejeitos concentrados em sulfeto após 10 anos de disposição. In: XXV Encontro Nacional de Tratamento de Minérios e Metalurgia Extrativa & VIII Meeting of the Southern Hemisphere on Mineral Technology, Goiânia. Anais do XXV Encontro Nacional de Tratamento de Minérios e Metalurgia Extrativa. vol.3: 259-266.

Stadelmann, P. (1987). EMS - a Software Package for Electron Diffraction Analysis and HREM Image Simulation in Materials Science. *Ultramicroscopy* vol. 21 (2): 131–145. DOI: 10.1016/0304-3991(87)90080-5.

Taylor, R.M., Schwertmann, U. (1978). The Influence of Aluminum on Iron Oxides. Part I. The Influence of Al on Fe Oxide Formation from the Fe(II) System. *Clays Clay Miner*. vol. 26 (6): 373–383.

Violante, A., Del Gaudio, S., Pigna, M., Ricciardella, M., Banerjee, D. (2007). Coprecipitation of Arsenate with Metal Oxides. 2. Nature, Mineralogy, and Reactivity of Iron(III) Precipitates. *Environ. Sci. Technol.* vol. 41 (24): 8275–8280. DOI: 10.1021/es070382+.

Violante, A., Pigna, M., Del Gaudio, S., Cozzolino, V., Banerjee, D. (2009). Coprecipitation of Arsenate with Metal Oxides. 3. Nature, Mineralogy, and Reactivity of iron(III)-Aluminum Precipitates. *Environ. Sci. Technol.* vol. 43 (5): 1515–1521. DOI: 10.1021/es802229r.

Wang, Z., Xiao, D., Bush, R.T., Liu J. (2015). Coprecipitated arsenate inhibits thermal transformation of 2-line-ferrihydrite: Implications for long-term stability of ferrihydrite, *Chemosphere*¸ vol. 122: 83-93. DOI: 10.1016/j.chemosphere.2014.11.017.

Waychunas, G. A., Kim, C. S., Banfield, J. F. (2005). Nanoparticulate irion oxide minerals in soils and sediments: unique properties and contaminant scavenging mechanisms. J. Nanoparticle Res. vol. 7: 409-433. DOI: 0.1007/s11051-005-6931-x.

Williams, D. B.; Carter, C. B. (2009). *Transmission Electron Microscop.* Second Edition; New York, USA. Springer New York.

Xue, X., Penn, R. L., Leite, E. R., Huang, F., Lin, Z. (2014). Crystal Growth by Oriented Attachment: Kinetic Models and Control Factors. *Cryst. Eng. Comm.* vol. 16: 1419-1429. DOI: 10.1039/c3ce42129e.

Zhang, H., Banfield, J. F. (2012). Energy Calculations Predict Nanoparticle Attachment Orientations and Asymmetric Crystal Formation. *J. Phys. Chem. Lett*. vol. 3: 2882-2886. DOI: 10.1021/jz301161j.

CHAPTER 4. Arsenic entrapment by nanocrystals of Al-magnetite: the role of Al in crystal growth and As retention

Abstract

The nature of As-Al-Fe co-precipitates aged for 120 days are investigated in detail by high resolution transmission electron microscopy (HRTEM), scanning TEM (STEM), electron diffraction, energy dispersive x-ray spectroscopy (EDS), electron energy-loss spectroscopy (EELS), and energy-filtered transmission electron microscopy (EFTEM). The Al present in magnetite is shown to favour As incorporation (up to 1.10 wt%) relative to Al-free magnetite and Al-goethite, but As uptake by Al-magnetite decreases with increasing Al-for-Fe substitution (3.53 – 11.37% mol mol^{-1}). Arsenic-bearing magnetite and goethite mesocrystals (MCs) are formed by oriented aggregation (OA) of primary nanoparticles (NPs). Well-crystalline magnetite likely formed by Otswald ripening was predominant in the Al-free system. The As content in Al-goethite MCs (having approximately 13% substituted Al) was close to the EDS detection limit (0.1 wt% As), but was below detection in Al-goethites with 23.00 – 32.19 mol% Al. Our results show for the first time the capacity of Al-magnetite to incorporate more As than Al-free magnetite, and the role of Al in favouring OA-based crystal growth under the experimental conditions, and therefore As retention in the formed MCs. The proposed mechanism of As incorporation involves adsorption of As onto the newly formed NPs. Arsenic is then trapped in the MCs as they grow by self-assembly OA upon attachment of the NPs. We conclude that Al may diffuse to the crystal facets with high surface energy to reduce the total energy of the system during the attachment events, thus favouring the oriented aggregation.

Keywords: Arsenic immobilization, As partitioning, As speciation, Al magnetite

4.1. Introduction

The immobilization of As released by geogenic and anthropogenic sources is a major environmental concern due to the toxicity of this metalloid, which depends on the As species and their bioavailability in different matrices (Smith et al. 1998, 2008; Smedley and Kinniburgh 2002). Recent studies have investigated the processes of immobilization of this metalloid in iron and/or aluminium (hydr)oxides (Ladeira and Ciminelli 2004; Ona-Nguema et al. 2005, 2010; Violante et a. 2006, 2007; Morin et al. 2008, 2009; Duarte et al. 2012; Bolanz et al. 2013; Guo et al. 2013; Das et al. 2014; Doerfelf et a. 2015) or in mixed Al-Fe-(hydr)oxides (Masue et al. 2007; Violante et al. 2009; Silva et al. 2010; Adra et al. 2013, 2016; Freitas et al. 2015). Mixed Al-Fe-(hydr)oxides have been identified as successful candidates for the long-term As immobilization due to the effects of Al-for-Fe substitution in these phases. Aluminium-bearing Fe-(hydr)oxides are ubiquitous in soils and acid mine drainage (AMD) water, and are also known to favour stable alpha- over gamma-phases (Taylor and Schwertmann 1978). Up to a certain concentration, Al gives more stability to Al- substituted Fe-(hydr)oxides such as ferrihydrite, goethite, hematite, and magnetite (Cornell and Schwertmann 2003), slowing down further phase transformation. The properties of mixed Al-Fe-(hydr)oxides have been explored in recent investigations on As immobilization and in water treatment. In a study of co-precipitation of As, Al and Fe from Fe and Al nitrates at 20 ºC, with initial Fe:Al molar ratio of 1, Violante et al. (2009) reported that As(V) is mainly incorporated in short-range ordered precipitates such as ferrihydrite, whose transformation is retarded due to the presence of Al. The decrease in As(V) concentration at the surface of co-precipitated products is followed by an increase in pH and ageing (Violante et al. 2009), which the authors attributed to a decrease of the solids' surface area as they evolved to a more ordered structure. Investigations on As adsorption onto Al-substituted goethite were undertaken by Silva et al. (2010). The results showed the high loading capacity of Al-goethite with respect to As(V) relative to pure goethite and hematite. Masue et al. (2007) and Adra et al. (2016) carried out similar investigations on As sorption onto Al-substituted ferrihydrite. Both groups reported a decreasing sorption of As(III) with increasing Al:Fe molar ratio (up to 20% mol mol^{-1}) in Al-containing ferrihydrite at nearly neutral pH. However, Masue et al.

(2007) observed no change in the adsorption of As(V) on Al-substituted ferrihydrite for increasing Al:Fe molar ratios, whilst Adra et al. (2016) reported an increase in As(V) adsorption. More recently, magnetite sorbents have become a topic of much interest due to their various applications, such as the removal of trace contaminants from aqueous systems. Despite these recent advances, there is relatively little information on As-bearing Al-magnetite compared to other iron oxides. Al-free magnetite NPs have been shown to have high As adsorption capacity (Morin et al. 2009; Ona-Nguema et al. 2010; Akin et al. 2012; Farrell et al. 2014; Türk and Alp 2014; Liu et al. 2015) and are commonly used for the treatment of polluted water. Al-bearing magnetite-based materials have been proposed as new types of adsorbents for As removal from contaminated water (Zhang et al. 2012; Moradlou et al. 2016). In general, the increased loading capacity onto mixed Al- and Fe- (hydr)oxides has been ascribed to increased surface area due to the presence of Al (Silva et al. 2010). The effect of increasing amounts of Al over As sorption, however, is still debated. Arsenic adsorbed onto metal (hydr)oxide nanoparticles (NPs) can be incorporated into the crystal structure as these phases evolve to more ordered phases, as shown by ageing As-bearing ferrihydrite (Violante et al. 2007; Bolanz et al. 2013; Das et al. 2014), and As-bearing Al-substituted ferrihydrite (Violante et al. 2009). Nevertheless, very few studies have investigated the mechanisms of structural As incorporation in Fe-(hydr)oxides. The pioneering work of Waychunas et al. (2005) suggested that oriented aggregation (OA)-based crystal growth could play a major role in metal contaminant scavenging from polluted waters. Nevertheless, to the authors' knowledge there is no experimental evidence in the scientific literature showing the role of OA-based crystal growth on the mechanism of As fixation in Al-containing Fe-(hydr)oxides. In our previous work (Freitas et al. 2015) we proposed that As immobilization in tailings impoundments in a gold mine occurred mainly by the incorporation of As(V) in natural nanostructured Al-hematite upon OA of primarily As-adsorbed Al-ferrihydrite NPs, which ultimately formed Al-hematite by ageing. However, the role of Al in the process of As immobilization in such mixed phases is yet to be fully understood.

In this study, As-bearing synthetic As-Al-Fe co-precipitates aged for 120 days were investigated using high resolution transmission electron microscopy (HRTEM), scanning TEM (STEM), selected area electron diffraction (SAD), energy dispersive X-ray spectroscopy (EDS), electron energy-loss spectroscopy (EELS), and energy-filtered transmission electron microscopy (EFTEM). The aim of this investigation was to understand (1) the nature of As-bearing phases; (2) the role of Al in the formation of these As-bearing phases; and (3) the mechanisms of As incorporation in magnetite. The effects of Al on As incorporation in co-precipitated Al-magnetite are shown here for the first time. Our results provide evidence for As scavenging by Al-magnetite whose magnetic properties can be utilized for its recovery from treated water.

4.2. Materials and Methods

For the purpose of this study synthetic samples were prepared according to a modified version (Silva et al. 2010) of the procedure described by Schwertmann and Cornell (2000). Synthetic As-bearing Al-Fe-(hydr)oxides were prepared by co-precipitating Fe, Al, and As, from ferrous and Al sulphates in the presence and absence of As, under E_h of approx. - 400 mV, pH 11.7 and ambient temperature (Mello et al. 2017), using three different initial Fe:Al molar ratios (R = 1:0, 1:0.3, and 1:0.7) and different As concentrations in the initial solution (C = 1 and 5 mg L^{-1}). The co-precipitated samples are hereafter named following the notation FeAl(R)CAs (e.g., FeAl(1:0.7)1As). Sulphate salts were used to represent water conditions in gold base metal mining environments and processing. The co-precipitated phases with different concentrations of Al were investigated as Al-Fe-(hydr)oxides are ubiquitous in many types of tropical and sub-tropical soils. The samples were aged for 120 days in plastic bottles at room temperature (around 25 °C). The bottles were opened daily and suspension stirred during five minute to allow slow oxidation of Fe^{2+} to Fe^{3+} and incorporation of Al^{3+}. The pH was kept > 11 over the time by adding KOH when needed. After the aging time, the suspensions were removed and precipitates freezed dried.

4.2.1. Sample preparation

Suspension of each sample was achieved by dispersion in distilled water in Eppendorf® tubes, and by sonication in an ultrasound bath for three minutes. Before sample loading, the carbon-coated TEM Cu-support grids (300 mesh) were subjected to a glow discharge process (Bal-Tec Sputter MD20) for approximately 15 seconds (Ayache et al. 2010). A drop of particle suspension was placed on the surface of a Petri dish filled with distilled water to form a thin film of fine particles on the water surface, and then the carbon film side of the TEM grid was placed in contact with the fine particles spread on the water surface to pick up the solids.

4.2.2. Electron microscopy techniques

The samples were analysed using HRTEM, SAD, EDS, EELS, and EFTEM in the Center of Microscopy at the Universidade Federal de Minas Gerais (CM-UFMG), Brazil, using a LaB_6-TEM Tecnai G^2 20 SuperTWIN (FEI), at 200 kV, and in the Centre for Microscopy and Microanalysis at The University of Queensland, Australia, using a FEG-STEM Phillips Tecnai F20, at 200kV. The EELS spectra were performed with energy resolution of 1.2 eV and energy dispersion of 0.3 eV/channel. The EFTEM was performed by using the three-window method.

4.3. Results and discussion

Our previous study (Freitas et al. 2015) demonstrated for the first time As fixation in Al-bearing hematite NPs in natural soils through oriented attachment. Here, we further investigate the mechanism of As entrapment in other iron oxides, formed under laboratory conditions, in the presence and absence of Al.

4.3.1. Phase formation and crystal morphology in the presence of Al and As

X-ray diffraction analyses (Figure 4.1) of the precipitates showed only goethite and minor bayerite in the series of experiments with high Al. Magnetite and goethite were formed in the experiments performed with intermediate amount of Al, and only magnetite was formed in the absence of Al. These results were confirmed by TEM analyses (the presence of bayerite, however, was not verified).

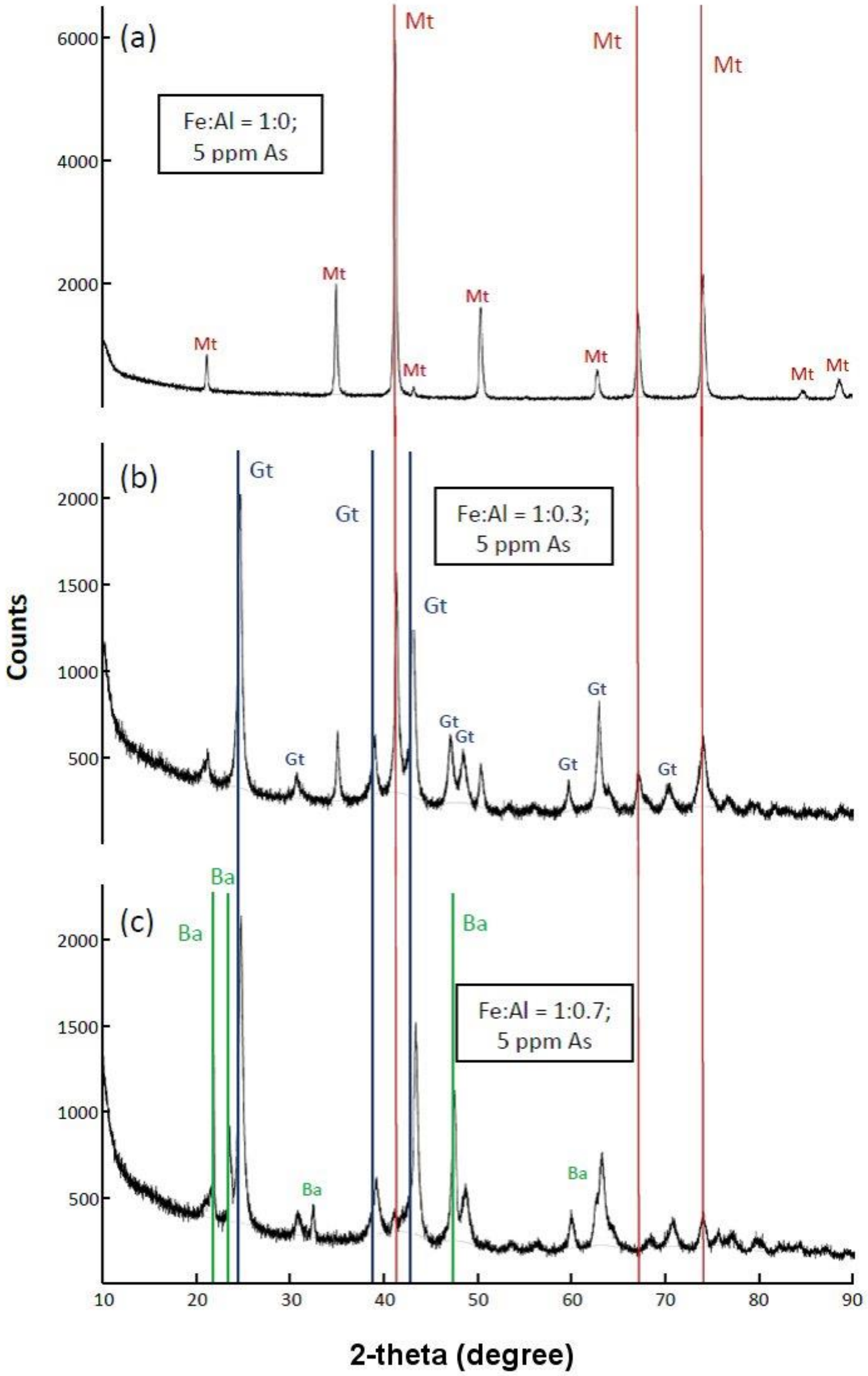

Figure 4.1. X-ray diffractograms of synthetic samples with 5 ppm As and (a) Fe:Al = 1:0 (magnetite only); (b) Fe:Al = 1:0.3 (goethite and magnetite), and (c) Fe:Al = 1:0.7 (goethite and bayerite with traces of magnetite). Mt – magnetite; Gt – goethite; Ba – bayerite. The three strongest lines for each “pure” mineral have been marked with continuous lines. Note the slight shift in the goethite spectra relative to “pure” goethite, and attributed to the presence of Al in the goethite structure.

The only Fe-(hydr)oxide phase identified by TEM in the samples co-precipitated with high amounts of Al (FeAl(1:0.7)1As and FeAl(1:0.7)5As) was Al-goethite (Figure 4.2). The calculated Al/(Al+Fe) ratio based on EDS analysis ranged from 29.05 – 32.22 mol%. No Al-(hydr)oxide was identified. The samples co-precipitated with intermediate amount of Al (FeAl(1:0.3)1As and FeAl(1:0.3)5As) showed Al-goethite followed by Al-magnetite. Schwertmann and Murad (1990) ascribed the predominance of goethite over magnetite at high Al concentrations to the capacity of the goethite structure to accommodate more Al.

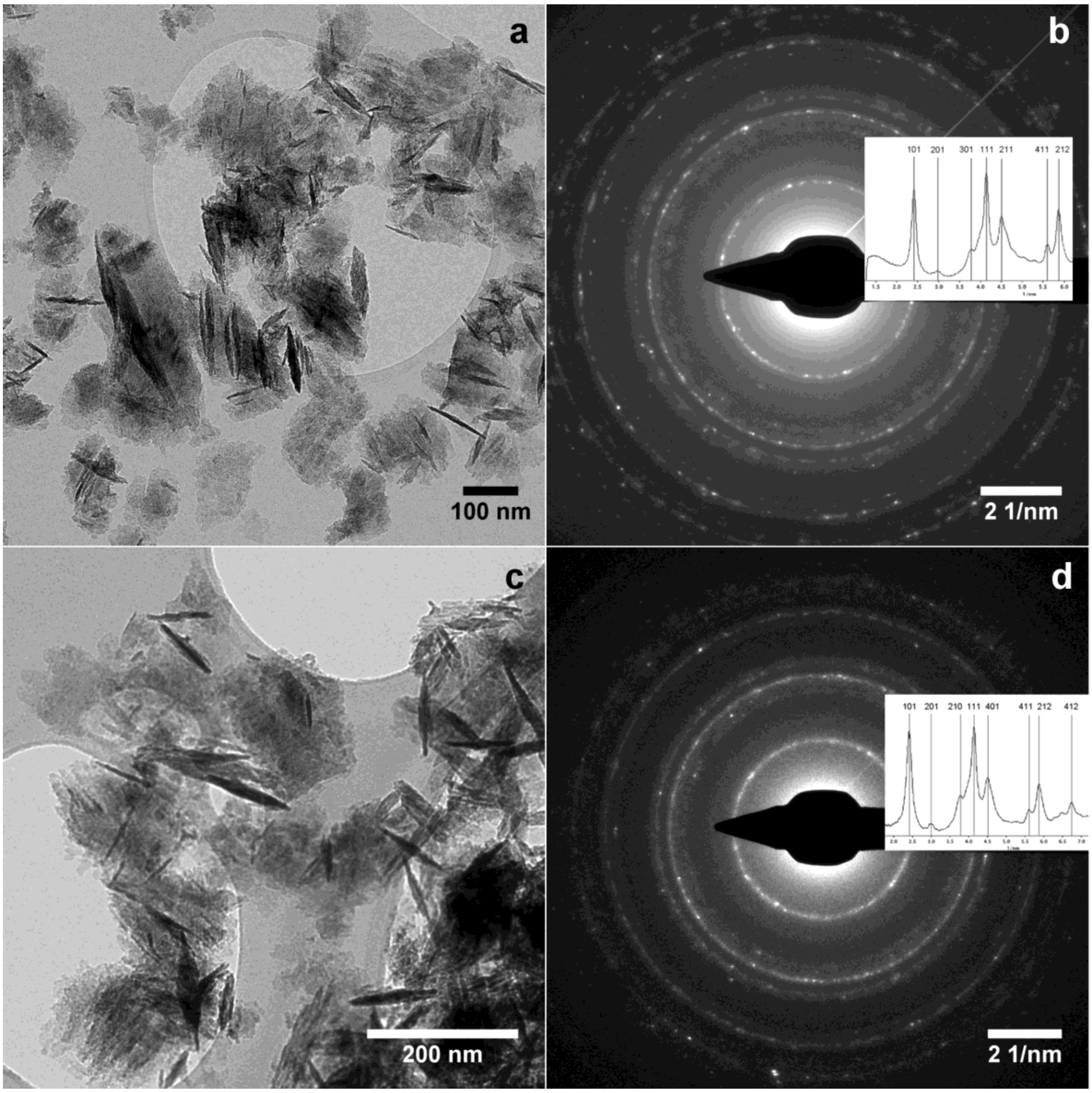

Figure 4.2. Typical bright field TEM images and the SAD pattern of samples (a-b) FeAl(1:0.7)1As, and (c-d) FeAl(1:0.7)5As. The insets in images (b) and (d) are the line profiles of the indexed SAD patterns displaying the *hlk* for goethite.

Figure 4.3 shows typical TEM images of Al-magnetite and Al-goethite crystals found in sample FeAl(1:0.3)5As. The Al-magnetite appears as plate-shape crystals of about 100 nm (Figure 4.3.a – particle 1). The Al-goethite crystals are flat and acicular and range in size from 50 to 150 nm (Figure 4.3.a – particle 2). The Al-goethite crystals show striations along a particular direction, similar to those described by Schwertmann and Murad (1990).

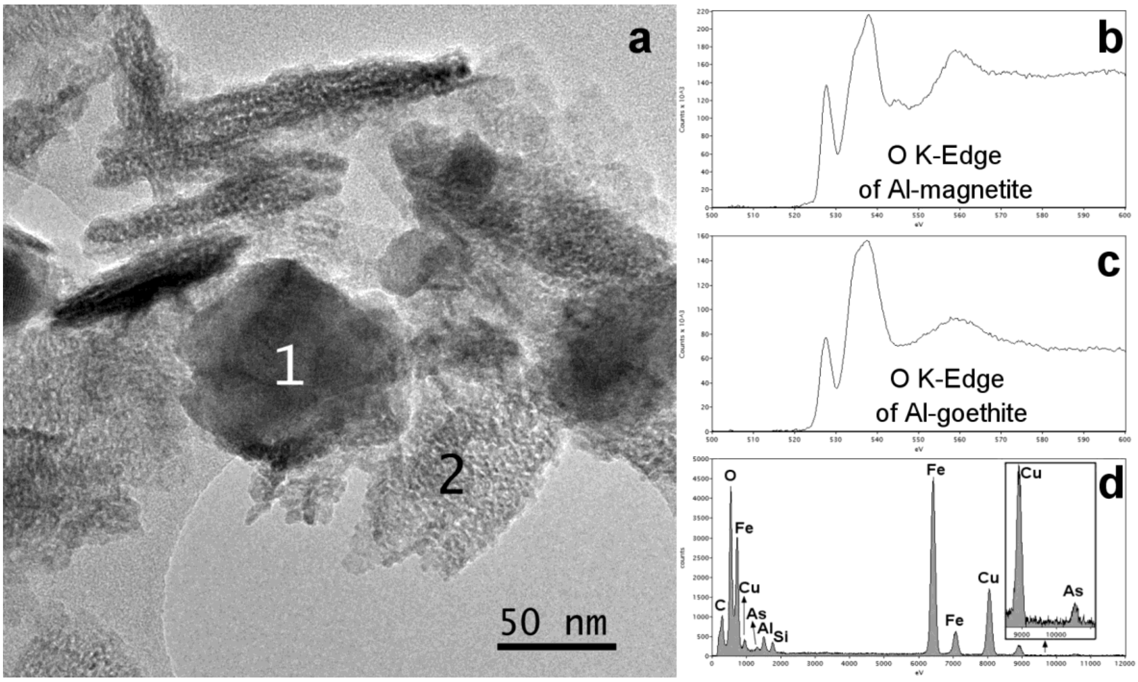

Figure 4.3. (a) Bright Field TEM image of sample FeAl(1:0.3)5As showing plate-shape crystalline Al-magnetite (particle 1) and plate and acicular “grainy” Al-goethite (particle 2). (b-c) Spectra of O K-near edge structure performed in particles 1 and 2, respectively, shown in (a). (d) EDS spectrum performed in Al-magnetite (particle 1).

The spectra of energy-loss near edge structure (ELNES) for Al-magnetite and Al-goethite in sample FeAl(1:0.3)5As are shown in Figure 4.3.b-c. The electron energy-loss spectrum arises from the electron-beam (primary electrons) that loses energy due to the beam-specimen interaction. The primary electrons scattered by ionized atoms’ core-shell of the specimen lose characteristic energies that can be used for elemental identification. The ELNES is due to the scattering by the first coordination shell around ionized atom and can be used for phase identification (Colliex et al. 1991; Williams and Carter 2009). The Al-magnetite was identified by comparing the experimental ELNES spectrum with the available spectrum in the literature (Colliex et al. 1991; Gloter et al. 2003). Al-goethite was confirmed by comparing its ELNES spectra to the reference goethite (Figure 4.4). The Al/(Al+Fe) molar ratio ranged from 3.03 – 11.37% mol mol^{-1} for Al-magnetite and 12.08 – 25.81% mol mol^{-1} for Al-goethite, consistent with the range reported in the literature (Schwertmann and Murad 1990; Cornell and Schwertmann 2003). Arsenic (0.90 wt%) was detected in Al-magnetite (Figure 4.3.d). The As content in Al-goethite was below the EDS detection limit (0.1 wt%) in the highest Al-containing goethites and close to detection limit (DL) in the Al-poor Al-goethites (< 13 mol mol^{-1}% Al). The detection limit was estimated based on the statistical criteria for minimum mass fraction (Williams and Carter 2009). These results suggest that As is preferably incorporated into Al-magnetite, but the reason for the lower uptake by the Al-goethite co-precipitates was not further investigated in this study and remains to be explained.

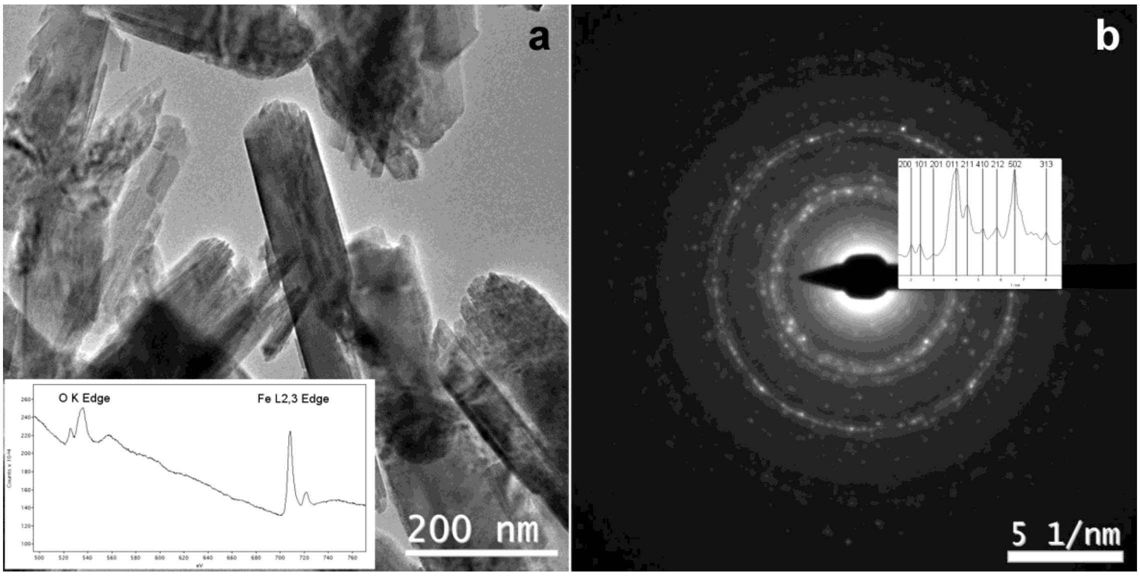

Figure 4.4. (a) TEM image of reference goethite; (b) SAD pattern of goethite. The inset in (a) shows the O K-edge and Fe $L_{2,3}$-edges in the EELS spectra of goethite with non-removed background. The inset in (b) shows the indexed line profile of the SAD pattern of goethite.

The EDS maps show the distribution of O, Fe, Al and As in Al-magnetite crystals measured in sample FeAl(1:0.3)5As (Figures 4.5.e-h). Aluminium is homogenously distributed in the crystal. The Al/(Al+Fe) molar ratios in the Al-magnetites shown in Figure 4.3.a was 9.25% mol mol^{-1}. The As content in Al-magnetite in this sample is higher than in the coexisting Al-goethite, which was shown to be below detection limit (< 0.1 wt% As). This trend was observed regardless of the initial As concentration in the solution.

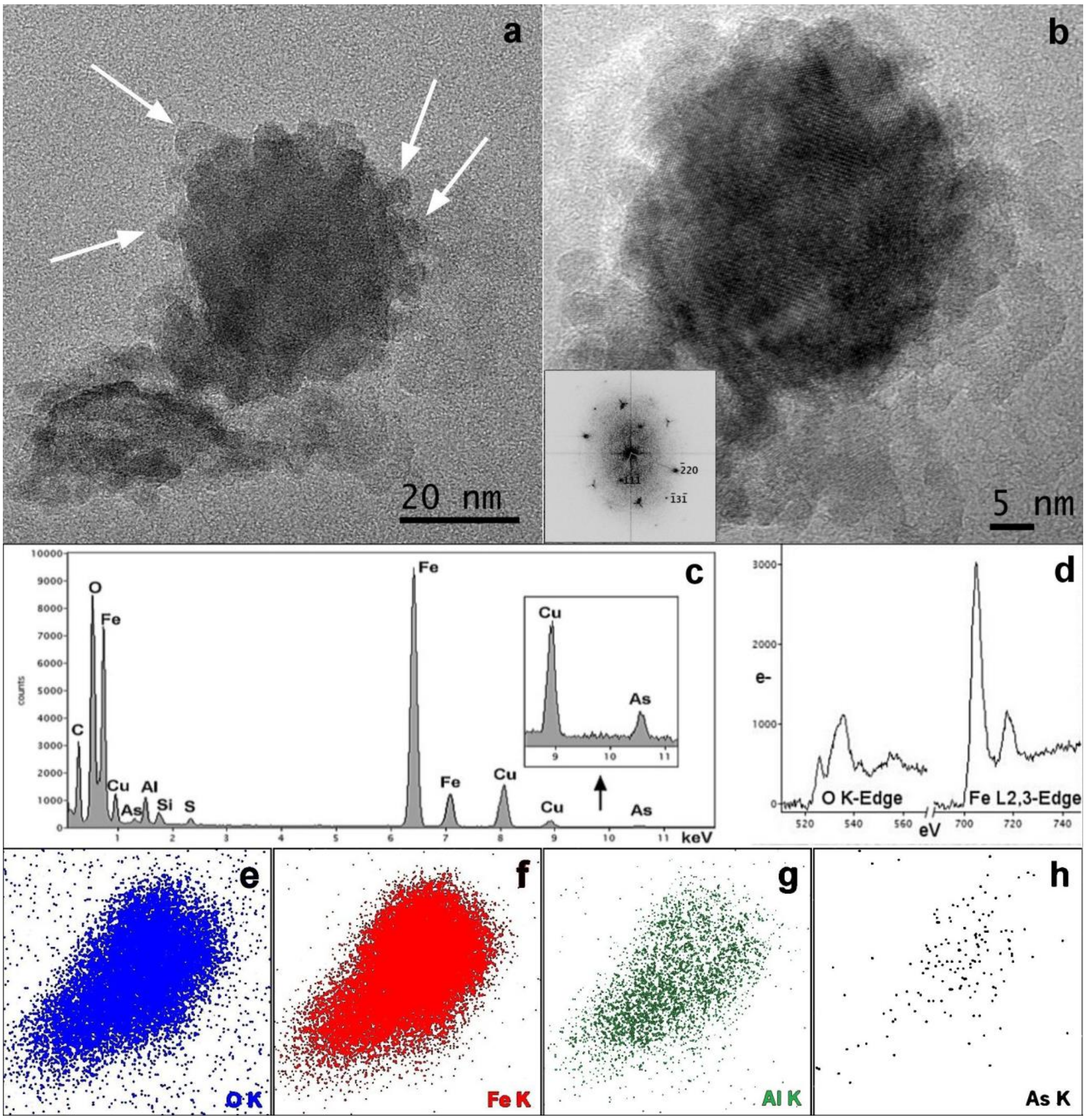

Figure 4.5. (a-b) TEM and HRTEM images of an aggregate of Al-magnetite NPs in sample FeAl(1:0.3)5As. The arrows indicate some of the attached NPs. The crystal shown in (b) is tilted along the [112] ZA. The inset shows the FFT of the whole HRTEM image (b). (c-d) EDS and ELNES spectra of Al-magnetite performed in the aggregate shown in (a). (e-h) STEM-EDS maps of the aggregate shown in (a).

4.3.2. Role of Al (and As) in crystal growth by oriented aggregation

The predominance of mesocrystals (MCs) of As-bearing Al-Fe-(hydr)oxide phases was demonstrated by HRTEM. The MCs are formed by oriented aggregation of nanoparticles (Niederberger and Cölfen 2006). Although the morphology by itself is not sufficient evidence to confirm the mechanism of crystal growth (Penn and Soltis 2014; De Yoreo et al. 2015), our results show common features of OA (Figures 4.5 and 4.6),

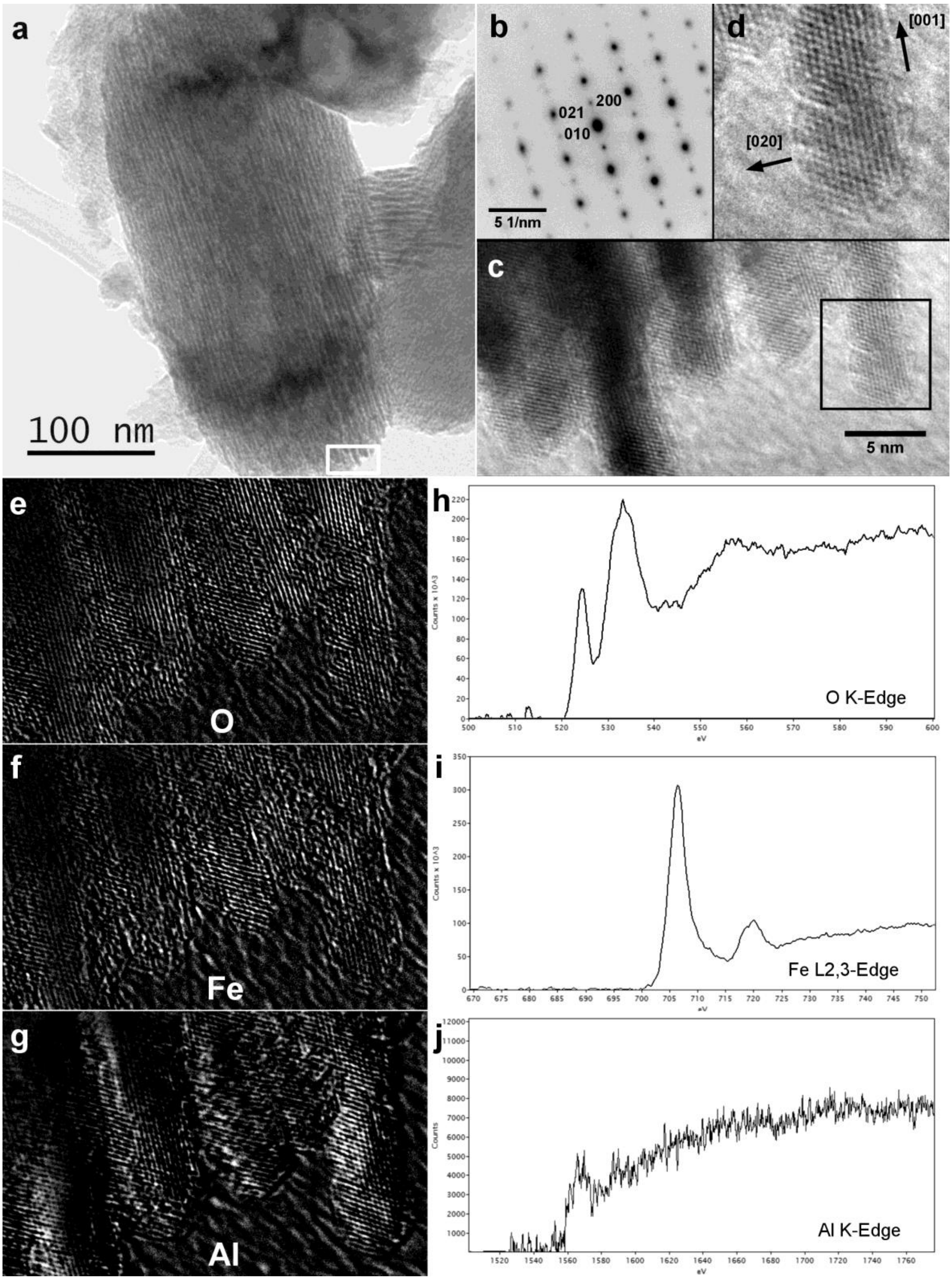

Figure 4.6. (a) TEM image of the Al-goethite in sample FeAl(1:0.3)1As. (b) SAD pattern taken from the whole crystal shown in (a). (c) HRTEM image of the bottom part of the Al-goethite crystal in (a). (d) Magnified image of the area inside the square in (c). (e-g) EFTEM showing the elemental mapping of O, Fe, and Al in the small square in (a), performed from the corresponding EELS spectra shown in (h-j). The brighter areas in (e-g) are those with elevated concentrations of mapped elements.

suggesting this was the mechanism of crystal growth during co-precipitation of Fe, Al, and As, and ageing. Mesocrystals of Al-magnetite and Al-goethite are shown in Figures 4.5 and 4.6, respectively. Phases were confirmed by EELS, HRTEM and SAD. The OA of Al-magnetite NPs is clearly observed in Figures 4.5.a-b. The Fast Fourier Transform (FFT) in the inset in Figure 4.5.b evidences the good attachment of NPs. Figure 4.6 shows an Al-goethite MC illustrating a perfect attachment of goethite NPs and the distinct morphology and a column-like texture (Figure 4.6.a). The perfect attachment is confirmed by the SAD (Figure 4.6.b), which is similar to the scattering from a single crystal, indicating the well-aligned assembly of NPs. Two attached NPs are shown in detail along the [001] direction (Figure 4.6.d). The attachment likely took place in {210} faces, which is in line with the most favoured predicted OA faces in the attachment event of 4 nm compounds of goethite (Zhang and Banfield 2012).

Our results suggest that Al plays a role in the OA of newly-formed goethite NPs. The EFTEM results show the elemental mapping for O, Fe, and Al performed in each corresponding ionization shell (Figure 4.6.e-j). Aluminium is not homogenously dispersed in the crystal structure, but mostly concentrated in the {020} faces (Figure 4.6.g). The presence of Al at these faces seems to have induced the crystal growth perpendicular to the [001] direction, by decreasing the surface energy of {020} and {210} thus favouring the attachment of NPs along these faces. The HRTEM and SAD data show that each column of NPs shares faces parallel to {020}, which suggests that attachment events also occurred in these faces, though {020} may not be favoured in attachment events for goethite compounds (Zhang et al. 2012). The reduction of total energy of the system upon attachment at the {020} faces is low when compared to the most favoured OA faces for goethite compounds. In order to explain this, we propose that Al may diffuse to the faces of high surface energy to reduce the total energy of the system during attachment events, thus favouring the oriented aggregation of the goethite NPs also in directions perpendicular to [001].

Aluminium may hinder the growth of the newly-formed Al-goethite NPs, so that the NPs grow to a suitable size that favours oriented aggregation (Zhang et al. 2012). The attraction of substituted Al to O from FeO_6 octahedra makes the Fe-O bond weaker

(Schwertmann et al. 1979; Schertmann and Murad 1990), and therefore substituted Al may hamper further growth of newly formed NPs. The short size range of the newly-formed NPs in solution might have kept the system in the OA-based crystal growth regime. In contrast, for the samples co-precipitated without Al the dominant crystal growth mechanism was likely Ostwald ripening (OR), whereby larger and more energetic stable particles grow at the expense of the smaller ones. The crystals grown by OR normally result in particles that keep the morphology consistent to the crystal symmetry (Xue et al. 2014). This pattern was observed for samples co-precipitated without Al (Figure 4.7.a and Figure 4.8). Octahedral magnetite was the only phase found in samples FeAl(1:0)1As and FeAl(1:0)5As. In these samples, crystal sizes (from 50 to 300 nm) were larger compared to the samples co-precipitated with Al.

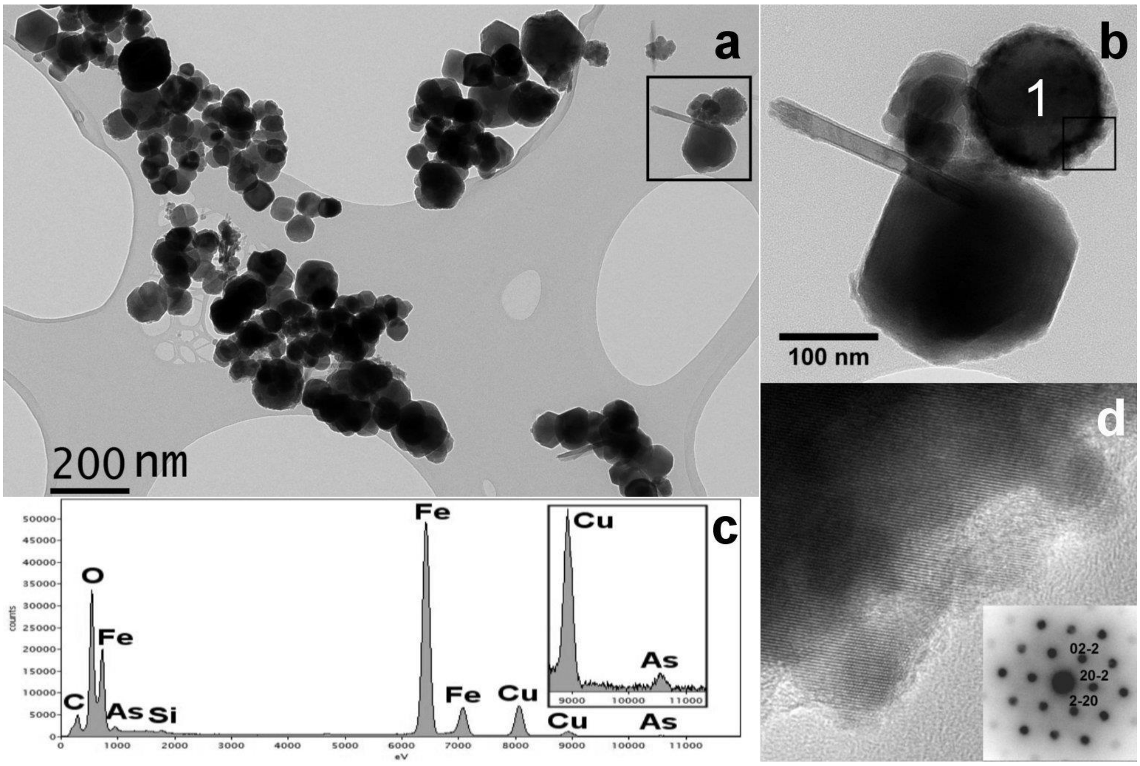

Figure 4.7. (a) TEM image of nanocrystals of magnetite in sample FeAl(1:0)5As. (b) magnified image of the area inside the square in (a). (c) EDS spectrum of the oriented aggregate of nanoparticles – particle 1 in (b). (d) HRTEM image of the area inside the square in (b) showing the OA of magnetite NPs. The inset in (d) shows the nano-beam electron diffraction pattern of the OA of NPs indexed as the zone axis <111> of magnetite.

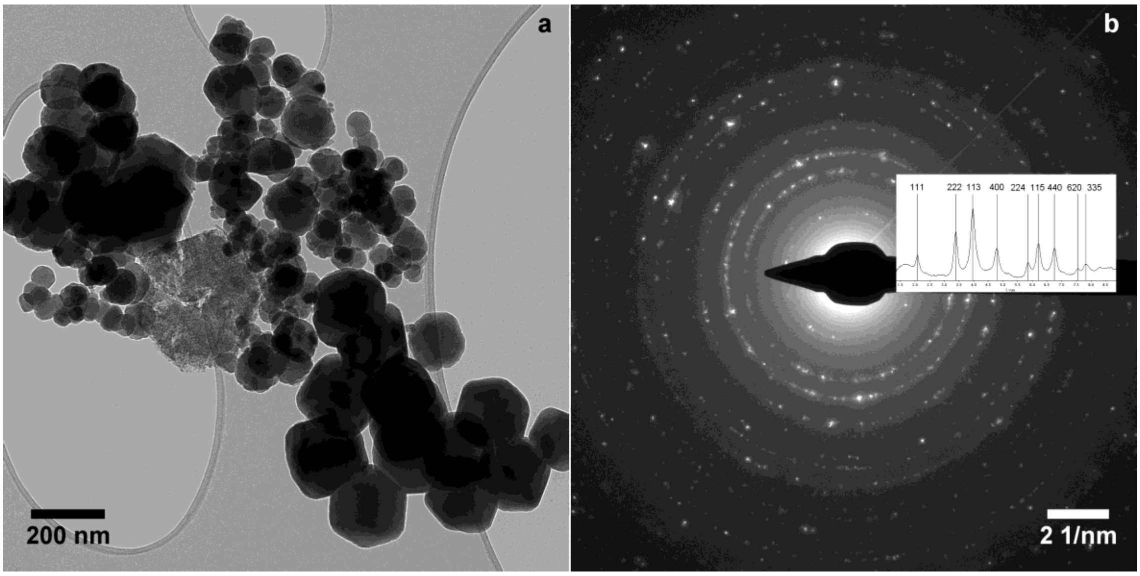

Figure 4.8. (a) TEM image of magnetite crystals of sample FeAl(1:0)1As; (b) SAD pattern of magnetite. The inset in (b) shows the indexed line profile of SAD pattern of magnetite.

Arsenic may also favour oriented aggregation. In the absence of Al, 0.30 wt% As was detected by EDS in an oriented aggregate of magnetite NPs in sample FeAl(1:0)5As (Figure 4.7.b-d). Like for Al, the adsorption of As (at low As/Fe molar ratio) onto some newly-formed magnetite NPs may energetically favour the oriented attachment events. Even though minor OA of magnetite had been observed in sample FeAl(1:0)5As, the amount of As detected in the aggregate (about 300 mg kg^{-1}) is up to 100 times the amount of As measured in the well-crystalline magnetite particles. The hypothesis proposed by Xue et al. (2014) whereby As anions in solution act as capping ligands favouring a mixed OA-OR growth may explain the coexistence of OA magnetite with well-crystallised magnetite in Al-free solutions.

4.3.3. Role of Al in the incorporation of As in magnetite

The amount of substituted Al in the crystalline Al-Fe-(hydr)oxide phases together with the dominant mechanism of crystal growth seem to control the amount of As incorporated in the MCs. Figure 4.9 shows the variation in As (wt%) content as a function of Al/(Al+Fe) molar ratios calculated from the EDS data in the OA of magnetites co-precipitated with 5 mg L^{-1} As in the initial solution. The maximum As content (1.10 wt% As) was observed at 3-5% mol mol^{-1} of substituted Al, and decreased to 0.43 wt% for an Al/(Al+Fe) molar ratio of 11.37% mol mol^{-1}. The As content in magnetite thus decreases linearly with increasing substituted Al, likely due to the increase of Fe^{2+} sites relatively to F^{3+} substituted by Al^{+3} in the tetrahedral sites. (Schwertmann and Murad 1990). This might contributed to weaken the interaction between arsenic anions and iron at lower Al substitution. Moreover, As uptake by OA of Al-magnetite was higher than in the Al-free magnetite (0.30 wt% As). Arsenic was below DL in single crystals of magnetite co-precipitated without Al. The EDS analysis of OA in Al-goethite showed that As was ≤0.1 wt% in Al-goethite with 13% mol mol^{-1} Al or higher.

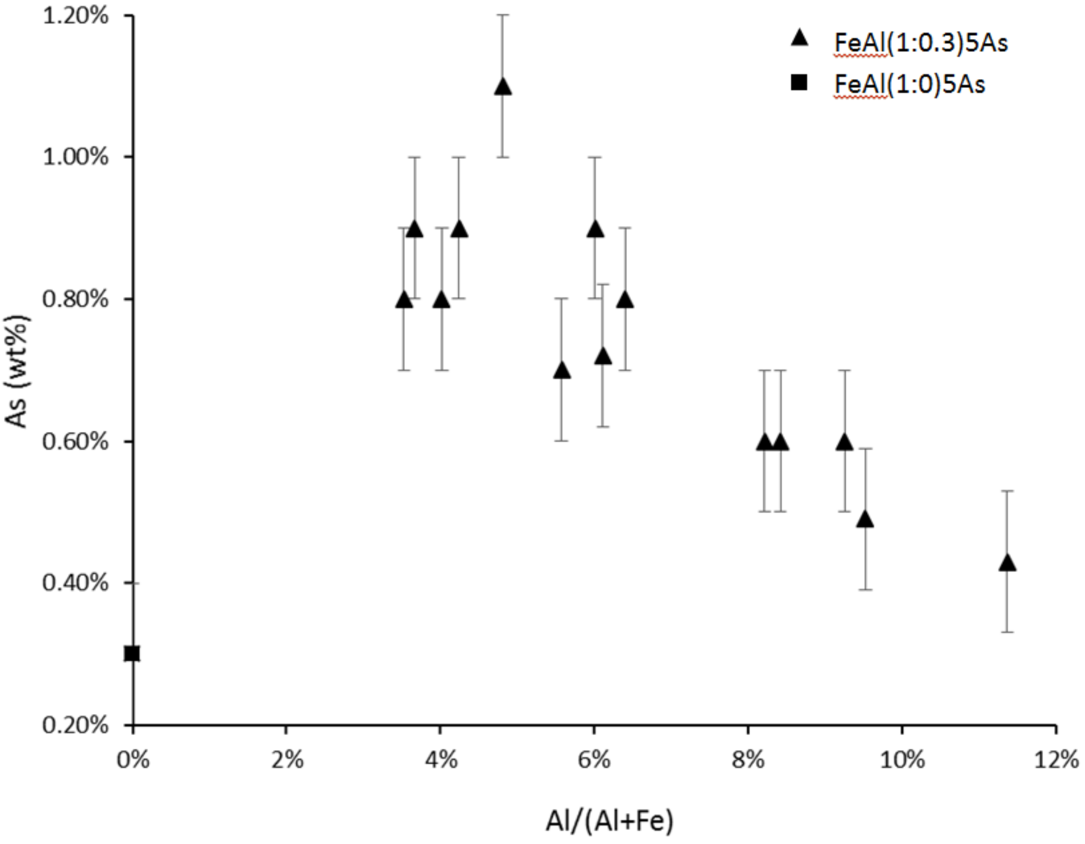

Figure 4.9. As (wt%) and Al/(Al+Fe) molar ratio (% mol mol^{-1}) in OA of magnetite nanoparticles. The deviation in As content (σ = 0.1 wt%) was considered as the error given by the EDS software.

The Al-for-Fe substitution in the magnetite induces structural strain (Schwertmann and Murad 1990), which can favour sequestration of contaminants. This process is consistent with our data, which show larger amounts of As (up to 1.10 wt%) in the OA of Al-magnetite than in the OA of magnetite without Al (0.30 wt% As). Arsenic adsorption can take place to reduce surface strain (Waychunas et al. 2005) caused by structural Al. On the other hand, Al can also favour the aggregation-based crystal growth, which may enhance the incorporation of As by trapping it upon attachment of NPs, as discussed in sub-section 4.3.2.

The mechanism of magnetite formation in the presence of Al may follow the sequence described for Al-free solutions. Magnetite particles may nucleate at the surface of Fe(III)-oxides upon reaction with Fe^{2+} as proposed by Tamaura and Katsura (1981). Alternatively, magnetite NPs may precipitate and aggregate upon adhesion on the surface of platy crystals of $Fe(OH)_2$ and then recrystallize to form larger and more crystalline particles (Sugimoto and Matijević 1980), in agreement with OA-based crystal growth (Yuwono et al. 2010; Penn and Soltis 2014; De Yoreo et al. 2015). Magnetite MCs have been shown to nucleate and grow *via* self-assembly oriented attachment in alkaline conditions and 25 ^{o}C by interaction between Fe^{2+} and ferrihydrite hydrogel (Baumgartner et al. 2013). In our study, we propose that As primarily adsorbed on the NPs is trapped in the aggregates as they grow and finally irreversibly incorporated upon attachment events to form larger particles of magnetite. The formation of (Al-containing) green rust/ferrihydrite as intermediate phases in our study is not excluded, as ferrihydrite may favour the nucleation of magnetite (Baumgartner et al. 2013), and also catalyses the oxidation of adsorbed Fe^{2+} (Cornell and Schwertmann 2003).

4.4. Environmental implications

The proposed oriented attachment mechanisms for As immobilization in Al-bearing Fe(hydr)oxide phases formed under experimental conditions account for As scavenging from polluted waters. Aluminium can play a major role in increasing As uptake by the Al-containing Fe-(hydr)oxides as these nucleate and grow by self-assembly aggregation as shown in this work. The magnetic properties of Al-magnetite with relatively high As content can be explored in the subsequent separation of the solid As-bearing phase (magnetite) from the treated waters. The phases remained stable after 120 days of ageing at ambient conditions, with no evidence of phase change. The presence of aluminium thus increases the long-term stability of the As-bearing precipitates by slowing down or even preventing further phase transformation.

4.5. Conclusion

The findings from the analysis of synthetic Al-Fe-(hydr)oxides precipitated in the presence of As showed for the first time that (a) As entrapment in Al-magnetite mesocrystals reaches a maximum between 3 and 5% mol mol^{-1} of substituted Al and then decreases linearly with increasing Al substitution; (b) larger amounts of As are incorporated in Al-magnetite compared with Al-free magnetite and other co-precipitated products; (c) the presence of Al favours the oriented attachment-based crystal growth, and therefore larger amount of As is immobilised as the magnetite crystals are formed; and (d) the mechanism of As fixation in the mesocrystals involves As-adsorption onto primary nanoparticles, followed by As entrapment upon oriented attachment of nanoparticles.

4.6. References

Adra, A., Morin, G., Ona-Nguema, G., Brest, J. (2016). Arsenate and arsenite adsorption onto Al-containing ferrihydrites. Implications for arsenic immobilization after neutralization of acid mine drainage. *Appl. Geochem.* vol. 64: 2-9. DOI: 10.1016/j.apgeochem.2015.09.015.

Adra, A., Morin, G., Ona-Nguema, G., Menguy, N. Maillot, F. Casiot, C. Bruneel, O., Lebrun, S., Juillot, F., Brest, J. (2013). Arsenic Scavenging by Aluminum-Substituted Ferrihydrites in a Circumneutral pH River Impacted by Acid Mine Drainage. *Environ. Sci. Technol*. vol. 47 (22): 12784–12792. DOI: 10.1021/es4020234.

Akin, I., Arslan, G., Tor, A., Ersoz, M., Cengeloglu, Y., (2012). Arsenic(V) removal from groundwater water by magnetic nanoparticles synthesized from wast red mud. *J.Harzard. Mater.* vol. 235-236: 62-68. DOI: 10.1016/j.hazmat.2012.06.024.

Ayache, J., Beaunier, L., Boumendil, J., Ehret, G., Laub, D. (2010). *Sample Preparation Handbook for Transmission Electron Microscopy*. New York, USA. Springer.

Baumgartner, J., Dey, A., Bomans, P. H. H., Le Coadou, C., Fratzl, P., Sommerdijk, N. A. J. M., Faivre, D. (2013). Nucleation and growth of magnetite from solution. *Nat. Mater.* vol. 12 (4): 310–314. DOI: 10.1038/nmat3558.

Bolanz, R. M., Wierzbicka-Wieczorek, M., Čaplovičová, M., Uhlík, P., Göttlicher, J., Steininger, R., Majzlan, J. (2013). Structural incorporation of As5+ into hematite. *Environ. Sci. Technol,* vol. 47 (16): 9140–9147. DOI: 10.1021/es305182c.

Colliex, C., Manoubi, T., Ortiz, C. (1991). Electron-energy-loss-spectroscopy near-edge fine structures in the iron-oxygen system. *Phys. Rev. B*. vol. 44 (20): 11402–11411.

Cornell, R.M.; Schwertmann, U. (2003). *The Iron Oxides: Structure, Properties, Reactions, Occurrences and Uses.* Second Edition. Weinheim, Germany. Wiley-VHC.

De Yoreo, J. J., Gilbert, P. U. P. A., Sommerdijk, N. A. J. M., Penn, R. L., Whitelam, S., Joester, D., Zhang, H., Rimer, J. D., Navrotsky, A., Banfield, J. F., Wallace, A. F., Michel, F. M., Meldrum, F. C., Colfen, H., Dove, P. M. (2015). Crystallization by particle attachment in synthetic, biogenic, and geologic environments. *Science* vol. 349 (aaa6247), 1–9. DOI: 10.1126/science.aaa6760.

Das, S., Essilfie-Dughan, J., Hendry, M. J. (2014) Arsenate partitioning from ferrihydrite to hematite: spectroscopic evidence. *Am. Mineral.* vol. 99: 749-754. DOI: 10.2138/am.2014.4657

Doerfelf, C., Feldmann, T., Daenzer, R., Demopoulos, G. P. (2015). Stability of continuously produced Fe(II)/Fe(III)/As(V) co-precipitates under periodic exposure to reducing agents. *Chemosphere* vol. 138: 239-246. DOI: 10.1016/j.chemosphere.2015.05.096.

Duarte, G., Ciminelli, V. S. T., Dantas, M. S. S., Duarte, H. A., Vasconcelos, I. F., Oliveira, A. F., Osseo-Asare, K. (2012). As(III) immobilization on gibbsite: Investigation of the complexation mechanism by combining EXAFS analyses and DFT calculations. *Geochim. Cosmochim. Ac.* vol. 83: 205–216. DOI: 10.1016/j.gca.2011.12.019.

Farrell, J. W., Fortner, J., Work, S., Avendano, C., Gonzalez-Pech, N. I., Araiza, R. Z., Li, Q., Álvarez, P. J. J., Colvin, V., Kan, A., Tomson, M. (2014). Arsenic removal by nanoscale magnetite in Guanajuato, Mexico. *Environ. Eng. Sci.* vol. 31 (7): 1-10. DOI: 10.1089/ees.2013.0425.

Freitas, E. T. F., Montoro, L. A., Gasparon, M., Ciminelli, V. S. T. (2015). Natural attenuation of arsenic in the environment by immobilization in nanostructured hematite. *Chemosphere* vol. 138: 340–347. DOI: 10.1016/j.chemosphere.2015.05.101.

Gloter, A., Douiri, A., Tencé, M., Colliex, C. (2003). Improving energy resolution of EELS spectra: An alternative to the monochromator solution. *Ultramicroscopy* vol. 96 (3-4): 385–400. DOI: 10.1016/S0304-3991(03)00103-7.

Guo, H., Ren, Y., Liu, Q., Zhao, K., Li, Y. (2013) Enhancement of Arsenic Adsorption during Mineral Transformation from Siderite to Goethite: Mechanism and Application. *Environ. Sci. Technol.* vol. 47: 1009–1016. DOI: 10.1021/es303503m

Ladeira, A. C. Q., Ciminelli, V. S. T. (2004). Adsorption and desorption of arsenic on an Oxisol and its constituents. *Water Res.* vol. 38 (8): 2087–2094. DOI: 10.1016/j.watres.2004.02.002.

Liu, C-H., Chuang, Y-H., Chen, T-Y., Tian, Y., Li, H., Wang, M-K., Zhang, W. (2015). Mechanism of arsenic adsorption on magnetite nanoparticles from water: thermodynamics and spectroscopic studies. *Environ. Sci. Technol.* vol. 49 (13): 7726-7734. DOI: 10.1021/acs.est.5b00381.

Masue, Y., Loeppert, R. H., Kramer, T. A. (2007). Arsenate and Arsenite Adsorption and Desorption Behavior on Coprecipitated Aluminum : Iron Hydroxides. *Environ. Sci. Technol.* vol. 41 (3): 837–842. DOI: 10.1021/es061160z

Mello, J. W. V., Gasparon, M., Silva, J. (2017) Effectiveness of Fe and Al hydroxides for treatmet of AMD water contaminated witth arsenic. Manuscript submitted for publication.

Moradlou, O., Farashah, S. D., Masumian, F., Banazadh, A. Z. (2016). Magnetite nanoplates decorated on anodized luminum oxide nanofibers as a novel adsorbent for efficient removal of As(III). *Int. J. Environ. Sci. Technol.* vol. 13: 1149-1158. DOI: 10.1007/s13765-016-0941-3.

Morin, G., Ona-Nguema, G., Wang, Y., Menguy, N., Juillot, F., Proux, O., Guyot, F., Calas, G., Brown, G. E. (2008). Extended X-ray absorption fine structure analysis of arsenite and arsenate adsorption on maghemite. *Environ. Sci. Technol.* vol. 42 (7): 2361–2366. DOI: 10.1021/es072057s.

Morin, G., Wang, Y., Ona-Nguema, G., Julliot, F., Calas, G., Menguy, N., Aubry, E., Bargar, J. R., Brown Jr., G. (2009). EXAFS and HRTEM evidence for As(III)-containing surface precipitates on nanocrystalline magnetite: implications for As sequestration. *Langmuir* vol. 25 (16): 9119-9128. DOI: 10.1021/la900655v.

Niederberger, M., Cölfen, H. (2006). Oriented attachment and mesocrystals: Non-classical crystallization mechanism based on nanoparticle assembly. *PCCP* vol. 8: 3271-3287. DOI: 10.1039/b604589h.

Ona-Nguema, G., Morin, G., Juillot, F., Calas, G., Brown, G. E. (2005). EXAFS analysis of arsenite adsorption onto two-line ferrihydrite, hematite, goethite, and lepidocrocite. *Environ. Sci. Technol.* vol. 39 (23): 9147–9155. DOI: 10.1021/es050889p.

Ona-Nguema, G., Morin, G., Wang, Y., Foster, A. L., Juillot, F., Calas, G., Brown, G. E. (2010). XANES evidence for rapid arsenic(III) oxidation at magnetite and ferrihydrite surfaces by dissolved O(2) via Fe(2+)-mediated reactions. *Environ. Sci. Technol.* vol. 44 (14): 5416–5422. DOI: 10.1021/es1000616.

Penn, R. L., Soltis, J. A. (2014). Characterizing crystal growth by oriented aggregation. *Cryst. Eng. Comm.* vol. 16: 1409-1418. DOI: 10.1039/c3ce41773e

Schwertmann, U., Fittzpatrick, R. W., Taylor, R. M., Lewis, D. G. (1979). The influence of aluminum on iron oxides. part ii. preparation and properties of a1-substituted hematites. *Clays Clay Miner.* vol. 27 (2): 105–112.

Schwertmann, U., Cornell, R.M. (2000). *Iron Oxides in Laboratory:* preparation and characterizaation: Weinheim, Germany. Wiley-VHC

Schwertmann, U., Murad, E. (1990). The Influence of Aluminum on Iron Oxides: XIV. Al-Substituted Magnetite Synthesized at Ambient Temperatures. *Clays Clay Miner.* vol. 38 (2): 196–202. DOI: 10.1346/CCMN.1990.0380211.

Silva, J., Mello, J. W. V., Gasparon, M., Abrahão, W. A. P., Ciminelli, V. S. T., Jong, T. (2010). The role of Al-goethites on arsenate mobility. *Water Res.* vol. 44 (19): 5684–5692. DOI: 10.1016/j.watres.2010.06.056.

Smedley, P.; Kinniburgh, D. (2002). A review of the source, behaviour and distribution of arsenic in natural waters. *Appl. Geochem* vol. 17 (5): 517–568. DOI: 10.1016/S0883-2927(02)00018-5.

Smith, E.; Naidu, R.; Alston, M. (1998). Arsenic in the soil environment: a review. *Adv. Agron.* vol. 64: 149–195. DOI: 10.1016/S0065-2113(08)60504-0.

Smith, E.; Naidu, R.; Weber, J.; Juhasz, A. L. (2008). The impact of sequestration on the bioaccessibility of arsenic in long-term contaminated soils. *Chemosphere* vol. 71 (4): 773–780. DOI: 10.1016/j.chemosphere.2007.10.012.

Sugimoto, T., Matijević, E. (1980). Formation of uniform spherical magnetite particles by crystallization from ferrous hydroxide gels. *J. Colloid Interface Sci.* vol. 74 (1): 227–243. DOI: 10.1016/0021-9797(80)90187-3.

Tamaura, Y., Katsura, T. (1981). Studies on the Oxidation of Iron(II) Ion during the Formation of Fe3O4 and alpha-FeO(OH) by Air Oxidation of Fe[OH]2 Suspensions. *J. Chem. Soc. Dalton.* 1807–1811.

Taylor, R. M.; Schwertmann, U. (1978). The influence of aluminum on iron oxides. Part I. The influence of Al on Fe oxide formation from the Fe(II) system. *Clays Clay Miner.* vol. 26 (6): 373–383.

Türk, T., Alp, I. (2014). Arsenic removal from aqueous solutions with Fe-hydrotalcite suported magnetite nanoparticle. *J.Ind.Eng.Chem.* vol. 20: 732-738. DOI: 10.1016/j.jiec.2013.06.002.

Violante, A., Gaudio, S. D., Pigna, M., Ricciardella, M., Banerjee, D. (2007). Coprecipitation of Arsenate with Metal Oxides. 2. Nature, Mineralogy, and Reactivity of Iron(III) Precipitates. *Environ. Sci. Technol.* vol. 41 (24): 8275–8280. DOI: 10.1016/0021-9797(80)90187-3.

Violante, A., Pigna, M., Gaudio, S. D., Cozzolino, V., Banerjee, D. (2009). Coprecipitation of arsenate with metal oxides. 3. Nature, mineralogy, and reactivity of iron(III)-aluminum precipitates. *Environ. Sci. Technol.* vol. 43 (5): 1515–1521. DOI: 10.1021/es802229r.

Violante, A., Ricciardella, M., Gaudio, S. D., Pigna, M. (2006). Coprecipitation of arsenate with metal oxides: nature, mineralogy, and reactivity of aluminum precipitates. *Environ. Sci. Technol.* vol. 40 (16): 4961–4967. DOI: 10.1021/es052321m.

Wang, Z., Xiao, D., Bush, R. T., Liu, J. (2015). Coprecipitated arsenate inhibits thermal transformation of 2-line ferrihydrite: implications for long-term stability of ferrihydrite. *Chemosphere* vol. 122: 88-93. DOI: 10.1016/j.chemosphere.2014.11.017.

Waychunas, G. A., Kim, C. S., Banfield, J. F. (2005). Nanoparticulate iron oxide minerals in soils and sediments: Unique properties and contaminant scavenging mechanisms. *J. Nanoparticle Res.* vol. 7 (4-5): 409–433. DOI: 10.1007/s11051-005-6931-x.

Williams, D. B., Carter, C. B. (2009). *Transmission Electron Microscopy*. Second Edition, New York, USA. Springer New York.

Xue, X., Penn, R. L., Leite, E. R., Huang, F., Lin, Z. (2014). Crystal growth by oriented attachment: kinetic models and control factors. *Cryst. Eng. Comm.* vol. 16: 1419-1429. DOI: 10.1039/c3ce42129e.

Yuwono, V. M., Burrows, N. D., Soltis, J. A., Penn, R. L. (2010). Oriented aggregation: Formation and transformation of mesocrystal. *JACS* vol. 132 (7): 2163–2165. DOI: 10.1021/ja909769a.

Zhang, H.; Banfield, J. F. (2012). Energy calculations predict nanoparticle attachment orientations and asymmetric crystal formation. *J. Phys. Chem. Lett.* vol. 3: 2882–2886. DOI: 10.1021/jz301161j.

Zhang, X., Jia, Y., Wang, S., Pan, R., Zhang, X. (2012). Bacterial reduction and release of adsorbed arsenate on Fe(III)-, Al- and coprecipitated Fe(III)/Al-hydroxides. *J. Environ. Sci.* vol. 24 (3): 440-448. DOI: 10.1016/S1001-0742(11)60792-4.

CHAPTER 5. The fate of adsorbed arsenic onto pure and aluminous ferrihydrite upon ageing

Abstract

Aluminium (Al) is ubiquitous in natural environments as well as in acid mine drainage waters. It is present along with iron (Fe) (hydr)oxides as an impurity or substituted for Fe. However, the effects of Al on arsenic (As) sorption behaviour onto Al-Fe-(hydr)oxides is scarley studied, specially the fate of As upon ageing its host phases. In this work, the partitioning of As(V) adsorbed onto Al-free and Al-containing ferrihydrite (Fh) was investigated upon ageing precipitates up to 120 days at circum-neutral pH and 30 ºC. The effects of Al-for-Fe substitution in Fh, and on As(V) uptake by Al-Fh were also studied. The inductively coupled plasma with optical emission spectrometry (ICP-OES) data showed that As(V) content in solution decreased for all Fh suspensions upon ageing, from 150.28 to 12.61 mg L-1 for Al-free Fh, after 1 day ageing, and down to 3.96 mg L^{-1} at day 120. For Al-Fh samples, the As(V) concentration upon ageing was even lower, from 150.28 down to 1.30 mg L^{-1} in the course of the experiment. The maximum Al-for-Fe susbstitution in Fh was shown to be around 21% mol mol^{-1}, based on the the scanning transmission electron microscopy energy dispersive X-ray spectroscopy (STEM-EDS) analysis, and the As/(Al+Fe) molar ratio between 0.062 – 0.075. Electron energy-loss spectroscopy (EELS) analysis at the Fe $L_{2,3}$ ionization edge suggested the substituted-Al promotes an increasing in the average charge density surrounding Fe atoms, which might be related to the relatively larger As-uptake by Al-Fh precipitates. High resolution transmission electron microscopy (HRTEM) data showed a progressive oriented aggregation of Fh nanoparticles (NPs) upon ageing, and energy filtered transmission electron microscopy (EFTEM) analysis evidenced the presence of arsenic trapped in between the attached Fh NPs in the aggregates. These results support a mechanism of As incorporation in the crystalline nanostructured Al-Fe-(hydr)oxides. This mechanism relies on the oriented aggregation based crystal growth. To the authors knowledge, this is the first time this mechanism is shown for As immobilizatizon in the bi-metal Al-Fe-(hydr)oxides.

Keyworks: Arsenic partitioning, As immobilization, Al-Fe-(hydr)oxides

5.1. Introduction

Nanostructured iron (hydr)oxides show high efficient capacity for heavy metals uptake from wastewater (Smith et al. 1998; Smedley and Kinniburgh 2002; Hua et al. 2012; Carabante et al. 2014; Adeleye et al. 2016; Lata and Samadder 2016), and several attempts have been made to enhance the arsenic adsorption capacity of Fe-oxides either synthesised from fresh or iron-rich waste materials (Tang et al. 2011; Akin et al. 2012; Cao et al. 2012; Feng et al. 2012; Carabante et al. 2014). As aluminium is ubiquitous in natural environment and as well as in acid mine drainage water, the understanding of its role in As uptake by Al-containing Fe-(hydr)oxides is crucial to develop remediation technologies for As immobilization by such mixed phases. Therefore, the combination of Al and Fe in adsorption and co-precipitation experiments for water treatment has opened a discussion on the role of Al in arsenic uptake by such bi-metal (hydr)oxides. Silva et al. (2010) reported an increased As loading capacity for synthetic Al-goethite compared to pure goethite. Masue et al. (2007) and Adra et al. (2016) reported different findings in similar investigations on As(V) adsorption onto Al-bearing ferrihydrite at neutral pH. Adra et al. (2016) observed an increase of As(V) sorption densities when increasing Al:Fe molar ratio, whilst Masue et al. (2007) reported no significant change in As(V) adsorption when increasing Al:Fe molar ratio up to 20% mol mol^{-1}. As for arsenite (As(III)) sorption, Masue et al. (2007) and Adra et al. (2016) found similar results, reporting a decrease of As(III) adsorption when increasing Al:Fe molar ratio. In these studies, however, Masue et al. (2007) and Adra et al. (2016) have not investigated the behaviour of adsorbed As over the time. To the authors knowledge no up-to-date literature have reported the partitioning of adsorbed arsenic onto the Al-bearing ferrihydrite and its fate upon ageing at neutral pH and ambient temperature. Our previous works have suggested that Al plays a major role in As immobilization in the structure of oriented aggregates of Al-Fe-(hydr)oxides nanoparticles found both in natural and synthetic samples (Freitas et al. 2015, 2016). Our own data suggested that adsorbed As onto primary nanoparticles of Al-containing Fe-(hydr)oxides could be incorporated in the crystalline nanoparticles' aggregates found in both aged natural and synthetic samples shown in chapters 3 and 4. However, the detailed ageing/recrystallization mechanisms taking place following the initial adsorption of As, and the role of Al in these processes remain to be fully understood. In this present work, we investigated the mechanism of As immobilization in the nanocrystalline Al-Fe-(hydr)oxide by studying As(V)-adsorbed Al-free and Al-bearing ferrihydrite over the time. Our findings highlight the arsenic partition in the nanostructured aggregates of Al-Fe-(hydr)oxides and its fate upon ageing.

5.2. Experimental

All labware used were washed and kept in 1 mol L^{-1} acid nitric bath for 24 hours and subsequently kept in Milli-Q water (Millipore) bath overnight, and triple rinsed with Milli-Q water afterwards prior to use. Series of Al-free and Al-containing ferrihydrite (Fh) samples were produced from mixed iron and aluminium nitrate solutions, in the absence and presence of As(V), following a modified procedure of Schwertmann and Cornell (2000). Appropriate volumes of five different 0.1 mol L^{-1} mixed $Fe(NO_3)_3.9H_2O$ and $Al(NO_3)_3.9H_2O$ (Sigma-Aldrich, ≥98.0%) solutions were prepared, and the initial Al/(Al+Fe) molar ratios (R) were 0, 5, 10, 20 and 30%. mol mol^{-1} The pH of Fe and Al nitrate solutions was 1.72 ± 0.02. Appropriate volume of 0.160 mol L^{-1} As(V) stock solution was prepared from $Na_2HAsO_4.7H_2O$ (Sigma-Aldrich, ≥98.0%).

5.2.1. Al-free and Al-containing ferrihydrite

A series of ferrihydrite was performed by titrating 50 mL of each mixed 0.1 mol L^{-1} iron and aluminium nitrate solution with 1 mol L^{-1} NaOH (Fmaia, 97%), while stirring, at a rate of approx. 1 mL min^{-1} to a final pH 7.0 ± 0.3, at ambient temperature. A reddish-brown precipitate was formed at the time NaOH was being added. Each ferrihydrite suspension (Al_RFh) was placed into dialysis tubing cellulose membrane (Sigma-Adrich) and filled tubes dialysed against 2 L of cold Milli-Q water during 2 days inside a refrigerator at approx. 15 ºC. The cold water was replaced periodically, every 1-3 hours for 4-5 times in the first day, left overnight, and every 2-4 hours in the following day. The conductivity of the water was monitored every replacement in the second day and was <12 mS cm^{-1} after the last change. Each ferrihydrite suspension (50 mL) was placed in graduated flask and volume brought to 150 mL with sodium chloride solution to keep the ionic strength around 10 mmol L^{-1} NaCl. The pH of suspensions was 5.9 ± 0.1.

5.2.2. Adsorption of As(V) on Al-free and Al-containing ferrihydrite

The adsorption of arsenic was achieved by adding the same volume of 2 mL As(V) stock solution in each 150 mL of Al_RFh suspension. The pH increased to 8.3 ± 0.1 after the arsenic addition. The samples were shaken in darkness for 24 hours at 30 ºC and 200 rpm in a thermostatic shaker (New Brunswick Scientific Edison). Each As-adsorbed ferrihydrite suspension (Al_RFh-As) was split in 6 aliquots in capped glass vials and left ageing for 8, 15, 30, 60 and 120 days in a water bath at 30ºC. The aliquots corresponding to day 1 were recovered right after have shaken suspensions for 24 hours.

5.2.3. Sample preparation for TEM, chemical and Raman analysis

At the specific ageing time the glass vials of each correspondent aliquot were taken from the water bath and homogenised by shaking them manually, and pH measured. For TEM sampling, each Al_RFh-As suspension was pipette and a drop placed on an ultra-thin film of C-coated Cu-TEM support grid. The grids were laid on Whatman® filter papers to remove excess water of the drop and left dry at room temperature prior TEM analysis. Suspensions of each correspondent aliquot were transferred to Falcon™ 50 mL conical centrifuge tubes and centrifuged at 4000 rpm for 20 min. Supernatants were recovered and stored in a refrigerator prior chemical analysis by a Perkin Palmer 7300 inductively coupled plasma with optical emission spectrometre (ICP-OES). For Raman spectroscopy, the solids in centrifuge tubes were lyophilised at approx. 50 μmHg for 24 hours prior analysis by a LabRam-HR 800 (Horiba/Jobin Yvon) spectrograph equipped with an Olympus BX-41 microprobe provided lens of 10, 50 and 100X and an additional macro lens of 40 mm for Raman spectroscopic application. A 632.8 nm excitation from a helium-neon laser was focused to a spot of 1-2 μm^2 at the samples.

The samples were analysed using different transmission electron microscopy (TEM) techniques: high resolution TEM (HRTEM), selected area electron diffraction (SAD), scanning TEM (STEM), energy dispersive X-ray spectroscopy (EDS), electron energy-loss spectroscopy (EELS), and energy-filtered TEM (EFTEM). Electron microscopy analyses were performed by using a LaB_6-TEM Tecnai G^2 20 SuperTWIN (FEI), operating at 200 kV, equipped with a Si(Li) EDS detector (EDAX) with 30 mm^2 window, and a post-column Gatan Image Filter (GIF) Quantum SE System equipped with a bright and annular dark field (BF/ADF) STEM detector, an Orius SC200 and a GIF (US1000FTXP) CCD cameras. Energy dispersive X-ray and EEL spectra were collected in STEM mode. For EFTEM images EELS elemental maps were performed by using objective aperture to cut off some diffracted beams. High resolution TEM images and SAD patterns were acquired by using elastic electrons adjusting a 10 eV slit at the zero-loss peak (ZLP) of EEL spectra. STEM-EDS relative quantification was performed via Genesis software (EDAX) by using the Elements Cliff-Lorimer-based method for thin specimens (Cliff and Lorimer 1975). The SAD patterns (SADPs) were performed at same camera length (30 mm) and recorded by using elastic scattered electrons only by filtering the zero-loss peak (ZLP) of EELS spectra. The short camera length was used to project the SADP in the GIF CCD camera. The scale bar of SADPs was calibrated by using a diffraction grating replica, parallel, 2,160 lines mm^{-1} standard sample (Ted Pella, INC). The SADPs were analysed with the help of the DiffTools suite of software (Mitchell 2008) using the Digital Micrograph (DM) software (Gatan). TEM images were manipulated and treated by means of both DM and ImageJ (Wayne Rasband, National Institutes of Health, USA) softwares.

5.2.4. Desorption of arsenate from precipitates

The removal of As(V) from dried solids of samples Al_RFh-As at days 1 and 120 was performed in 2 consecutive steps, in duplicate for soluble and adsorbed arsenic fractions, based on a protocol for sequential extraction (Pantuzzo et al. 2008; Pantuzzo and Ciminelli 2010). In the step 1, each solid (25 mg) was re-suspended in equal volume of Milli-Q water (50 mL) in centrifuge Falcon^{TM} tubes. The suspensions were shaken for 1 hour at 200 rpm and 30 ºC, and then centrifuged at 4000 rpm for 10 min. Supernatants were recovered for ICP-OES analysis. In the step 2, the same volume (50 mL) of 0.2 mol L^{-1} Na_2HPO_4 (Sigma-Aldrich) was added to each solid (not dried after the first step) to have an initial P:As molar ratio of 550:1. The large phosphate concentration was to facilitate As(V) desorption. The initial pH after phosphate addition was 9.1 ± 0.2. Samples were then shaken at 200 rpm for 24 h at 30 ºC, and then centrifuged at 4000 rpm for 20 min afterwards. Supernatants were recovered for ICP-OES analysis as well as an aliquot of Na_2HPO_4 solution. When the As content was found to be near or below the quantification limit given by the calibration curve, As(V) was measured by hydrated generation (HG)-ICP-OES.

5.3. Results and discussion

5.3.1. As, Al and Fe content in solids and supernatants

The concentration of As in supernatants recovered from each Al_RFh-As suspension was measured by ICP-OES, and in an aliquot of As(V) stock solution as well. The initial arsenate loaded in each aliquot of suspensions was 150.28 mg L^{-1}, and the residual As(V) content in the supernatants over the time is shown in Figure 5.1. In all cases, the As(V) content in supernatants decreased as samples aged. This indicates a relatively gradual increasing of As(V) bound to solids during the course of the experiment (95.4 ± 0.8% at day 1, and 99.0 ± 0.5% at day 120 out of total initial loaded As).

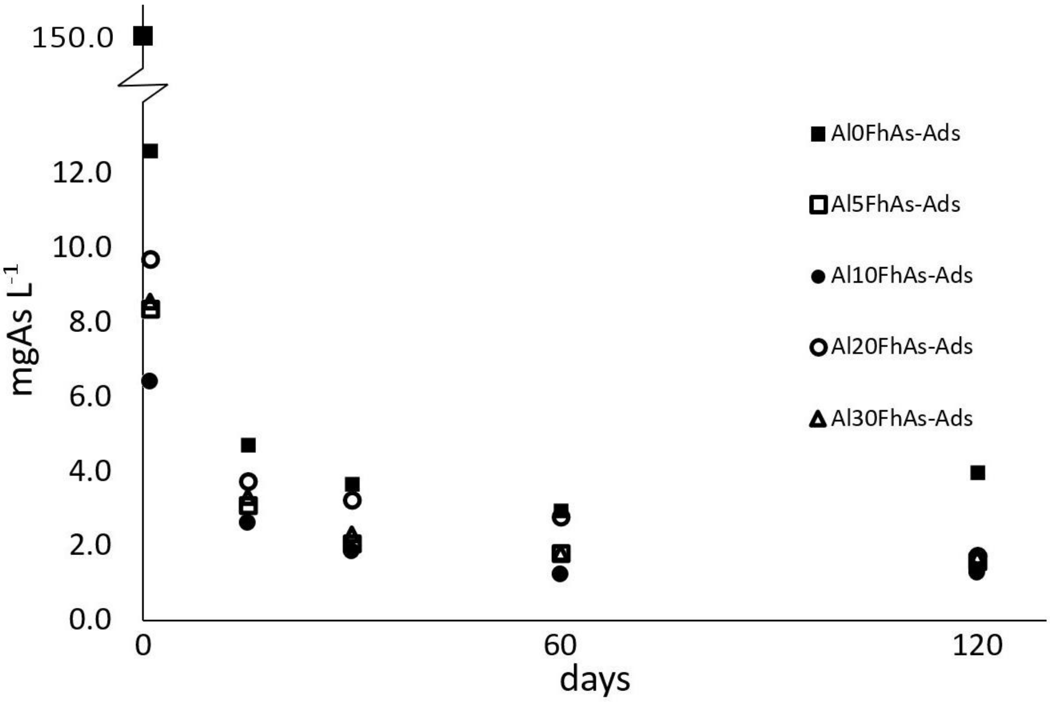

Figure 5.1. As(V) concentration (mg L^{-1}) in supernatants recovered from of suspensions of samples Al_RFh-As. R stands for the initial Al/(Al+Fe) molar ratio in the precipitates. The point at day 0 is the As concentration added to each suspension.

The pH range of suspensions upon ageing (8.3 ± 0.2 to 7.6 ± 0.3; see Appendices) remained slightly above the PZC values of 7.6 (Masue et al. 2007) and 7.8 (Cornell and Schwertmann 2003) for Al:Fe (0:1) oxyhydroxides, and 8.2 for Al:Fe (1:4) oxyhydroxides (Masue et al. 2007). The PZC may be shifted to lower pH upon adsorption of anions such as As(V) onto Al oxyhydroxides (Anderson et al. 1976) and ferrihydrite (Jain et al. 1999), thus hindering the attraction of more anions. The shift of the isoelectric point towards lower values upon As(V) adsorption is also reported for goethite (8.1 to 6.3) and for gibbsite (7.7 to 7.0) (Ladeira and Ciminelli 2004). Nonetheless, our results show further decreasing of arsenic in solution over the time, as expected for inner sphere complexation. Indeed, the data from the desorption experiments (see Appendices) showed the majority of As(V) (approx. 66%, i.e. ~37 $mg_{As(V)}\ g_{solid}^{-1}$) incorporated into the solids or, in other words, not extracted by phosphate solutions. As an expected result, nearly the same amount of As(V) was extracted from solids at days 1 and 120. Furthermore, the lyophilization of solids under vacuum prior desorption experiments may be contributed to promote aggregation of solids and phase transformation upon release of structural water. Indeed, non-identified phases were observed in lyophilized solids by Raman analysis (spectra not shown).

In general, Al is shown to favour As(V) uptake by Al-Fh compared to pure Fh. However, the actual role of Al-for-Fe substitution in Fh precipitates that could explain the increased As(V) adsorption is still to be fully understood. Adra et al. (2013) showed that arsenate forms inner-sphere complexes bound to Fe sites onto Al-ferrihydrites, but no As-Al interaction was shown to contribute to the As K-edge extended X-ray absorption fine structure data (Adra et al. 2013). Based on the literature data, Adra et al. (2016) attributed the higher As(V) sorption density for Al-ferrihydrites to the existence of more protonated sites compared to Al-free Fh, since their experiments were performed in a pH (6.5) below the PZC. The increased protonated sites would likely be due to the formation of outer-sphere complexes that form hydrogen bonds with =Al-OH or =Fe-OH (Adra et al. 2016). These explanations, however, fall short of the understanding the As(V) adsorption behaviour in our experiments, in which the pH remained above the PZC. In the next sections, we discuss our own EELS data that suggest a likely increase of the surrounding charge of Fe atoms in Al-substituted Fh. This increased charge density of Fe could favour the attraction of more arsenate anions and hence the increasing of As(V) adsorption on Fe sites in Al-ferrihydrites compared to pure Fh.

5.3.2. Solid phases

5.3.2.1. Al-free and Al- ferrihydrites

The ferrihydrite precipitates formed without Al presented larger aggregates of nanoparticles (NPs) (Figure 5.2). At day 15, larger nanoparticles (10 nm size) were observed (Figure 5.2.b), likely goethite nucleated from ferrihydrite. From day 60 on, needle-like goethite NPs (30 – 50 nm) and akaganéite/lepidocrocite with an oblong shape were clearly observed (Figures 5.2.c-d). The formation of akaganéíte may be favoured by the presence of chloride (10 mmol L^{-1}) in suspensions. Hematite crystals were also observed at day 120 (Figure 5.2.d). These phases likely grew following the Ostwald Ripening model, which leads to the formation of larger single crystals grown at expensive of smaller particles, and whose morphology often keeps the crystal symmetry.

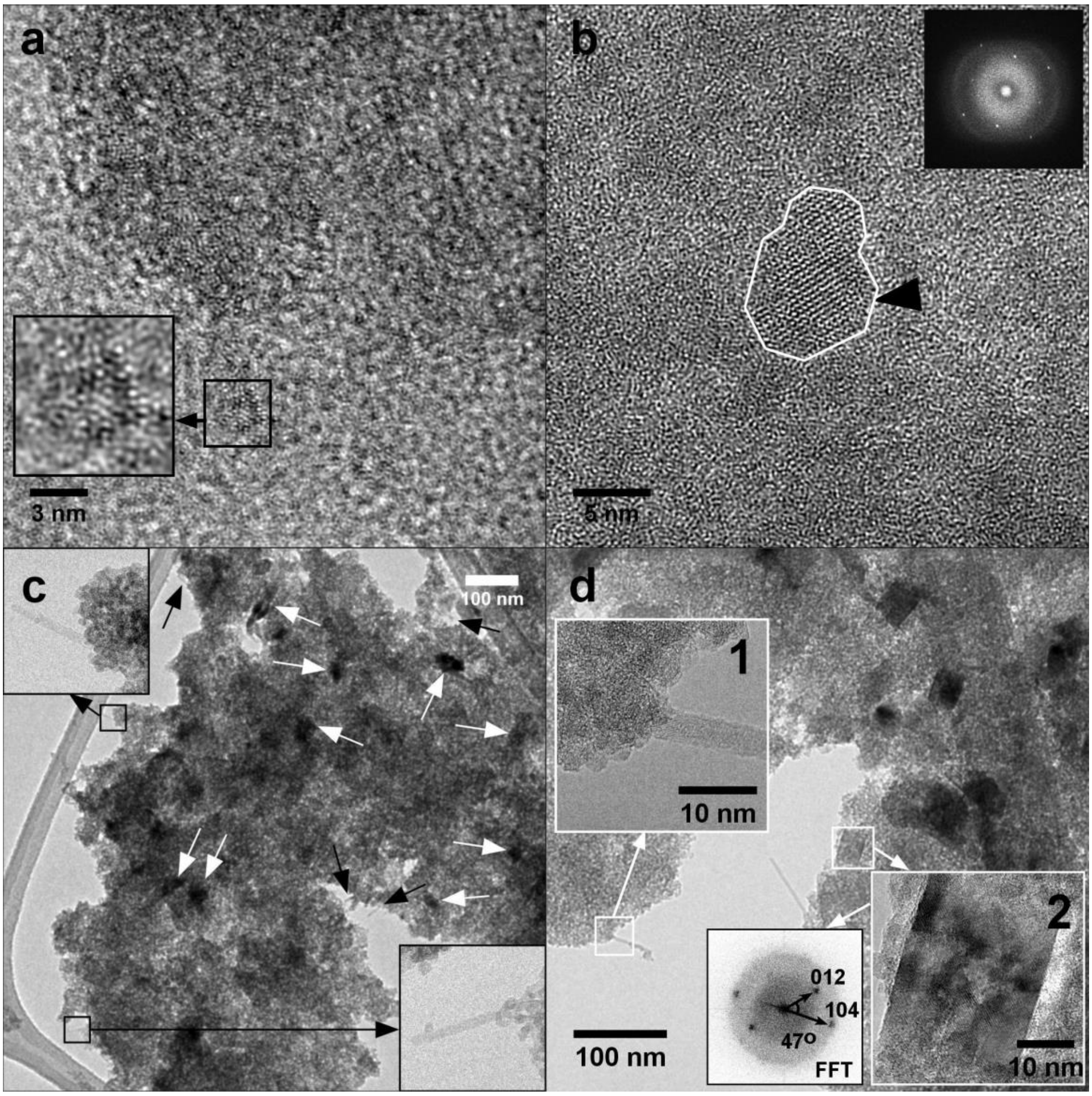

Figure 5.2. HRTEM images showing the Al-free ferrihydrite (Al_0Fh) nanoparticles aggregates at day 1 (a), 15 (b), 60 (c) and 120 (d). The Fast Fourier Transform (FFT) in the insets in (b and d) shows spots indicating lattice fringes of the pointed larger recrystallized NP. The larger crystallites indicated by black and white arrows in (c) are goethite and akaganéite, respectively, formed upon ageing Fh in the presence of 10 mmol L^{-1} NaCl. The insets 1 and 2 in (d) show goethite and hematite crystals, respectively.

As for Al-ferrihydrites, the results show that the NPs' aggregates have a different morphology compared to the pure Fh. The aluminous Fh precipitates present a net-like morphology given by the formed stripes of oriented attached NPs which yielded a porous-like structure produced by the voids in between the nanoparticles (Figures 5.3.b-c). The presence of Al in Fh seems to have favoured the oriented aggregation crystal growth regime. The NPs have likely grown along [110] direction (inferred from HRTEM images). Indeed, the [110] is one of the predicted common favourable growth directions in an attachment event of two 4 nm compounds for hexagonal crystal system with *P*63mc space group (Zhang and Banfield 2012), that is the same space group for 2-line ferrihydrite (Michel et al. 2007).

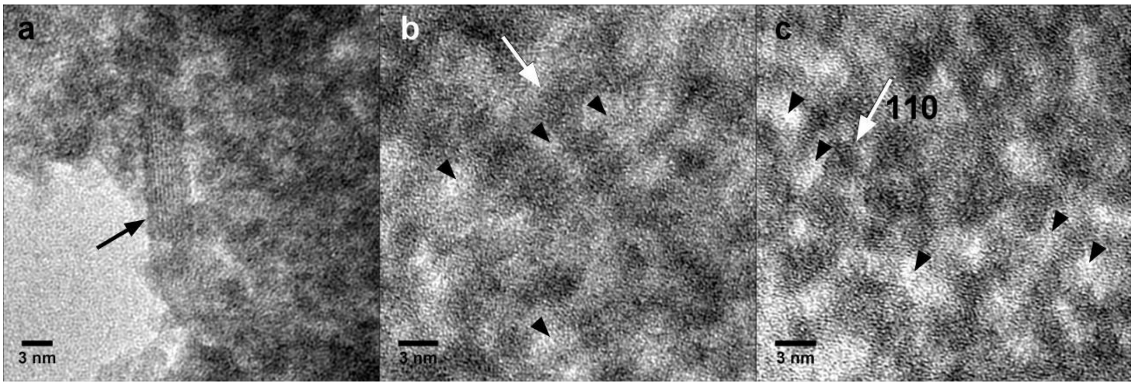

Figure 5.3. HRTEM images of samples Al_0Fh (a), $Al_{10}Fh$ (b), and $Al_{20}Fh$ at 60 days ageing. A needle-like goethite crystal among the aggregates of Fh NPs is pointed in (a). The ordered strips of Fh NPs are shown in (b-c), whose likely growth direction [110] is indicated by the white arrow. The porous-like structure formed by voids in between the stripes of NPs is indicated by black arrows in (b-c).

The Al-ferrihydrite samples $Al_{10}Fh$ and $Al_{20}Fh$, whose respective R molar ratios 9.6 ± 0.8% and 19.8 ± 0.7% were confirmed by STEM-EDS, have not undergone phase transformation within 120 days. This delaying comparing to Al-free Fh is due to the presence of substituted Al which retards phase transformation (Cornell and Schwertmann 2003; Violante et al. 2007). Indeed, careful analysis of the SAD patterns for both samples showed two main characteristic d_{hkl} (d_{110} and d_{300}) spaces very similar, but shifted to lower d-spaces, to those of Al_0Fh (Figure 5.4). This contraction is consistent with the smaller Al^{3+} atom substitution for Fe^{3+} in the aluminous Fh samples.

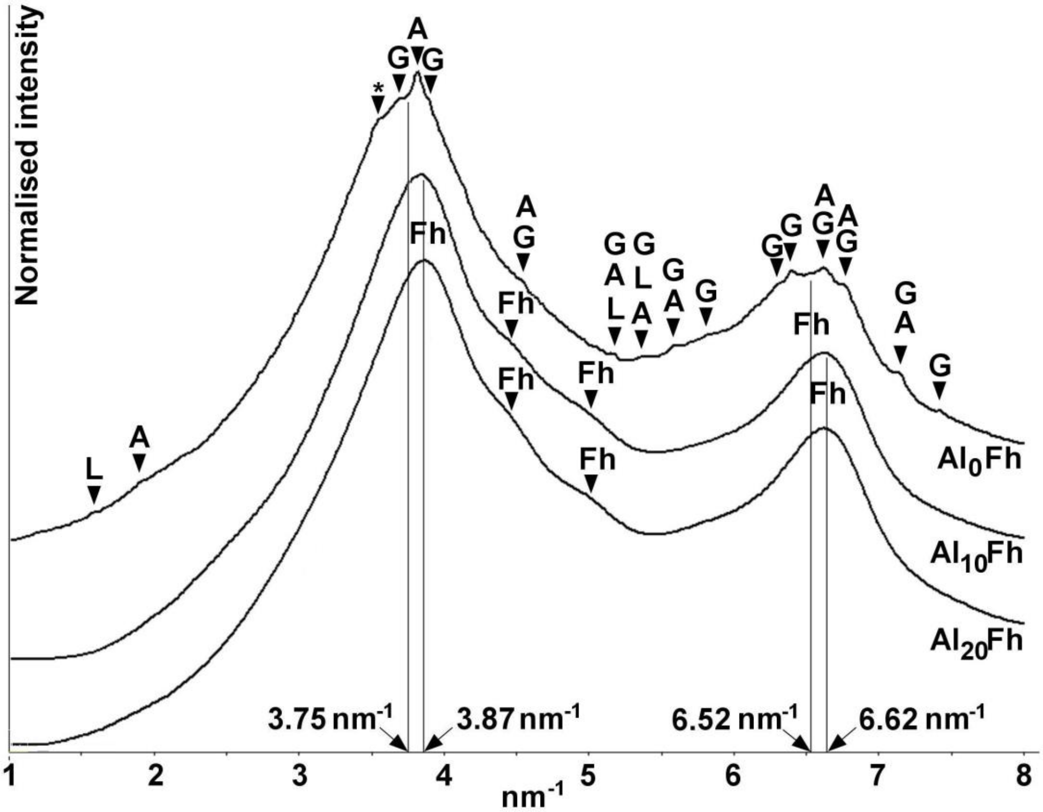

Figure 5.4. Line profiles performed from the selected area diffraction patterns (SADPs) of samples Al_0Fh, $Al_{10}Fh$, and $Al_{20}Fh$ all at day 60. Akaganéite (A), lepidocrocite (L), and goethite (G) were identified in Al_0Fh sample.

The two peaks of Al_0Fh ($d^*_{110} = 3.75$ nm^{-1} and $d^*_{300} = 6.52$ nm^{-1}, i.e. $d_{110} = 0.267$ nm and $d_{300} = 0.153$ nm, respectively) are shifted to lower d-spaces in SADPs for aluminous Fh samples ($d^*_{110} = 3.87$ nm^{-1} and $d^*_{300} = 6.62$ nm^{-1}, i.e. $d_{110} = 0.258$ nm and $d_{300} = 0.151$ nm, respectively). The two weaker peaks in the SADPs for aluminous Fh samples centred at about 4.50 nm^{-1} (0.222 nm) and 5.00 nm^{-1} (0.200 nm) correspond to planes (112) and (113), respectively. The peak indicated with a star (*) at about 3.5 nm^{-1} (2.86 nm) did not match any reflection for other Fe^{3+} oxyhydroxide phases (hematite, feroxyhyte, maghemite, and bernalite).

The STEM-EELS analysis of Fh precipitates (Figure 5.5) shows a chemical shift of Fe $L_{2,3}$-edge towards higher energy-loss for Al-ferrihydrites compared to pure Fh. The energy shift of about 0.5 eV is shown at the spectra onset energies for Al_0Fh (709.00 ± 0.25 eV) and for $Al_{10,20}Fh$ samples (709.50 ± 0.25 eV). The error on the onset energy was considered as the observed spectra shift of 0.25 eV by double checking the zero-loss peak (ZLP) right before and after the acquisition of the EEL core loss spectra in each measurement. This chemical shift suggests a relative higher charge density surrounding Fe atoms in Al-Fh. It is also evidenced by the increasing of the Fe $L_{2,3}$ white-line ratios (WLR) with the increasing of substituted Al in ferrihydrite. The WLR were measured by taken the integral intensity ratio of the L_3 ($2p_{3/2} \rightarrow 3d$) and L_2 ($2p_{1/2} \rightarrow 3d$) excitation peaks of the Fe $L_{2,3}$-edge. The script *Measure EELS Peak Intensity* (Mitchell and Schaffer 2005) was used to measure the Fe-$L_{2,3}$ peaks.

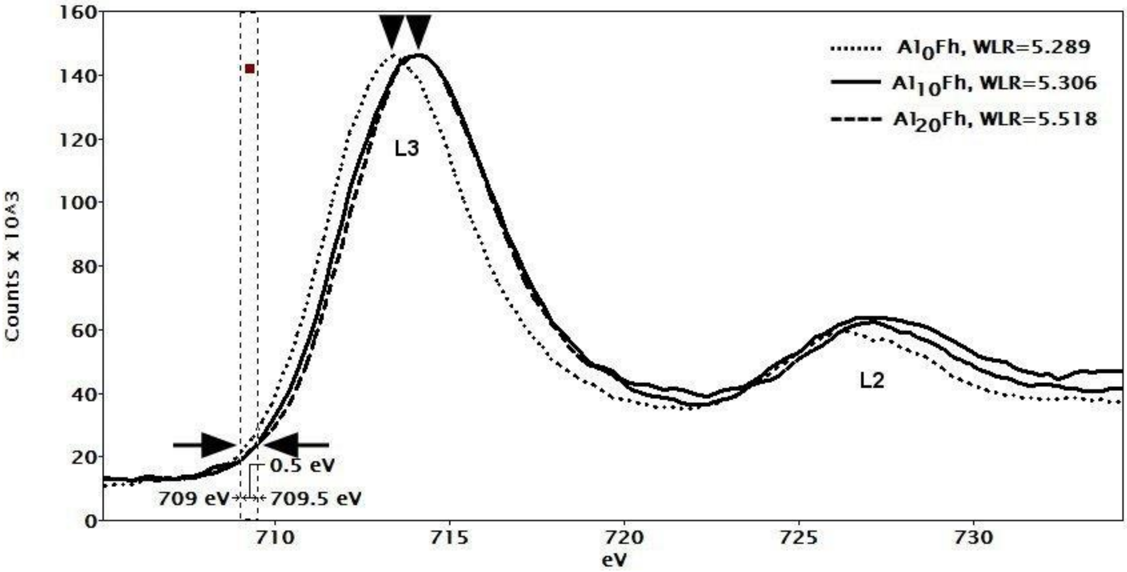

Figure 5.5. EEL spectra of samples Al_0Fh, $Al_{10}Fh$, and $Al_{20}Fh$ at day 120, showing the (white-lines) L_3 ($2p_{3/2} \rightarrow 3d$) and L_2 ($2p_{1/2} \rightarrow 3d$) excitation peaks of the Fe $L_{2,3}$-edge. The white-line ratios (WLR) of Fe $L_{2,3}$ peaks are shown at the legend.

The chemical shift and the changing in the WLR have been ascribed to a changing in the oxidation state of transition metals (Colliex et al. 1991; Egerton 2008; Tan et al. 2012), but it is unlike that Fe has an average higher oxidation state in the Al-Fh system as there would be need a high electronegative ion to stabilize Fe(IV). The observed changing in the electronic density of Fe might be caused by the likely displacement of some electrons from Fe towards Al atoms in the lattice due to the higher electrostatic potential of Al(III) compared to Fe(III), thus giving to Fe atoms a relative higher positive charge density. The increased charge surrounding Fe in the Al-Fh may contribute to enhance As uptake respectively to Al-free Fh.

5.3.2.2. As-bearing Al-free and Al- ferrihydrites

The presence of As in ferrihydrite solids was confirmed by Raman spectroscopy and TEM. The Raman spectra for Al_RFh-As samples (Figure 5.6) show a broad peak centred at around 840 cm^{-1}, that is ascribed to the adsorbed As(V) (Müller et al. 2010). Indeed, this peak is not present in spectra of As-free Fh. No significant differences were observed when comparing the Raman spectra.

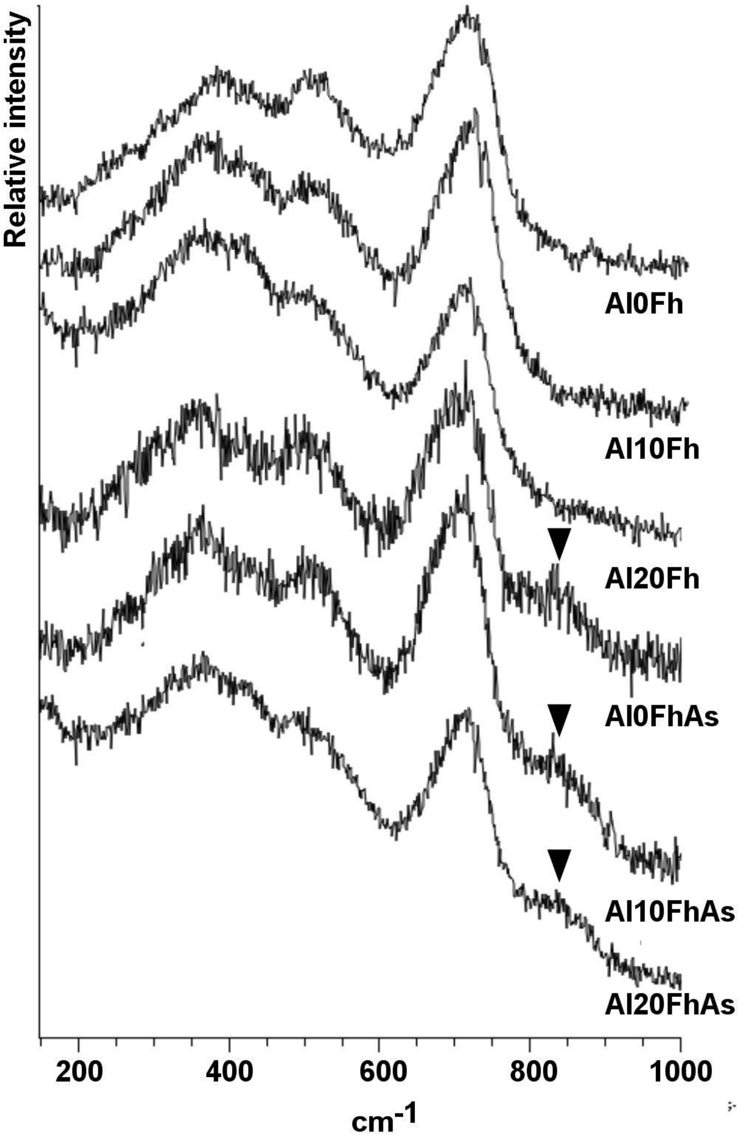

Figure 5.6. Raman spectra for As-free and As-adsorbed Al_RFh solids; R stands for the Al/(Al+Fe) molar ratio. The black arrows indicate the the As(V) peak centred at about 840 cm^{-1}.

The relative quantification from STEM-EDS analysis (Table 5.1) shows that Al/(Al+Fe) ratios are the same initial molar ratios (R) for almost all Fh precipitates, with the exception for sample precipitated with the highest amount of Al (R = 30%). The maximum Al-for-Fe substitution was 21 ± 4% mol mol^{-1}. This is consistent with Adra et al. (2016) who reported the maximum Al content in synthetic Fh as 22% mol mol^{-1}. The As/(Al+Fe) ratio was higher for Al_{30}Fh precipitates, nearly constant for $Al_{5,10,20}$Fh and slightly lower for Al_0Fh. The presence of adsorbed As(V) inhibited phase transformation in samples $Al_{0\text{-}10}$Fh-As during the course of the experiment. This is consistent with other studies (Das et al. 2011; Bolanz et al. 2013). However, As-bearing gibbsite was found in sample Al_{30}Fh-As from day 1 on, and at day 60 on, some gibbsite-like particles were identified in the sample Al_{20}Fh-As.

Table 5.1. Relative STEM-EDS quantification for Fh precipitates (only) with adsorbed As. The average values and standard deviations were determined from data in different measurements for each sample at different ageing times.

Sample	**O (wt%)**	**Fe (wt%)**	**Al (wt%)**	**As (wt%)**	**Al/(Al+Fe) (% mol mol^{-1})**	**As/(Al+Fe) (%mol mol^{-1})**
Al_0Fh-As	29.6 ± 0.1	65.0 ± 0.6		5.4 ± 0.6		0.062 ± 0.006
Al_5Fh-As	30.1 ± 0.1	62.6 ± 0.5	1.4 ± 0.1	5.8 ± 0.6	0.046 ± 0.003	0.066 ± 0.007
Al_{10}Fh-As	30.5 ± 0.1	60.7 ± 0.8	2.9 ± 0.3	5.8 ± 0.3	0.09 ± 0.01	0.065 ± 0.007
Al_{20}Fh-As	31.4 ± 0.2	57 ± 2	5.6 ± 0.8	6.1 ± 0.6	0.17 ± 0.02	0.066 ± 0.006
Al_{30}Fh-As	31.8 ± 0.4	54 ± 2	7 ± 1	6.9 ± 0.3	0.21 ± 0.04	0.075 ± 0.004

The TEM data provide evidences for a progressive aggregation of Fh towards mesocrystals (Figure 5.7). At day 1, we observed some As-adsorbed Fh NPs very close but not quite attached to each other (Figure 5.7.a). The nanoparticles aggregated upon attachment and formed a porous-like structure (Figures 5.7.b-c). From day 30 on we observed stripes of attached Fh NPs likely grown in [110] direction (Figure 5.7.c) and some Fh mesocrystals at day 120 (Figure 5.7.d). The presence of adsorbed As seems to have favoured the aggregation based crystal growth, differently from the pure Fh whose crystal products grew based on Ostwald ripening.

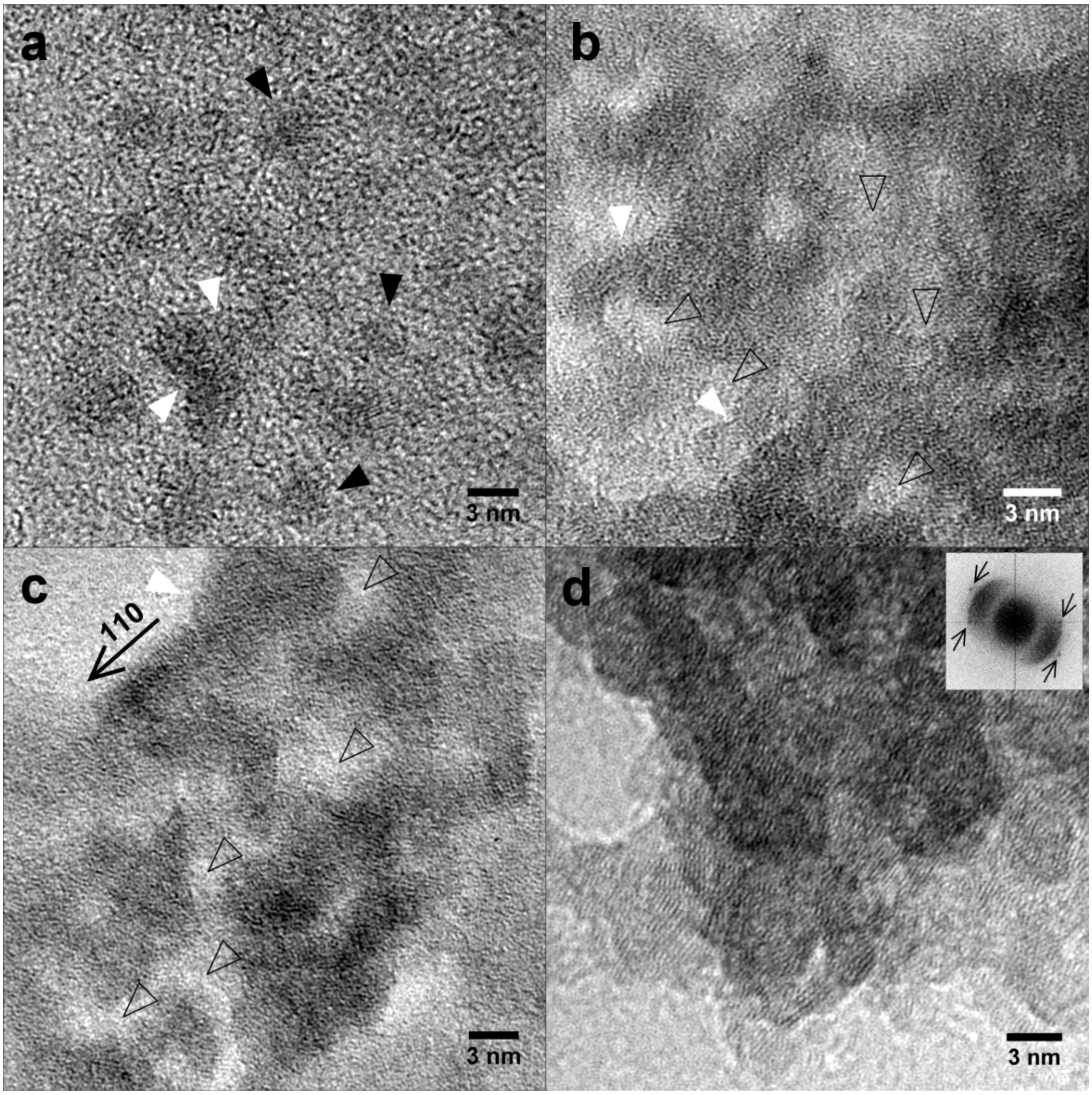

Figure 5.7. HRTEM images of Fh NPs in sample Al_0FhAs at day 1 (a), 15 (b), 30 (c) and 120 (d). The black arrows point some isolated As-adsorbed NPs and the white arrows some attached NPs (a-c). The outlined black arrows in (b-c) point some voids in between the stripes of NPs. The Fast Fourier Transform (FFT) in (d) shows the spots (pointed by arrows) corresponding to the lattice fringes of Fh mesocrystal shown in (d).

The EFTEM analysis shows the As(V) map in the Fh NPs' aggregate (Figure 5.8), predominantly surrounding the attached nanoparticles. The voids in between the NPs may provide a pathway to further soluble arsenic get into the porous-like structure and then adsorb onto available sites along the stripes of NPs. This highlights the inhibition of phase transformation from As(V)-adsorbed ferrihydrite towards goethite or hematite in our experiment, likely due the steric hindrance set up by adsorbed arsenic.

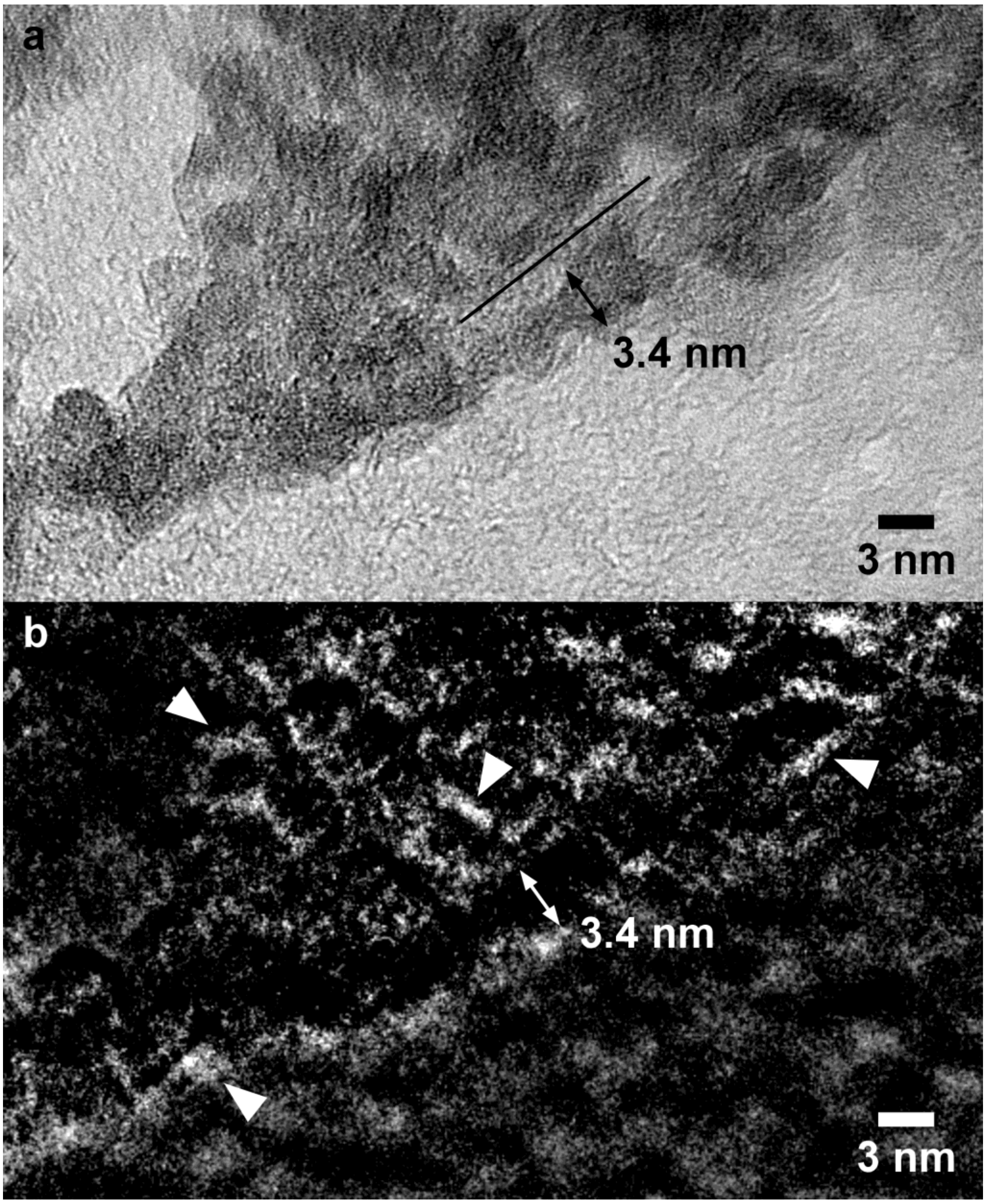

Figure 5.8. (a) HRTEM image of an aggregate of attached Fh NPs in sample Al_{10}Fh-As at day 60 (the direction of a stripe of NPs is indicate by the dark segment of line); (b) EFTEM image showing the EELS map for As M-edge performed in the same area shown in (a). The brighter areas, pointed by some arrows, show the As signal. The grey area outside the Fh NPs is due to signal from the background spectrum within the selected energy window to perform EFTEM mapping.

5.3.3. Mechanism of As immobilization in the nanostructured Al-Fe-(hydro)oxides

In this present work, large amounts of As(V) were adsorbed on Al-free and Al-ferrihydrite, and the arsenic content bound to solis increased gradually as samples aged. The Al-for-Fe substitution in ferrihydrite was shown to increase the average charge density surround Fe atoms, what may have contributed to strengthen the coulomb interaction between Fe adsorption sites and arsenate anions in solution. The solid phases analysis has shown the progressive oriented aggregation of As-adsorbed Fh NPs upon ageing, and the As distribution in between the oriented attached nanoparticles. These findings highlight and support a mechanism of (initially adsorbed) arsenic incorporation in nanocrystalline Al-Fe-(hydr)oxides, as depicted in Figure 5.9. Rather than adsorption or co-precipitation, this mechanism depends on the very nature of the samples and relies on a non-classical aggregation based crystal growth. The arsenic on the surface of primary nanoparticles of ferrihydrite, if not desorbed, can be irreversibly trapped upon attachment events of NPs. The self-assembly aggregation of ferrihydrite produces larger mesocrystals presenting a porous-like structure that can be a sink to adsorb further soluble arsenic. As the Fh mesocrystals would evolve to oriented aggregates upon ageing and thus undergo phase transformation, the primary adsorbed arsenic will ultimately be incorporated in the crystal products goethite or hematite.

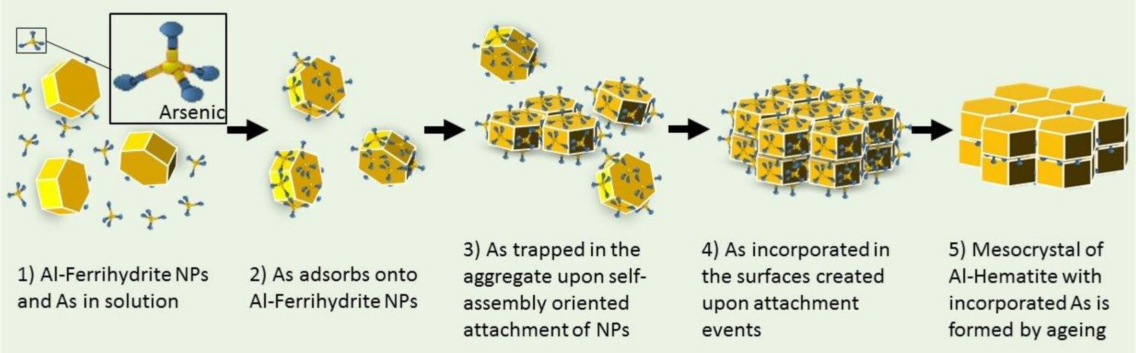

Figure 5.9. Schematic of the mechanism of As incorporation in nanostructured Al-Fe-(hydr)oxides

5.4. Conclusion

The mechanism of As incorporation into the nanostructured crystalline Al-containing Fe-(hydr)oxides have been proposed, and experimental evidences provided. The Al-for-Fe substitution in ferrhydrite promotes a displacement in the electronic density of Fe, virtually increasing the average charge density surrounding Fe atoms in the lattice. This effect may strengthen the electrostatic interaction between Fe sites and adsorbed As(V), or even compensate the charge balance to allow As get in to the lattice. This would need further investigations. Moreover, the presence of Al retards further crystallographic phase transformation, thus making Al-ferrihydrite more stable, what may contribute to the As stabilization in the host phase. The findings in this work deepen the understanding of long-term As immobilization in the crystalline bi-metal Al-Fe-(hydr)oxides, and may help the development of remediation technologies for As scavenging from contaminated water.

5.5. References

Adeleye, A. S., Conway, J. R., Garner, K., Huang, Y., Su, Y., Keller, A. A. (2016). Engineered Nanomaterials for Water Treatment and Remediation: Costs, Benefits, and Applicability. *Chem. Eng. J.* vol. 286: 640–662. DOI:10.1016/j.cej.2015.10.105.

Adra, A., Morin, G., Ona-Nguema, G., Brest, J. (2016). Arsenate and Arsenite Adsorption onto Al-Containing Ferrihydrites. Implications for Arsenic Immobilization After Neutralization of Acid Mine Drainage. *Appl. Geochemistry* vol. 64: 2–9. DOI: 10.1016/j.apgeochem.2015.09.015.

Adra, A., Morin, G., Ona-Nguema, G., Menguy, N., Maillot, F., Casiot, C., Bruneel, O., Lebrun, S., Juillot, F., Brest, J. (2013). Arsenic Scavenging by Aluminum-Substituted Ferrihydrites in a Circumneutral pH River Impacted by Acid Mine Drainage. *Environ. Sci. Technol.* vol. 47 (22): 12784–12792. DOI:10.1021/es4020234.

Akin, I., Arslan, G., Tor, A., Ersoz, M., Cengeloglu, Y. (2012). Arsenic(V) Removal from Underground Water by Magnetic Nanoparticles Synthesized from Waste Red Mud. *J. Hazard. Mater.* vol. 235–236: 62–68. DOI: 10.1016/j.jhazmat.2012.06.024.

Anderson, M. A., Ferguson, J. F., Gavis, J. (1976). Arsenate Adsorption on Amorphous Aluminum Hydroxide. *J. Colloid Interface Sci.* vol. 54 (3): 391–399.

Bolanz, R. M., Blass, U., Ackermann, S., Ciobota, V., Rosch, P., Tarcea, N., Popp, J., Majzlan, J. (2013). The Effect of Antimonate, Arsenate, and Phosphate on the Transformation of Ferrihydrite to Goethite, Hematite, Feroxyhyte, and Tripuhyite. *Clays Clay Miner.* vol. 61 (1): 11–25. DOI:10.1346/CCMN.2013.0610102.

Cao, C. Y., Qu, J., Yan, W. S., Zhu, J. F., Wu, Z. Y., Song, W. G. (2012). Low-Cost Synthesis of Flowerlike α-Fe 2O 3 Nanostructures for Heavy Metal Ion Removal: Adsorption Property and Mechanism. *Langmuir* vol. 28 (9): 4573–4579. DOI:10.1021/la300097y.

Carabante, I., Mouzon, J., Kumpiene, J., Gran, M., Fredriksson, A., Hedlund, J. (2014). Reutilization of Porous Sintered Hematite Bodies as E ff ective Adsorbents for Arsenic (V) Removal from Water. *Ind. Eng. Chem. Res*. vol. 53: 12689–12696.

Cliff, G., Lorimer, G. W. (1975). The Quantitative Analysis of Thin Specimens. *J. Microsc.* vol. 103 (2): 203–207. DOI:10.1111/j.1365-2818.1975.tb03895.x.

Cölfen, H., Antonietti, M. (2008). *Mesocrystals and Nonclassical Crystallization*. Chichester, England. John Wiley & Sons, Ltd.

Colliex, C., Manoubi, T., Ortiz, C. (1991). Electron-Energy-Loss-Spectroscopy near-Edge Fine Structures in the Iron-Oxygen System. *Phys. Rev. B* vol. 44 (20): 11402–11411.

Cornell, R.M., Schwertmann, U. (2003). *The Iron Oxides*: Structure, Properties, Reactions, Occurences and Uses. Second Edition. Weinheim, Germany: Wiley-VCH. DOI: 10.1002/3527602097.ch1.

Das, S., Hendry, M. J., Essil, J. (2011). Effects of Adsorbed Arsenate on the Rate of Transformation of 2-Line Ferrihydrite at pH 10 Soumya Das. *Environ. Sci. Technol*. vol. 45: 5557–5563.

Das, S., Essilfie-Dughan, J., Hendry, M. J. (2014). Arsenate Partitioning from Ferrihydrite to Hematite: Spectroscopic Evidence. *Am. Mineral.* vol. 99 (4): 749–754. DOI: 10.2138/am.2014.4657.

Egerton, R. F. (2008). Electron Energy-Loss Spectroscopy in the TEM. *Reports Prog. Phys*. vol. 72 (1): 016502. doi:10.1088/0034-4885/72/1/016502.

Feng, L., Cao, M., Ma, X., Zhu, Y., Hu, C. (2012). Superparamagnetic High-Surface-Area Fe3O4 Nanoparticles as Adsorbents for Arsenic Removal. *J. Hazard. Mater*. vol. 217–218: 439–446. DOI: 10.1016/j.jhazmat.2012.03.073.

Freitas, E. T. F., Montoro, L. A., Gasparon, M., Ciminelli, V. S. T. (2015). Natural Attenuation of Arsenic in the Environment by Immobilization in Nanostructured Hematite. *Chemosphere* vol. 138: 340–347. DOI: 10.1016/j.chemosphere.2015.05.101.

Freitas, E. T. F., Stroppa, D. G., Montoro, L. A., Mello, J. W. V., Gasparon, M., Ciminelli, V. S. T. (2016). Arsenic Entrapment by Nanocrystals of Al-Magnetite: The Role of Al in Crystal Growth and As Retention. *Chemosphere* vol. 158: 91–99. DOI: 10.1016/j.chemosphere.2016.05.044.

Hua, M., Zhang, S., Pan, B., Zhang, W., Lv, L., Zhang, Q. (2012). Heavy Metal Removal from Water/wastewater by Nanosized Metal Oxides: A Review. *J. Hazard. Mater*. vol. 211–212: 317–331. DOI: 10.1016/j.jhazmat.2011.10.016.

Jain, A., Raven, K. P., Loeppert, R. H. (1999). Arsenite and Arsenate Adsorption on Ferrihydrite: Surface Charge Reduction and Net OH- Release Stoichiometry. *Environ. Sci. Technol.* vol. 33 (8): 1179–1184. DOI: 10.1021/es980722e.

Ladeira, A. C. Q., Ciminelli, V. S. T. (2004). Adsorption and desorption of arsenic on an Oxisol and its constituents. Water Res. vol. 38 (8): 2087–2094. DOI: 10.1016/j.watres.2004.02.002.

Lata, S., Samadder, S. R. (2016). Removal of Arsenic from Water Using Nano Adsorbents and Challenges: A Review. J. Environ. Manage. vol. 166: 387–406. DOI: 10.1016/j.jenvman.2015.10.039.

Masue, Y., Loeppert, R. H., Kramer, T. A. (2007). Arsenate and Arsenite Adsorption and Desorption Behavior on Coprecipitated Aluminum:iron Hydroxides. Environ. Sci. Technol. vol. 41 (3): 837–842. DOI: 10.1021/es061160z.

Michel, F. M., Ehm, L., Antao, S. M., Lee, P. L., Chupas, P. L., Liu, G., Strongin, D. R., Schoonen, M. A. A., Phillips, B. L., Parise, J. B. (2007). The Structure of Ferrihydrite, a Nanocrystaline Material *Science* vol. 316: 1726–1729. DOI: 10.1126/science.1142525.

Mitchell, D. R. G, Schaffer, B. (2005). Scripting-Customised Microscopy Tools for Digital MicrographTM. *Ultramicroscopy* vol. 103 (4): 319–332. DOI: 10.1016/j.ultramic.2005.02.003.

Mitchell, D. R. G. (2008). DiffTools: Electron Diffraction Software Tools for DigitalMicrographTM. Microsc. Res. Tech. vol. 71 (8): 588–593. DOI: 10.1002/jemt.20591.

Müller, K., Ciminelli, V. S. T., Dantas, M. S. S., Willscher, S. (2010). A Comparative Study of As(III) and As(V) in Aqueous Solutions and Adsorbed on Iron Oxy-Hydroxides by Raman Spectroscopy. *Water Res.* vol. 44 (19): 5660–5672. DOI:

10.1016/j.watres.2010.05.053.

Pantuzzo, F. L., Ciminelli, V. S. T. (2010). Arsenic Association and Stability in Long-Term Disposed Arsenic Residues. *Water Res.* vol. 44 (19): 5631–5640. DOI: 10.1016/j.watres.2010.07.011.

Pantuzzo, F. L., Ciminelli, V. S. T., Brito, W. (2008). New Evidences for the Role of Precipitation and Adsorption during Fe(III)-As(V) Coprecipitation. In: Young, C.A., Taylor, P. R., Anderson, C. G. *Hydrometallurgy: Proceedings of the Sixth International Symposium*. Society for Mining, Metallurgy, and Exploration, Inc. Littleton, Colorado, USA. 130–139.

Penn, R. L. (2004). Kinetics of Oriented Aggregation. *J. Phys. Chem. B* vol. 108 (34): 12707–12712. DOI: 10.1021/jp036490.

Schwertmann, U., Cornell, R. M. (2000). *Iron Oxides in the Laboratory*. Second Edition. Weinheim, Germany. Wiley-VCH. DOI: 10.1180/minmag.1992.056.383.20.

Silva, J., Mello, J. W. V., Gasparon, M., Abrahao, W. A. P., Ciminelli, V. S. T., Jong, T. (2010). The Role of Al-Goethites on Arsenate Mobility. *Water Res*. vol. 44 (19): 5684–5692. DOI: 10.1016/j.watres.2010.06.056.

Smedley, P. L., Kinniburgh, D. G. (2002). A Review of the Source, Behaviour and Distribution of Arsenic in Natural Waters. *Appl. Geochemistry* vol. 17 (5): 517–568. DOI: 10.1016/S0883-2927(02)00018-5.

Smith, E., Naidu, R., Alston, A. M., Donald, L. S. (1998). Arsenic in the Soil Environment: A Review. *Adv. Agron.* vol. 64: 149–195. DOI: 10.1016/S0065-2113(08)60504-0.

Tan, H., Verbeeck, J., Abakumov, A., Van Tendeloo, G. (2012). Oxidation State and Chemical Shift Investigation in Transition Metal Oxides by EELS. *Ultramicroscopy* vol. 116: 24–33. DOI: 10.1016/j.ultramic.2012.03.002.

Tang, W., Li, Q., Gao, S., Shang, J. K. (2011). Arsenic (III, V) Removal from Aqueous Solution by Ultrafine α-Fe2O3 Nanoparticles Synthesized from Solvent Thermal Method. *J. Hazard. Mater.* vol. 192 (1): 131–138. DOI: 10.1016/j.jhazmat.2011.04.111.

Violante, A., Gaudio, S. D., Pigna, M., Ricciardella, M., Banerjee, D. (2007). Coprecipitation of Arsenate with Metal Oxides. 2. Nature, Mineralogy, and

Reactivity of Iron (III)-Alulminum Precipitates. *Environ. Sci. Technol*. vol. 41 (3): 8275–8280.

Yuwono, V. M., Burrows, N. D., Soltis, J. A., Do, T. A., Penn, R. L. (2012). Aggregation of Ferrihydrite Nanoparticles in Aqueous Systems." *Faraday Discuss.* vol. 159: 235. DOI: 10.1039/c2fd20115a.

Zhang, H., Banfield, J. F. (2012). Energy Calculations Predict Nanoparticle Attachment Orientations and Asymmetric Crystal Formation. *J. Phys. Chem. Lett*. vol. 3: 2882. DOI: 10.1021/jz301161j.

CHAPTER 6. Final considerations

6.1. Overal conclusions

The arsenic incorporation in nanostructured crystalline Al-Fe-(hydr)oxides was shown for different crystallographic phases found in both environmental and synthetic samples. Direct and indirect experimental supporting evidences are provided. This mechanism relies on the aggregation based crystal growth of As-adsorbed nanoparticles and is described as follows: The Al-Fe-(hydr)oxides' nanoparticles formed in soluble media adsorb arsenic in solution, and have their surface energy changed. Initially, the nanoparticles undergo oriented attachment along the crystal facets with highest energies to reduce the total energy of the system. Following, further attachment takes place in other directions and large mesocrystals start to form. This mesocrystals present a porous-like structure formed by the voids in between the attached nanoparticles that can be a sink for further aqueous arsenic. As the nanoparticles aggregate, the initially adsorbed As is trapped upon attachment events. If not desorbed, the arsenic is irreversibly incorporated in the net structure when the mesocrystals evolve to oriented aggregates and ultimately to other stable, end phases goethite and hematite.

The presence of Al, or adsorbed As, in the Fe-(hydr)oxides hinders the crystal growth of the primary formed nanoparticles. This effect contributes to keep the system in the oriented aggregation regime. The presence of substituted Al in Fe-(hydr)oxides can also promote a displacement in the electronic density of Fe, virtually changing the average charge density around Fe atoms in the crystal lattice as shown for Al-ferrihydrite. The increased As adsorption onto Al-Fe-(hydr)oxides relative to pure Fe-(hydr)oxides may be due to the stronger coulomb interaction between the Fe sorption sites and the oxyanions in solution. The presence of Al also retards phase transformation, thus stabilizing the formed Al-ferrihydrite.

This mechanism of As incorporation in the crystalline Al-Fe-(hydr)oxides accounts for and highlights the long-term As immobilization in both environmental and synthetic samples studied in this research. The findings reported here contribute to deepen the understanding of As partitionining during crystallographic phase transformation upon ageing at ambient temperature. At certain extent, this mechanism may be responsible for the uptake and sequestration of existent contaminat metalloids in soils which undergo weathering processes in the environment. Indeed, soil-Al-containig-Fe-(hydr)oxides are often nanostructured. In addition, the findings reported in the present work can help in the development of remediation technologies for efficient As fixation, and for the post-treatment of contaminated water and acid mine drainage water.

6.2. Original contributions from this Thesis

The findings reported in this work contribute to deepen the understanding of the arsenic immobilization process in crystalline Al-bearing Fe-(hydr)oxides in both natural and synthetic samples. The nature of these As-bearing nanostructured phases was investigated by high spatial resolution image, diffraction and spectroscopy analyses. The direct evidences that support the proposed mechanism of As incorporation in these nanostructured phases were shown here for the first time. In addition, the application of transmission electron microscopy techniques was shown to be successful and feasible to the analysis and characterization of trace-elements-containing heterogeneous solid phases.

6.3. Publications

i) Freitas, E. T. F., Montoro, L. A., Gasparon, M., Ciminelli, V. S. T. (2015). **Natural attenuation of arsenic in the environment by immobilization in nanostructured hematite**. *Chemosphere* vol. 138: 340–347. DOI: 10.1016/j.chemosphere.2015.05.101.

ii) Freitas, E. T. F., Stroppa, D. G., Montoro, L. A., Mello, J. W. V., Gasparon, M., Ciminelli, V. S. T. (2016). **Arsenic entrapment by nanocrystals of al-magnetite: the role of Al in crystal growth and as retention**. *Chemosphere* vol. 158: 91–99. DOI: 10.1016/j.chemosphere.2016.05.044.

iii) Ciminelli, V. S. T., Freitas, E. T. F.; Montoro, L. A., Mello, J. W. V.; Gasparon, M. (2016). **New insights in the mechanisms of arsenic association with iron oxides in the environment**. In: *6th International Congress on Arsenic in the Environment (As2016),* Stockholm. Arsenic Research and Global Sustainability.

iv) "The fate of adsorbed arsenic onto pure and aluminous ferrihydrite"

- Authors: Erico T. F. Freitas, Claudia L. Caldeira, Maria S. S. Dantas, Luciano A. Montoro, Hélio A. Duarte, Massimo Gasparon, Virginia S. T. Ciminelli.
- Manuscript in preparation.

v) "Transmission electron microscopy techniques applied to the characterization of environmental and synthetic samples"

- Authors: Erico T. F. Freitas, Virgínia S. T. Ciminelli
- Manuscript to be submitted

vi) Freitas, E. T. F., Montoro, L. A., Mello, J. W. V., Gasparon, M., Ciminelli, V. S. T. (2016). **Role of Al-Fe-(hydr)oxides on mobility and bioavailability of contaminants. Part 1: mechanism or arsenic fixation**. *Activity Report* 2013-2016. National Institute of Science and Technology on Mineral Resources, Water and Biodiversity (INCT-Acqua), Belo Horizonte, 64-66.

vii) Freitas, E. T. F. (2014). **Refinement of lattice parameter of hematite by nano-beam electron diffraction**. In: *18th International Miroscopy Congress,* Praga. Proceedings. Czecchoslovak Microscopy Society

viii) Freitas, E. T. F., Silva, G. C., Ciminelli, V. S. T. (2013). **Phase characterization by nano-beam electron diffraction of enriched Al and Fe Oxisols containing arsenic**. In: *XXIV Congresso da Sociedade Brasileira de Microscopia e Microanálise.* Caxambu. Anais.

6.4. Contributions to additional publications

i) Ciminelli, V. S. T., Antônio, D. C., Caldeira, C. L., Gasparon, M., Ng, J., Freitas, E. T. F., Delbem, I. D., Fernandes, M. M. (2017). Low Arsenic Bioaccessibility by Fixation in Nanostructured Iron (Hydr)-Oxides: A Quantitative Identification of As-Bearing Phases. Manuscript submitted.

ii) Morais, M., Ng, J., Gasparon, M., Freitas, E. T. F., Delbem, I. D., Ciminelli, V. S. T. (2017). Lung bioaccessibility combined with quantification of As–bearing phases in fine surface dust in a gold mining district. Manuscript in preparation

6.5. Suggestion for future works

The findings in this research point out some possibilities for future investigations. Some additional questions arise regarding the actual role of aluminium in the process of arsenic uptake by bi-metal aluminium and iron (hydr)oxides, and the arsenic partitioning during phase transformation upon ageing at ambient temperature. The research themes and main quantions are listed below.

i) Investigation of the actual effect of Al-for-Fe substitution in the electronic density of Fe atoms in crystalline Fe-(hydr)oxides and on surface energy changing by combining high spatial and energy resolution sensitive spectroscopy techniques (Raman, XPS and EELS) with theoretical modelling.
ii) Does the Fe electronic density increase by Al-for-Fe substitution in the lattice?
iii) At which extent does the lattice potential is changed by Al-for-Fe substitution?
iv) Will Al-for-Fe substitution change the surface energy of the nanocrystal compound?

v) Evaluation of the fate of adsorbed and co-precipitated As during phase transformation of nanostructured Al-Fe-(hydr)oxides.

vi) Is the mechanism of As incorporation in nanostructured Al-Fe-(hydr)oxides pH dependent?

vii) Will some aluminium be resolubilised upon phase transformation in aqueous media?

viii) Will some arsenic be mobilised upon phase transformation?

APPENDICES

Appendix 1. Refinement of lattice parameters

Prior the refinement of lattice parameters, the distortion coefficients C_{radial}, C_{spiral}, and $C_{ellipticala}$ of image-forming lens system of the TEM were determined after Saitoh et al. (2013; See reference in Chapter 3). A standard single crystal of Si (*F*d-3m, *a* = 5.4309 nm) were used for the distortion coefficients measurements. The experimental nano-beam electron diffraction pattern (NBDP) of Si along the <111> zone axis (ZA) was indexed and compared with the simulated NBDP (Figure A1). The indexation and simulated pattern were performed with the help of JEMS software.

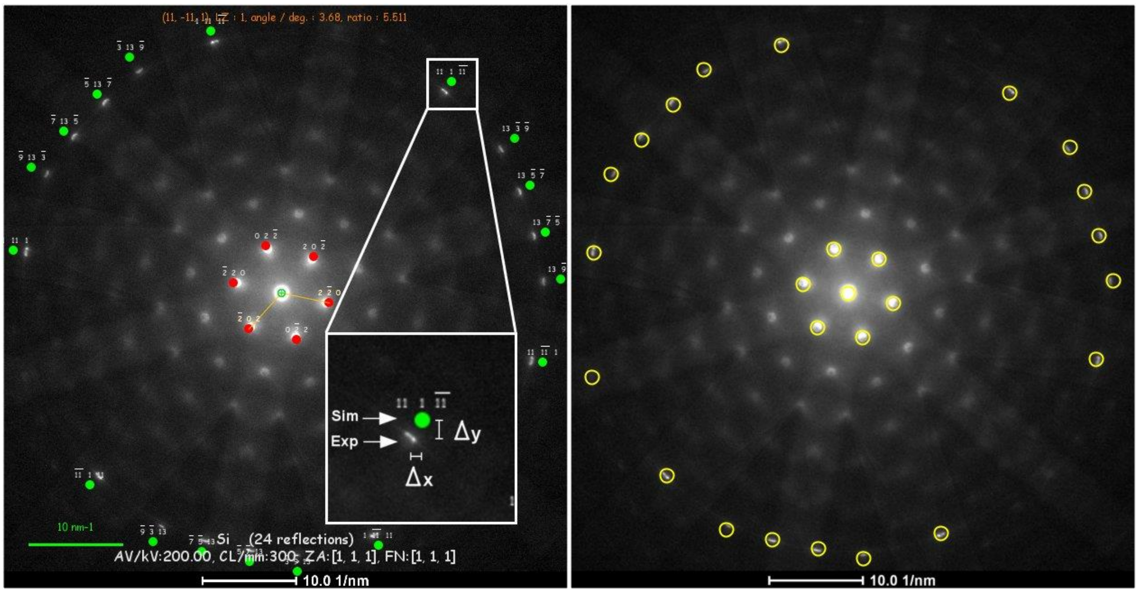

Figure A.1. NBDP patterns of the standard Si sample along the <111> ZA, taken at a camera length of 300 mm. At left, the NBDP showing the experimental (Exp) the correspondent simulated (Sim) reflection *hkl* positions. At right, the same experimental NBDP with the corrected *hkl* reflection positions centrered at the overlaid yellow circles.

The experimental and simulated (indexed) *i*-th reflection positions (x_i^{exp}, y_i^{exp}) and (x_i^{sim}, y_i^{sim}), respectively, were measured in pixel units after the scale bar had been set. A total of 25 *hlk* reflections were used, as indicated in Figure A.1. The displacements (Δx_i, Δy_i) for each *i*-th reclection were calculated by using the equation 3.1 (See Section 3.2.4). The distortion coefficients were determined by fitting the reflection positions between the experimental and simulated NBDPs, using the equation 3.2 (See Section 3.2.4), until the minimum *chi*-square (X^2) value had been reached. The corrected reflection positions overlaid in Figure A1 (at right) gives an ideia of the excellent fitting. All the calculated values are shown in the Excel sheet (Figure A.2).

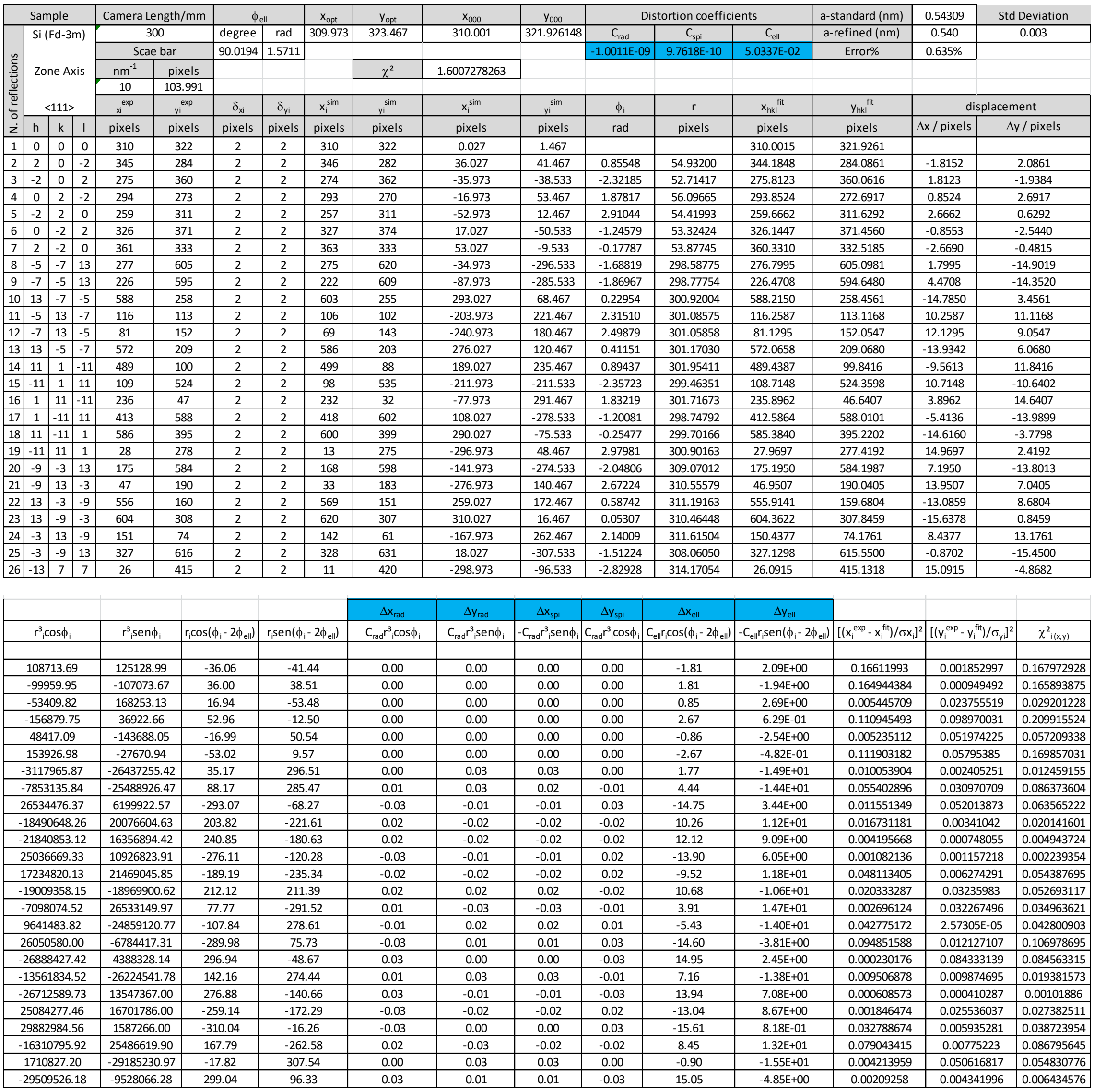

Sample				Camera Length/mm		ϕ_{ell}		x_{opt}	y_{opt}	x_{000}	y_{000}	Distortion coefficients			a-standard (nm)	0.54309	Std Deviation
N. of reflections	Si (Fd-3m)			300		degree	rad	309.973	323.467	310.001	321.926148	C_{rad}	C_{spi}	C_{ell}	a-refined (nm)	0.540	0.003
				Scae bar		90.0194	1.5711					-1.0011E-09	9.7618E-10	5.0337E-02	Error%	0.635%	
	Zone Axis			nm^{-1}	pixels				χ^2	1.6007278263							
				10	103.991												
	<111>			x_i^{exp}	y_i^{exp}	δ_{xi}	δ_{yi}	x_i^{sim}	y_i^{sim}	x_i^{sim}	y_i^{sim}	ϕ_i	r	x_{hkl}^{fit}	y_{hkl}^{fit}	displacement	
	h	k	l	pixels	pixels	pixels	pixels	pixels	pixels	pixels	pixels	rad	pixels	pixels	pixels	Δx / pixels	Δy / pixels
1	0	0	0	310	322	2	2	310	322	0.027	1.467			310.0015	321.9261		
2	2	0	-2	345	284	2	2	346	282	36.027	41.467	0.85548	54.93200	344.1848	284.0861	-1.8152	2.0861
3	-2	0	2	275	360	2	2	274	362	-35.973	-38.533	-2.32185	52.71417	275.8123	360.0616	1.8123	-1.9384
4	0	2	-2	294	273	2	2	293	270	-16.973	53.467	1.87817	56.09665	293.8524	272.6917	0.8524	2.6917
5	-2	2	0	259	311	2	2	257	311	-52.973	12.467	2.91044	54.41993	259.6662	311.6292	2.6662	0.6292
6	0	-2	2	326	371	2	2	327	374	17.027	-50.533	-1.24579	53.32424	326.1447	371.4560	-0.8553	-2.5440
7	2	-2	0	361	333	2	2	363	333	53.027	-9.533	-0.17787	53.87745	360.3310	332.5185	-2.6690	-0.4815
8	-5	-7	13	277	605	2	2	275	620	-34.973	-296.533	-1.68819	298.58775	276.7995	605.0981	1.7995	-14.9019
9	-7	-5	13	226	595	2	2	222	609	-87.973	-285.533	-1.86967	298.77754	226.4708	594.6480	4.4708	-14.3520
10	13	-7	-5	588	258	2	2	603	255	293.027	68.467	0.22954	300.92004	588.2150	258.4561	-14.7850	3.4561
11	-5	13	-7	116	113	2	2	106	102	-203.973	221.467	2.31510	301.08575	116.2587	113.1168	10.2587	11.1168
12	-7	13	-5	81	152	2	2	69	143	-240.973	180.467	2.49879	301.05858	81.1295	152.0547	12.1295	9.0547
13	13	-5	-7	572	209	2	2	586	203	276.027	120.467	0.41151	301.17030	572.0658	209.0680	-13.9342	6.0680
14	11	1	-11	489	100	2	2	499	88	189.027	235.467	0.89437	301.95411	489.4387	99.8416	-9.5613	11.8416
15	-11	1	11	109	524	2	2	98	535	-211.973	-211.533	-2.35723	299.46351	108.7148	524.3598	10.7148	-10.6402
16	1	11	-11	236	47	2	2	232	32	-77.973	291.467	1.83219	301.71673	235.8962	46.6407	3.8962	14.6407
17	1	-11	11	413	588	2	2	418	602	108.027	-278.533	-1.20081	298.74792	412.5864	588.0101	-5.4136	-13.9899
18	11	-11	1	586	395	2	2	600	399	290.027	-75.533	-0.25477	299.70166	585.3840	395.2202	-14.6160	-3.7798
19	-11	11	1	28	278	2	2	13	275	-296.973	48.467	2.97981	300.90163	27.9697	277.4192	14.9697	2.4192
20	-9	-3	13	175	584	2	2	168	598	-141.973	-274.533	-2.04806	309.07012	175.1950	584.1987	7.1950	-13.8013
21	-9	13	-3	47	190	2	2	33	183	-276.973	140.467	2.67224	310.55579	46.9507	190.0405	13.9507	7.0405
22	13	-3	-9	556	160	2	2	569	151	259.027	172.467	0.58742	311.19163	555.9141	159.6804	-13.0859	8.6804
23	13	-9	-3	604	308	2	2	620	307	310.027	16.467	0.05307	310.46448	604.3622	307.8459	-15.6378	0.8459
24	-3	13	-9	151	74	2	2	142	61	-167.973	262.467	2.14009	311.61504	150.4377	74.1761	8.4377	13.1761
25	-3	-9	13	327	616	2	2	328	631	18.027	-307.533	-1.51224	308.06050	327.1298	615.5500	-0.8702	-15.4500
26	-13	7	7	26	415	2	2	11	420	-298.973	-96.533	-2.82928	314.17054	26.0915	415.1318	15.0915	-4.8682

				Δx_{rad}	Δy_{rad}	Δx_{spi}	Δy_{spi}	Δx_{ell}	Δy_{ell}			
$r^3_i\cos\phi_i$	$r^3_i\mathrm{sen}\phi_i$	$r_i\cos(\phi_i - 2\phi_{ell})$	$r_i\mathrm{sen}(\phi_i - 2\phi_{ell})$	$C_{rad}r^3_i\cos\phi_i$	$C_{rad}r^3_i\mathrm{sen}\phi_i$	$-C_{rad}r^3_i\mathrm{sen}\phi_i$	$C_{rad}r^3_i\cos\phi_i$	$C_{ell}r_i\cos(\phi_i - 2\phi_{ell})$	$-C_{ell}r_i\mathrm{sen}(\phi_i - 2\phi_{ell})$	$[(x_i^{exp} - x_i^{fit})/\sigma x_i]^2$	$[(y_i^{exp} - y_i^{fit})/\sigma_{yi}]^2$	$\chi^2_{i\,(x,y)}$
108713.69	125128.99	-36.06	-41.44	0.00	0.00	0.00	0.00	-1.81	2.09E+00	0.16611993	0.001852997	0.167972928
-99959.95	-107073.67	36.00	38.51	0.00	0.00	0.00	0.00	1.81	-1.94E+00	0.164944384	0.000949492	0.165893875
-53409.82	168253.13	16.94	-53.48	0.00	0.00	0.00	0.00	0.85	2.69E+00	0.005445709	0.023755519	0.029201228
-156879.75	36922.66	52.96	-12.50	0.00	0.00	0.00	0.00	2.67	6.29E-01	0.110945493	0.098970031	0.209915524
48417.09	-143688.05	-16.99	50.54	0.00	0.00	0.00	0.00	-0.86	-2.54E+00	0.005235112	0.051974225	0.057209338
153926.98	-27670.94	-53.02	9.57	0.00	0.00	0.00	0.00	-2.67	-4.82E-01	0.111903182	0.05795385	0.169857031
-3117965.87	-26437255.42	35.17	296.51	0.00	0.03	0.03	0.00	1.77	-1.49E+01	0.010053904	0.002405251	0.012459155
-7853135.84	-25488926.47	88.17	285.47	0.01	0.03	0.02	-0.01	4.44	-1.44E+01	0.055402896	0.030970709	0.086373604
26534476.37	6199922.57	-293.07	-68.27	-0.03	-0.01	-0.01	0.03	-14.75	3.44E+00	0.011551349	0.052013873	0.063565222
-18490648.26	20076604.63	203.82	-221.61	0.02	-0.02	-0.02	-0.02	10.26	1.12E+01	0.016731181	0.00341042	0.020141601
-21840853.12	16356894.42	240.85	-180.63	0.02	-0.02	-0.02	-0.02	12.12	9.09E+00	0.004195668	0.000748055	0.004943724
25036669.33	10926823.91	-276.11	-120.28	-0.03	-0.01	-0.01	0.02	-13.90	6.05E+00	0.001082136	0.001157218	0.002239354
17234820.13	21469045.85	-189.19	-235.34	-0.02	-0.02	-0.02	0.02	-9.52	1.18E+01	0.048113405	0.006274291	0.054387695
-19009358.15	-18969900.62	212.12	211.39	0.02	0.02	0.02	-0.02	10.68	-1.06E+01	0.020333287	0.03235983	0.052693117
-7098074.52	26533149.97	77.77	-291.52	0.01	-0.03	-0.03	-0.01	3.91	1.47E+01	0.002696124	0.032267496	0.034963621
9641483.82	-24859120.77	-107.84	278.61	-0.01	0.02	0.02	0.01	-5.43	-1.40E+01	0.042775172	2.57305E-05	0.042800903
26050580.00	-6784417.31	-289.98	75.73	-0.03	0.01	0.01	0.03	-14.60	-3.81E+00	0.094851588	0.012127107	0.106978695
-26888427.42	4388328.14	296.94	-48.67	0.03	0.00	0.00	-0.03	14.95	2.45E+00	0.000230176	0.084333139	0.084563315
-13561834.52	-26224541.78	142.16	274.44	0.01	0.03	0.03	-0.01	7.16	-1.38E+01	0.009506878	0.009874695	0.019381573
-26712589.73	13547367.00	276.88	-140.66	0.03	-0.01	-0.01	-0.03	13.94	7.08E+00	0.000608573	0.000410287	0.00101886
25084277.46	16701786.00	-259.14	-172.29	-0.03	-0.02	-0.02	0.02	-13.04	8.67E+00	0.001846474	0.025536037	0.027382511
29882984.56	1587266.00	-310.04	-16.26	-0.03	0.00	0.00	0.03	-15.61	8.18E-01	0.032788674	0.005935281	0.038723954
-16310795.92	25486619.90	167.79	-262.58	0.02	-0.03	-0.02	-0.02	8.45	1.32E+01	0.079043415	0.00775223	0.086795645
1710827.20	-29185230.97	-17.82	307.54	0.00	0.03	0.03	0.00	-0.90	-1.55E+01	0.004213959	0.050616817	0.054830776
-29509526.18	-9528066.28	299.04	96.33	0.03	0.01	0.01	-0.03	15.05	-4.85E+00	0.00209258	0.004341996	0.006434576

Figure A.2. Excel sheet for the calculation of the distortion coefficients C_{rad}, C_{spi}, and C_{ell} after Saitoh et al. (2013) for an standard single crystal of Si (*F*d-3m, *a* = 5.4309 nm), along <111> ZA.

For each *i*-th corrected *hlk* refection position, the lattice parameter "a_i" for the Si was determined after the Equation A.1:

$$a_i = \left(d_{hkl}\sqrt{h^2 + k^2 + l^2}\right)^{1/2} \qquad \text{(Eq. A.1)}$$

The refined lattice parameter "a_{Ref}" was taken as the average over all the calculated a_i values. The presicion of the lattice parameter refinement, in terms of error % was considered as the coefficient of variation, i.e. the ratio of the standard deviation to the averaged valeu of the lattice parameter. For the Si sample, the determined a_{Ref} value (0.540 ± 0.003 nm) is in excellent agreement with the standard value (a_{Std} = 0.54309 nm). The precision in the refinement was 0.635% error.

After the distortion coefficients have been determined, they were applied to the refinement of the lattice parameters for the Al-hematite samples found in Oxisol liners (OL) samples OL1 and OL3. The results are shown in Section 3.3.2. Figure A.3 shows the simulated and experimental NBDPs for hematite along the [301] ZA, in sample OL1, as well as the overlaid 52 corrected reflection positions using for the refinement of the lattice parameter.

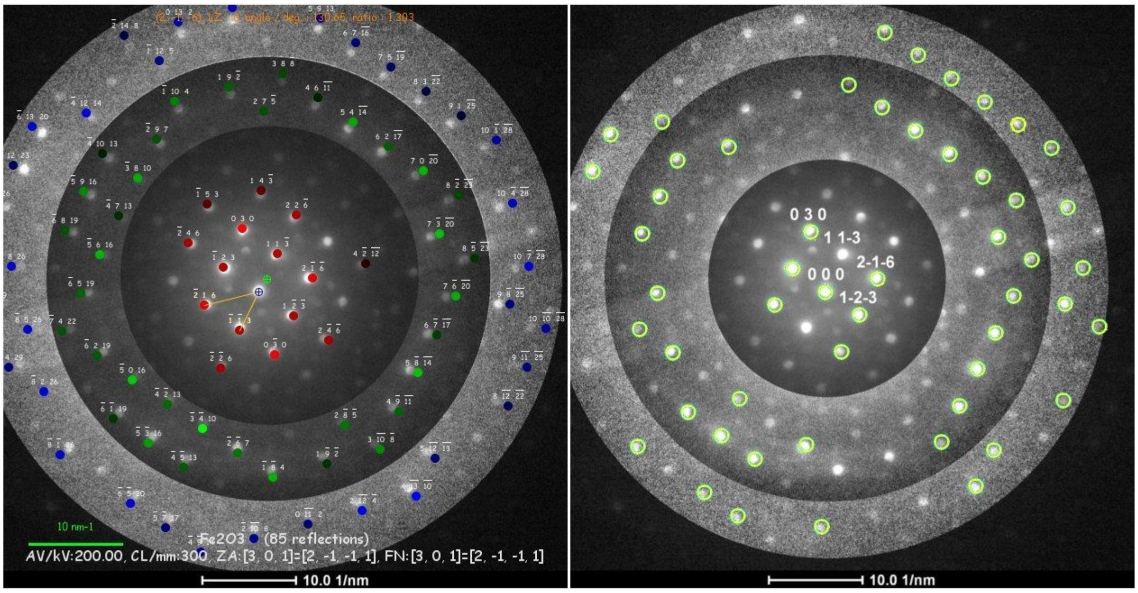

Figure A.3. NBDP patterns of the Al-hematite along [301] ZA, in sample OL1, taken at a camera length of 300 mm. At left, the NBDP showing the experimental (Exp) the correspondent simulated (Sim) *hkl* reflection positions. At right, the same experimental NBDP with the corrected *hkl* reflection positions centrered at the overlaid yellow circles.

Figure A.4 shows the Excel sheet for the calculations of the fitted *hkl* reflection positions used for the lattice parameters refinement. For simplicity, other parts of the Excel sheet that would show the detailed calculated values for each individual contribution to the displacements ($\Delta x,y_{\text{radial}}$, $\Delta x,y_{\text{spiral}}$, and $\Delta x,y_{\text{eliptical}}$) are omitted.

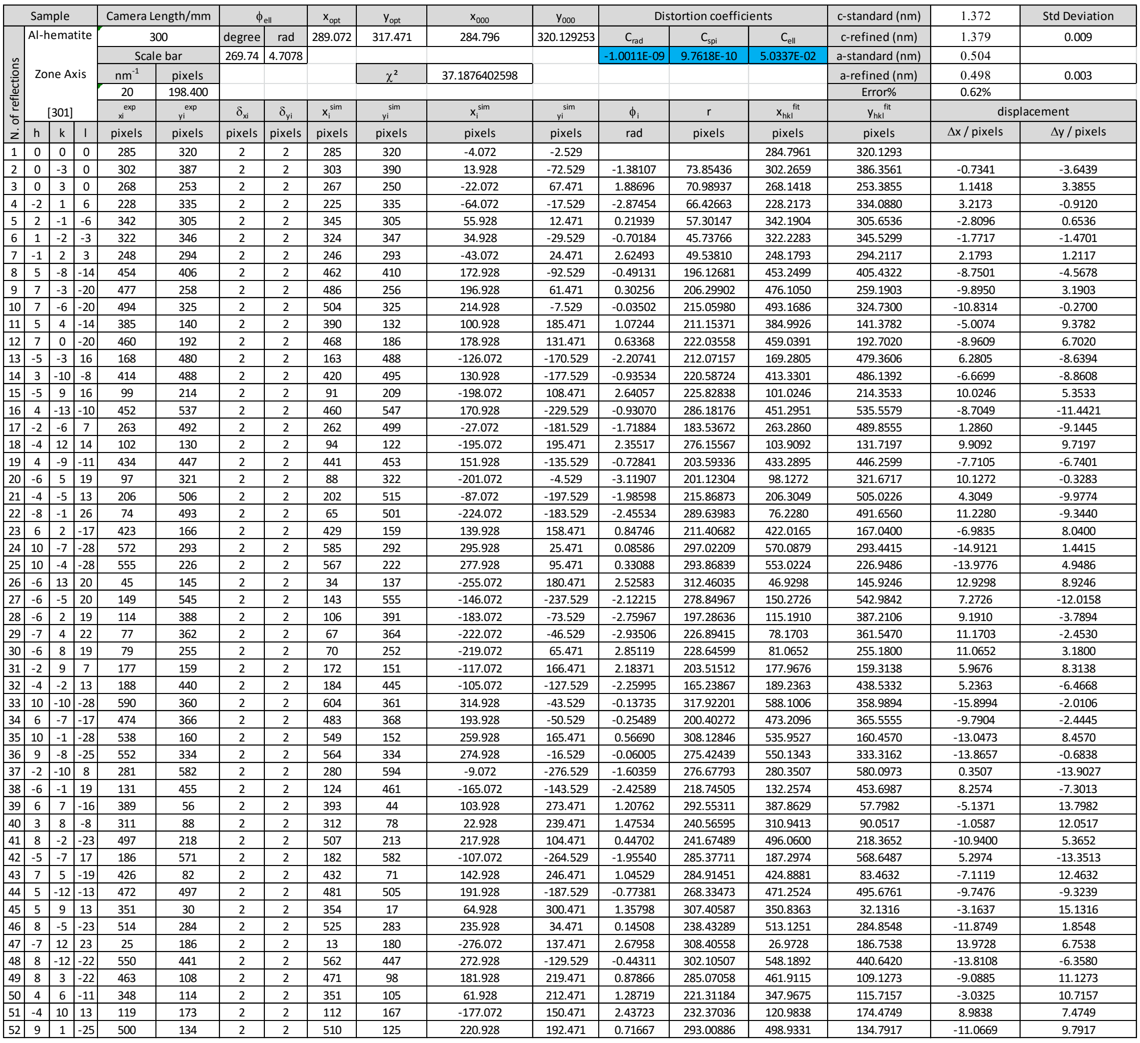

Sample				Camera Length/mm		ϕ_{ell}		x_{opt}	y_{opt}	x_{000}	y_{000}	Distortion coefficients			c-standard (nm)	1.372	Std Deviation
N. of reflections	Al-hematite			300		degree	rad	289.072	317.471	284.796	320.129253	C_{rad}	C_{spi}	C_{ell}	c-refined (nm)	1.379	0.009
				Scale bar		269.74	4.7078					-1.0011E-09	9.7618E-10	5.0337E-02	a-standard (nm)	0.504	
	Zone Axis			nm^{-1}	pixels				χ^2	37.1876402598					a-refined (nm)	0.498	0.003
				20	198.400										Error%	0.62%	
	[301]			$^{exp}_{xi}$	$^{exp}_{yi}$	δ_{xi}	δ_{yi}	x_i^{sim}	$^{sim}_{yi}$	x_i^{sim}	$^{sim}_{yi}$	ϕ_i	r	x_{hkl}^{fit}	y_{hkl}^{fit}	displacement	
	h	k	l	pixels	pixels	pixels	pixels	pixels	pixels	pixels	pixels	rad	pixels	pixels	pixels	Δx / pixels	Δy / pixels
1	0	0	0	285	320	2	2	285	320	-4.072	-2.529			284.7961	320.1293		
2	0	-3	0	302	387	2	2	303	390	13.928	-72.529	-1.38107	73.85436	302.2659	386.3561	-0.7341	-3.6439
3	0	3	0	268	253	2	2	267	250	-22.072	67.471	1.88696	70.98937	268.1418	253.3855	1.1418	3.3855
4	-2	1	6	228	335	2	2	225	335	-64.072	-17.529	-2.87454	66.42663	228.2173	334.0880	3.2173	-0.9120
5	2	-1	-6	342	305	2	2	345	305	55.928	12.471	0.21939	57.30147	342.1904	305.6536	-2.8096	0.6536
6	1	-2	-3	322	346	2	2	324	347	34.928	-29.529	-0.70184	45.73766	322.2283	345.5299	-1.7717	-1.4701
7	-1	2	3	248	294	2	2	246	293	-43.072	24.471	2.62493	49.53810	248.1793	294.2117	2.1793	1.2117
8	5	-8	-14	454	406	2	2	462	410	172.928	-92.529	-0.49131	196.12681	453.2499	405.4322	-8.7501	-4.5678
9	7	-3	-20	477	258	2	2	486	256	196.928	61.471	0.30256	206.29902	476.1050	259.1903	-9.8950	3.1903
10	7	-6	-20	494	325	2	2	504	325	214.928	-7.529	-0.03502	215.05980	493.1686	324.7300	-10.8314	-0.2700
11	5	4	-14	385	140	2	2	390	132	100.928	185.471	1.07244	211.15371	384.9926	141.3782	-5.0074	9.3782
12	7	0	-20	460	192	2	2	468	186	178.928	131.471	0.63368	222.03558	459.0391	192.7020	-8.9609	6.7020
13	-5	-3	16	168	480	2	2	163	488	-126.072	-170.529	-2.20741	212.07157	169.2805	479.3606	6.2805	-8.6394
14	3	-10	-8	414	488	2	2	420	495	130.928	-177.529	-0.93534	220.58724	413.3301	486.1392	-6.6699	-8.8608
15	-5	9	16	99	214	2	2	91	209	-198.072	108.471	2.64057	225.82838	101.0246	214.3533	10.0246	5.3533
16	4	-13	-10	452	537	2	2	460	547	170.928	-229.529	-0.93070	286.18176	451.2951	535.5579	-8.7049	-11.4421
17	-2	-6	7	263	492	2	2	262	499	-27.072	-181.529	-1.71884	183.53672	263.2860	489.8555	1.2860	-9.1445
18	-4	12	14	102	130	2	2	94	122	-195.072	195.471	2.35517	276.15567	103.9092	131.7197	9.9092	9.7197
19	4	-9	-11	434	447	2	2	441	453	151.928	-135.529	-0.72841	203.59336	433.2895	446.2599	-7.7105	-6.7401
20	-6	5	19	97	321	2	2	88	322	-201.072	-4.529	-3.11907	201.12304	98.1272	321.6717	10.1272	-0.3283
21	-4	-5	13	206	506	2	2	202	515	-87.072	-197.529	-1.98598	215.86873	206.3049	505.0226	4.3049	-9.9774
22	-8	-1	26	74	493	2	2	65	501	-224.072	-183.529	-2.45534	289.63983	76.2280	491.6560	11.2280	-9.3440
23	6	2	-17	423	166	2	2	429	159	139.928	158.471	0.84746	211.40682	422.0165	167.0400	-6.9835	8.0400
24	10	-7	-28	572	293	2	2	585	292	295.928	25.471	0.08586	297.02209	570.0879	293.4415	-14.9121	1.4415
25	10	-4	-28	555	226	2	2	567	222	277.928	95.471	0.33088	293.86839	553.0224	226.9486	-13.9776	4.9486
26	-6	13	20	45	145	2	2	34	137	-255.072	180.471	2.52583	312.46035	46.9298	145.9246	12.9298	8.9246
27	-6	-5	20	149	545	2	2	143	555	-146.072	-237.529	-2.12215	278.84967	150.2726	542.9842	7.2726	-12.0158
28	-6	2	19	114	388	2	2	106	391	-183.072	-73.529	-2.75967	197.28636	115.1910	387.2106	9.1910	-3.7894
29	-7	4	22	77	362	2	2	67	364	-222.072	-46.529	-2.93506	226.89415	78.1703	361.5470	11.1703	-2.4530
30	-6	8	19	79	255	2	2	70	252	-219.072	65.471	2.85119	228.64599	81.0652	255.1800	11.0652	3.1800
31	-2	9	7	177	159	2	2	172	151	-117.072	166.471	2.18371	203.51512	177.9676	159.3138	5.9676	8.3138
32	-4	-2	13	188	440	2	2	184	445	-105.072	-127.529	-2.25995	165.23867	189.2363	438.5332	5.2363	-6.4668
33	10	-10	-28	590	360	2	2	604	361	314.928	-43.529	-0.13735	317.92201	588.1006	358.9894	-15.8994	-2.0106
34	6	-7	-17	474	366	2	2	483	368	193.928	-50.529	-0.25489	200.40272	473.2096	365.5555	-9.7904	-2.4445
35	10	-1	-28	538	160	2	2	549	152	259.928	165.471	0.56690	308.12846	535.9527	160.4570	-13.0473	8.4570
36	9	-8	-25	552	334	2	2	564	334	274.928	-16.529	-0.06005	275.42439	550.1343	333.3162	-13.8657	-0.6838
37	-2	-10	8	281	582	2	2	280	594	-9.072	-276.529	-1.60359	276.67793	280.3507	580.0973	0.3507	-13.9027
38	-6	-1	19	131	455	2	2	124	461	-165.072	-143.529	-2.42589	218.74505	132.2574	453.6987	8.2574	-7.3013
39	6	7	-16	389	56	2	2	393	44	103.928	273.471	1.20762	292.55311	387.8629	57.7982	-5.1371	13.7982
40	3	8	-8	311	88	2	2	312	78	22.928	239.471	1.47534	240.56595	310.9413	90.0517	-1.0587	12.0517
41	8	-2	-23	497	218	2	2	507	213	217.928	104.471	0.44702	241.67489	496.0600	218.3652	-10.9400	5.3652
42	-5	-7	17	186	571	2	2	182	582	-107.072	-264.529	-1.95540	285.37711	187.2974	568.6487	5.2974	-13.3513
43	7	5	-19	426	82	2	2	432	71	142.928	246.471	1.04529	284.91451	424.8881	83.4632	-7.1119	12.4632
44	5	-12	-13	472	497	2	2	481	505	191.928	-187.529	-0.77381	268.33473	471.2524	495.6761	-9.7476	-9.3239
45	5	9	13	351	30	2	2	354	17	64.928	300.471	1.35798	307.40587	350.8363	32.1316	-3.1637	15.1316
46	8	-5	-23	514	284	2	2	525	283	235.928	34.471	0.14508	238.43289	513.1251	284.8548	-11.8749	1.8548
47	-7	12	23	25	186	2	2	13	180	-276.072	137.471	2.67958	308.40558	26.9728	186.7538	13.9728	6.7538
48	8	-12	-22	550	441	2	2	562	447	272.928	-129.529	-0.44311	302.10507	548.1892	440.6420	-13.8108	-6.3580
49	8	3	-22	463	108	2	2	471	98	181.928	219.471	0.87866	285.07058	461.9115	109.1273	-9.0885	11.1273
50	4	6	-11	348	114	2	2	351	105	61.928	212.471	1.28719	221.31184	347.9675	115.7157	-3.0325	10.7157
51	-4	10	13	119	173	2	2	112	167	-177.072	150.471	2.43723	232.37036	120.9838	174.4749	8.9838	7.4749
52	9	1	-25	500	134	2	2	510	125	220.928	192.471	0.71667	293.00886	498.9331	134.7917	-11.0669	9.7917

Figure A.4. Excel sheet for the fitting between the experimental and simulated reflection positons observed on the NBDP of Al-hematite, along [301] ZA, in sample OL1. The refined lattice paramteres *a* and *c*, as well as the error are shown at the upper right.

The experimental and simulated 25 *hkl* reflection positions used for fitting the lattice parameter for Al-hematite in sample OL3 are shown in Figures A.5 and A.6.

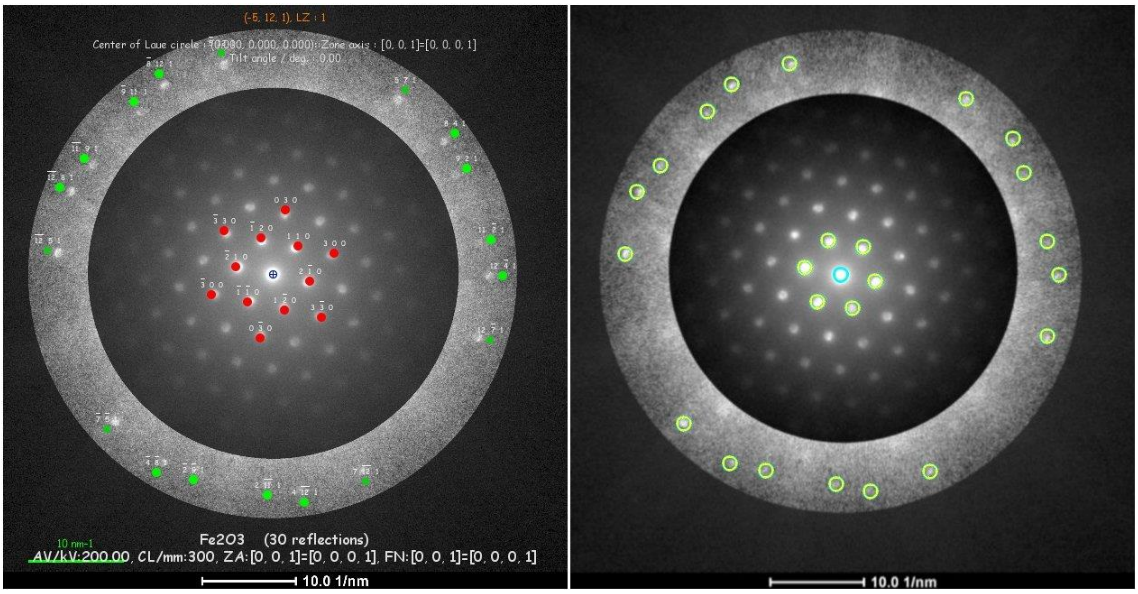

Figure A.5. NBDP patterns of the Al-hematite along <001> ZA, in sample OL3, taken at a camera length of 300 mm. At left, the NBDP showing the experimental (Exp) the correspondent simulated (Sim) *hkl* reflection positions. At right, the same experimental NBDP with the corrected *hkl* reflection positions centrered at the overlaid yellow circles.

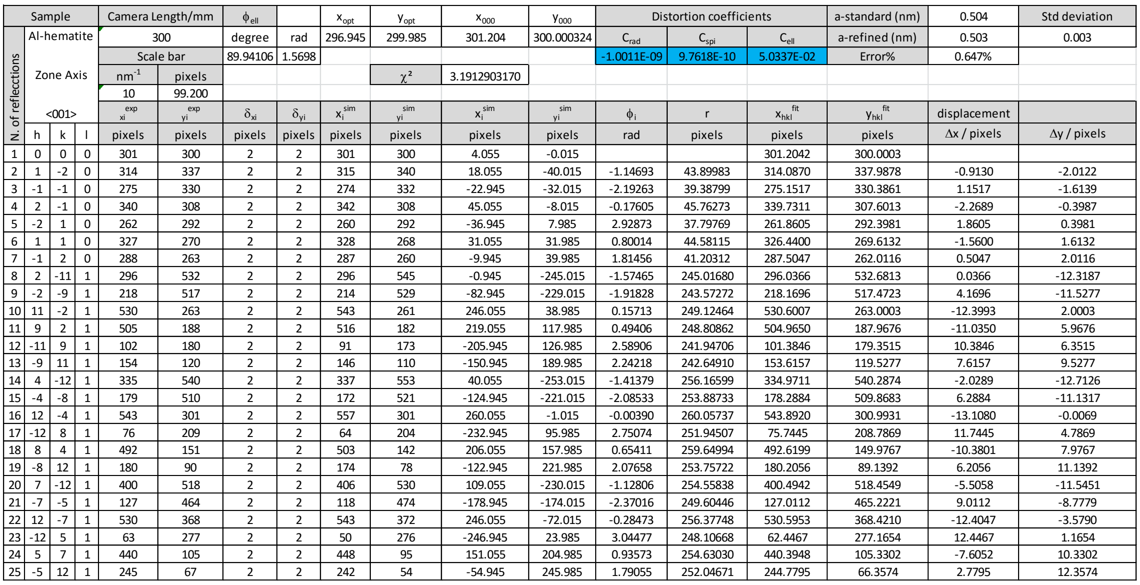

Sample				Camera Length/mm		ϕ_{ell}		x_{opt}	y_{opt}	x_{000}	y_{000}	Distortion coefficients			a-standard (nm)	0.504	Std deviation
N. of reflecctions	Al-hematite			300		degree	rad	296.945	299.985	301.204	300.000324	C_{rad}	C_{spi}	C_{ell}	a-refined (nm)	0.503	0.003
				Scale bar		89.94106	1.5698					-1.0011E-09	9.7618E-10	5.0337E-02	Error%	0.647%	
	Zone Axis			nm^{-1}	pixels				χ^2	3.1912903170							
				10	99.200												
	<001>			$_{xi}^{exp}$	$_{yi}^{exp}$	δ_{xi}	δ_{yi}	x_i^{sim}	$_{yi}^{sim}$	x_i^{sim}	$_{yi}^{sim}$	ϕ_i	r	x_{hkl}^{fit}	y_{hkl}^{fit}	displacement	
	h	k	l	pixels	pixels	pixels	pixels	pixels	pixels	pixels	pixels	rad	pixels	pixels	pixels	Δx / pixels	Δy / pixels
1	0	0	0	301	300	2	2	301	300	4.055	-0.015			301.2042	300.0003		
2	1	-2	0	314	337	2	2	315	340	18.055	-40.015	-1.14693	43.89983	314.0870	337.9878	-0.9130	-2.0122
3	-1	-1	0	275	330	2	2	274	332	-22.945	-32.015	-2.19263	39.38799	275.1517	330.3861	1.1517	-1.6139
4	2	-1	0	340	308	2	2	342	308	45.055	-8.015	-0.17605	45.76273	339.7311	307.6013	-2.2689	-0.3987
5	-2	1	0	262	292	2	2	260	292	-36.945	7.985	2.92873	37.79769	261.8605	292.3981	1.8605	0.3981
6	1	1	0	327	270	2	2	328	268	31.055	31.985	0.80014	44.58115	326.4400	269.6132	-1.5600	1.6132
7	-1	2	0	288	263	2	2	287	260	-9.945	39.985	1.81456	41.20312	287.5047	262.0116	0.5047	2.0116
8	2	-11	1	296	532	2	2	296	545	-0.945	-245.015	-1.57465	245.01680	296.0366	532.6813	0.0366	-12.3187
9	-2	-9	1	218	517	2	2	214	529	-82.945	-229.015	-1.91828	243.57272	218.1696	517.4723	4.1696	-11.5277
10	11	-2	1	530	263	2	2	543	261	246.055	38.985	0.15713	249.12464	530.6007	263.0003	-12.3993	2.0003
11	9	2	1	505	188	2	2	516	182	219.055	117.985	0.49406	248.80862	504.9650	187.9676	-11.0350	5.9676
12	-11	9	1	102	180	2	2	91	173	-205.945	126.985	2.58906	241.94706	101.3846	179.3515	10.3846	6.3515
13	-9	11	1	154	120	2	2	146	110	-150.945	189.985	2.24218	242.64910	153.6157	119.5277	7.6157	9.5277
14	4	-12	1	335	540	2	2	337	553	40.055	-253.015	-1.41379	256.16599	334.9711	540.2874	-2.0289	-12.7126
15	-4	-8	1	179	510	2	2	172	521	-124.945	-221.015	-2.08533	253.88733	178.2884	509.8683	6.2884	-11.1317
16	12	-4	1	543	301	2	2	557	301	260.055	-1.015	-0.00390	260.05737	543.8920	300.9931	-13.1080	-0.0069
17	-12	8	1	76	209	2	2	64	204	-232.945	95.985	2.75074	251.94507	75.7445	208.7869	11.7445	4.7869
18	8	4	1	492	151	2	2	503	142	206.055	157.985	0.65411	259.64994	492.6199	149.9767	-10.3801	7.9767
19	-8	12	1	180	90	2	2	174	78	-122.945	221.985	2.07658	253.75722	180.2056	89.1392	6.2056	11.1392
20	7	-12	1	400	518	2	2	406	530	109.055	-230.015	-1.12806	254.55838	400.4942	518.4549	-5.5058	-11.5451
21	-7	-5	1	127	464	2	2	118	474	-178.945	-174.015	-2.37016	249.60446	127.0112	465.2221	9.0112	-8.7779
22	12	-7	1	530	368	2	2	543	372	246.055	-72.015	-0.28473	256.37748	530.5953	368.4210	-12.4047	-3.5790
23	-12	5	1	63	277	2	2	50	276	-246.945	23.985	3.04477	248.10668	62.4467	277.1654	12.4467	1.1654
24	5	7	1	440	105	2	2	448	95	151.055	204.985	0.93573	254.63030	440.3948	105.3302	-7.6052	10.3302
25	-5	12	1	245	67	2	2	242	54	-54.945	245.985	1.79055	252.04671	244.7795	66.3574	2.7795	12.3574

Figure A.6. Excel sheet for the fitting between the experimental and simulated reflection positons observed on the NBDP of Al-hematite, along <001> ZA, in sample OL3. The refined lattice paramteres *a* and *c*, as well as the error are shown at the upper right.

As for Al-hematite crystal measured in samples OL1, the lattice parameter “c_i”, was determined for each i-th corrected *hlk* ($l \neq 0$) reflection position, by using the following Equation A.2 (keeping the a_{Std} value constant):

$$c_i = \sqrt{\frac{l^2}{\left[\frac{1}{d_{hkl}^2} - \frac{4}{3}\left(\frac{h^2+hk+k^2}{a_{Std}^2}\right)\right]}} \qquad \text{(Eq. A.2)}$$

The lattice parameter a_i for Al-hematite crystals measured in both samples OL1 and OL3, was determined for each i-th corrected *hk0* (i.e. $l = 0$) reflection position, by using the Equation A.3:

$$a_i = \sqrt{\frac{4d_{hk0}^2}{3}\left(h^2 + hk + k^2\right)} \qquad \text{(Eq. A.3)}$$

The results of the lattice parameters refinement are shown in Section 3.3.2 as well as in Figures A.4 and A.6. The presicions of the lattice parameter refinements were 0.62% and 0.65% errors for Al-hematite samples in samples OL1 and OL3, respectively.

Appendix 2. Additional TEM images from Oxisol samples

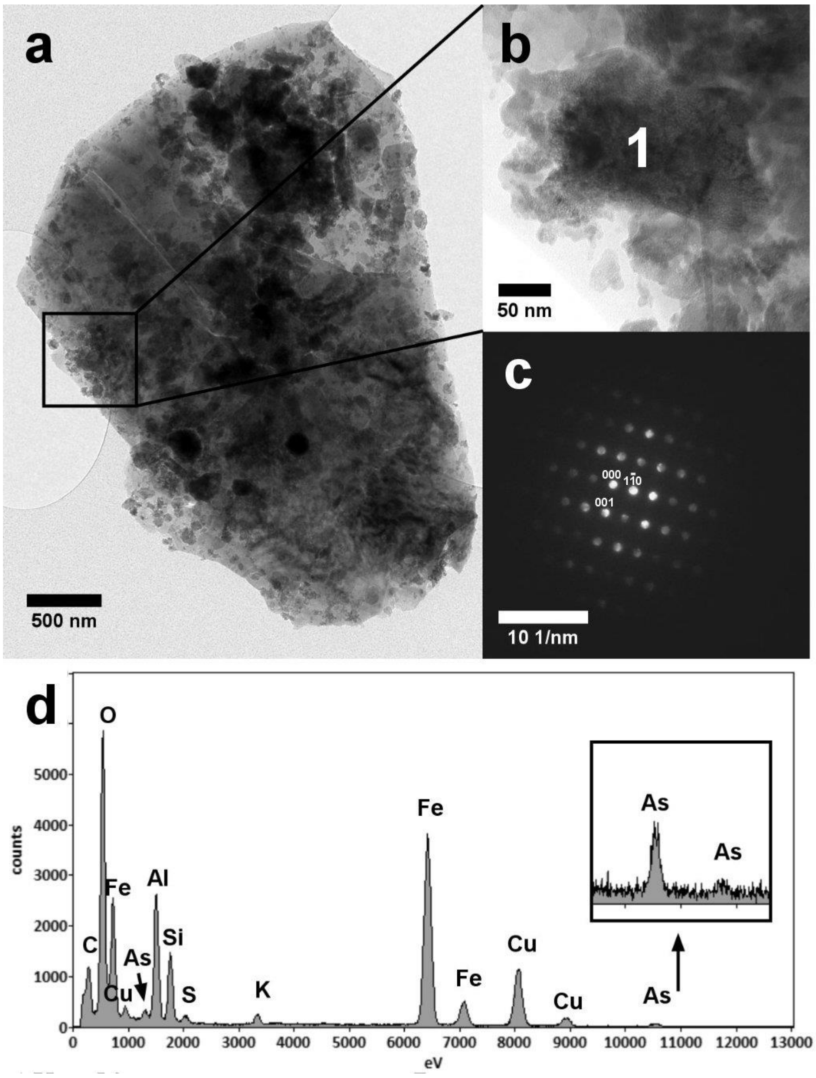

Figure A.7. (a) Brigh field TEM image of OL1 sample. (b-c) A mesocrystal of Al-goethite (1), and its correspondent NBDP along the [110] ZA. (d) The EDX spectrum taken at the point 1 indicated in image (b) shows the presence of As in the Al-goethite mesocrystal. The Si, S and K signal are due to X-ray emitted from the phyllosilicate crystal superimposed with the goethite. The C and Cu signals are from the Carbon-coated TEM Cu-support grid.

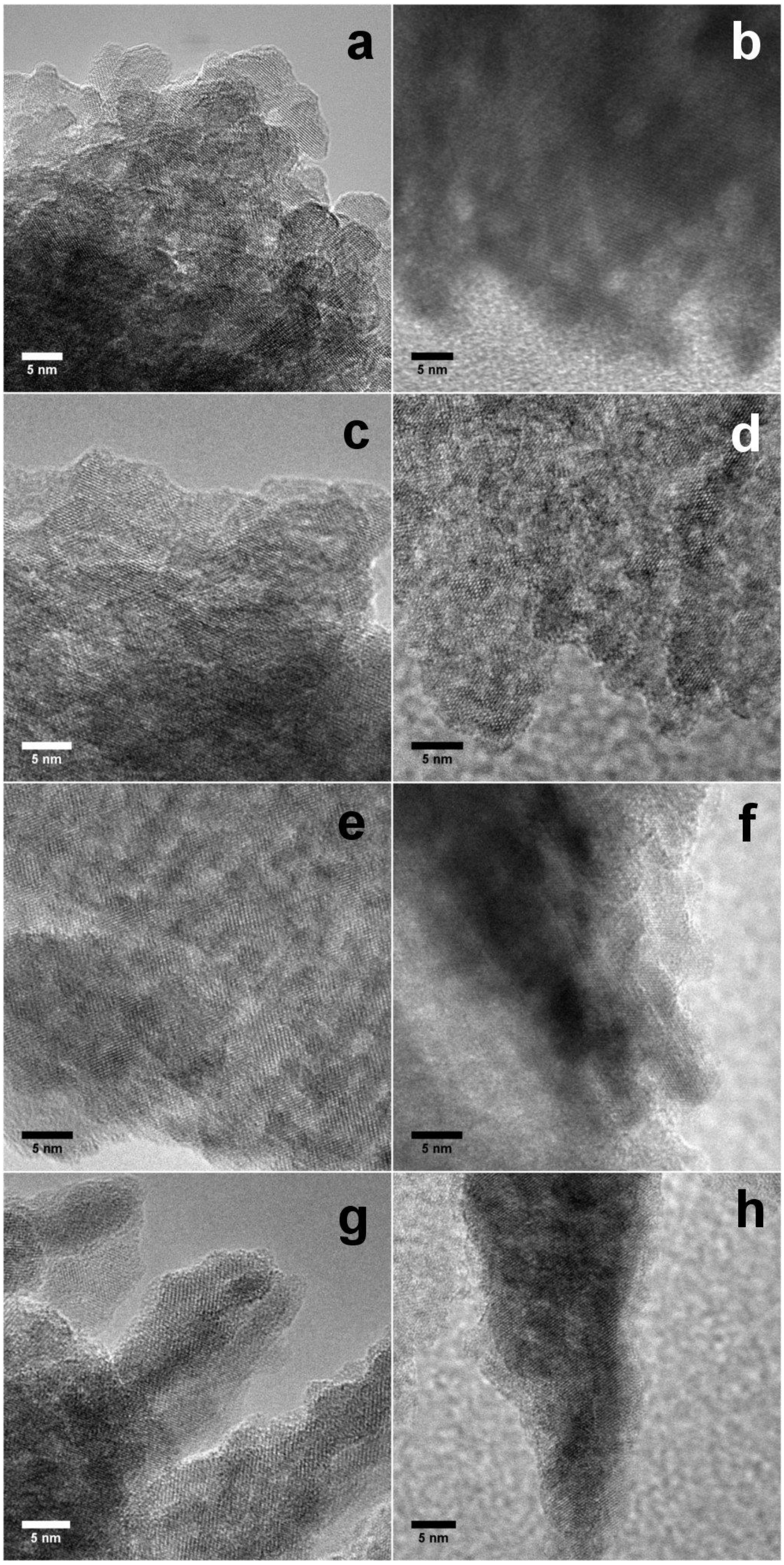

Figure A.8. HRTEM images of different oriented aggregates of As-bearing Al-Fe-(hydr)oxides in sample OL1.

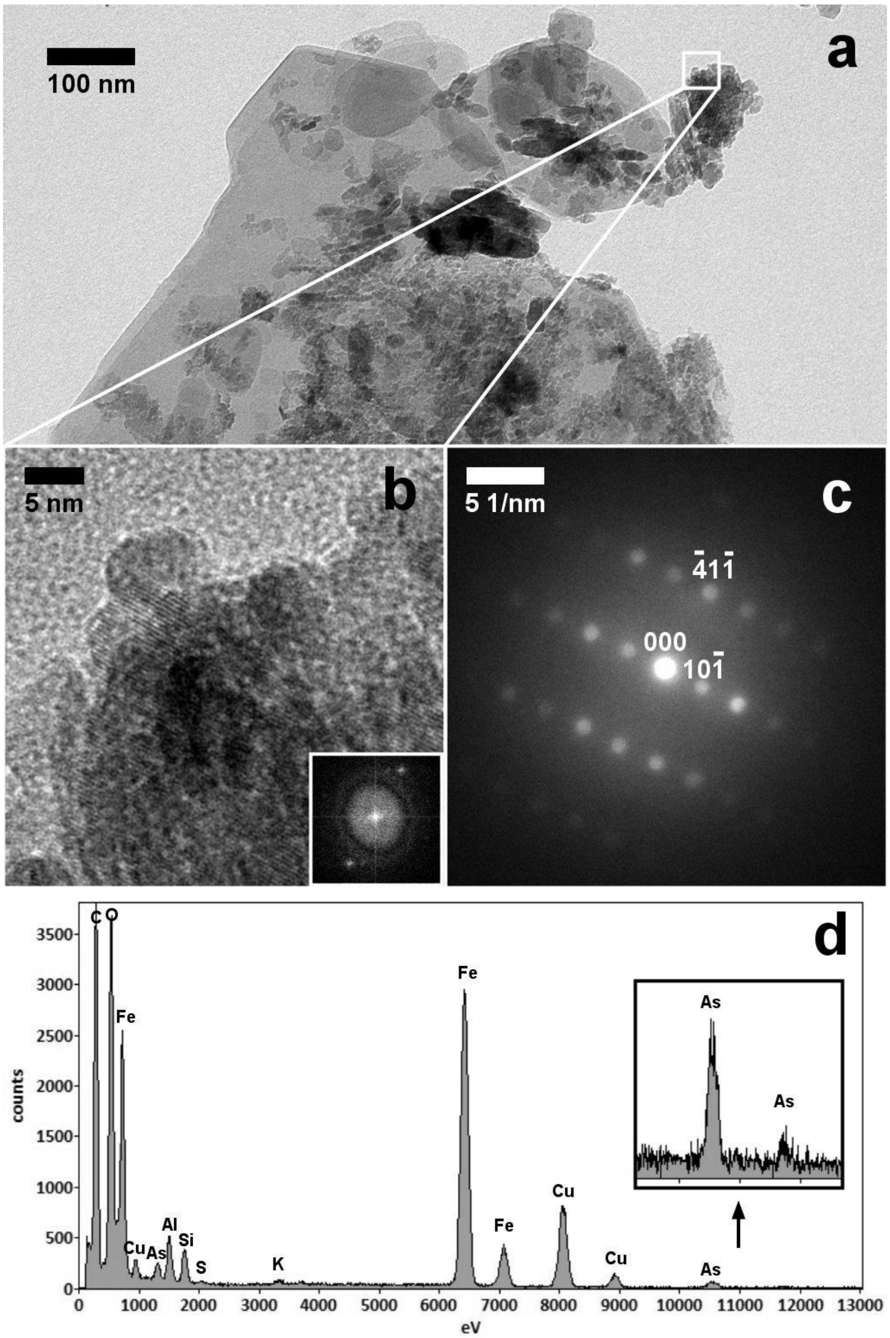

Figure A.9. (a) Bright field TEM image of sample OL3. (b) HRTEM image of an oriented aggregate of Al-goethite taken from the area inside the white square in (a). The FFT in the inset shows the lattice fringes observed on the HRTEM image. (c) NBDP of the oriented aggregate of Al-goethite along the [151] ZA. (d) EDX spectrum shown its chemical comsposition of the Al-goethite. The C and Cu signal are due to X-ray emitted from the Carbon-coated TEM Cu-support grid.

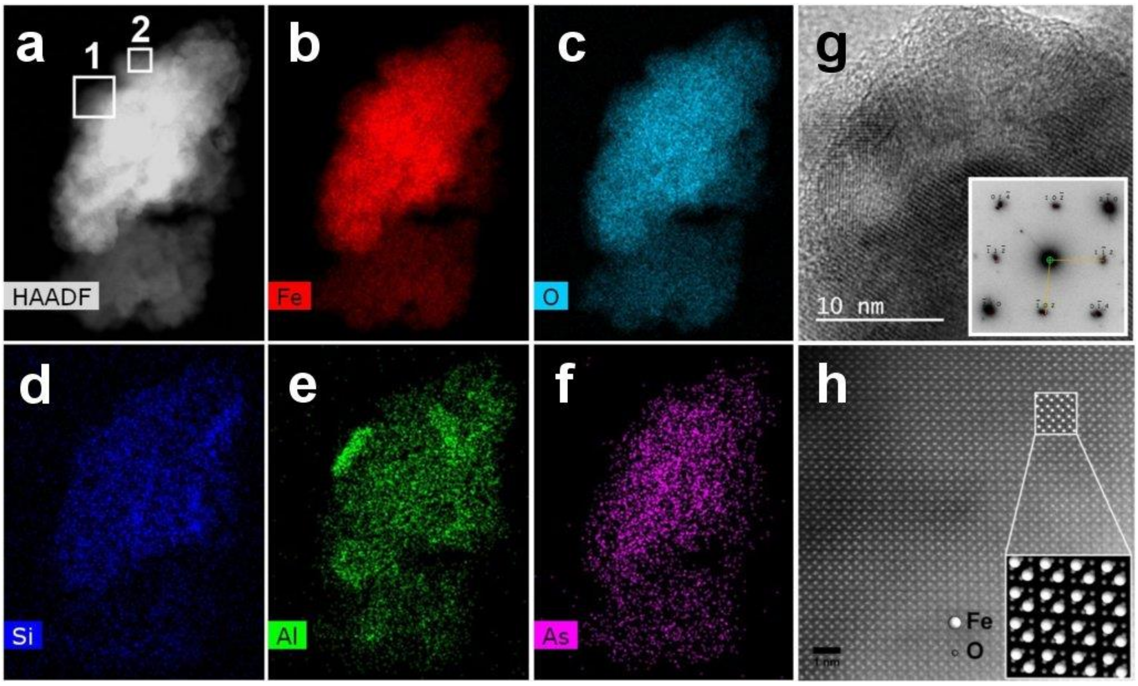

Figure A.10. (a) HAADF-STEM image of an oriented aggregate of Al-hematite in sample OL3. (b-f) EDS maps showing the chemical composition and distribution of each element in the aggregate. The segregation of Al shown in image (e) is likely due to an Al-oxide particle, as there is no significant Fe signal from the same area. The HRTEM image (g) and HR-STEM image (h) were taken from areas inside the white squares 1 and 2, respectively. The insets in images (g) and (h) show, repectively, the SADP and the simulated Fe and O atomic positons for hematite along the [241] ZA.

Appendix 3. Additional TEM images of As-Al-Fe co-precipitates

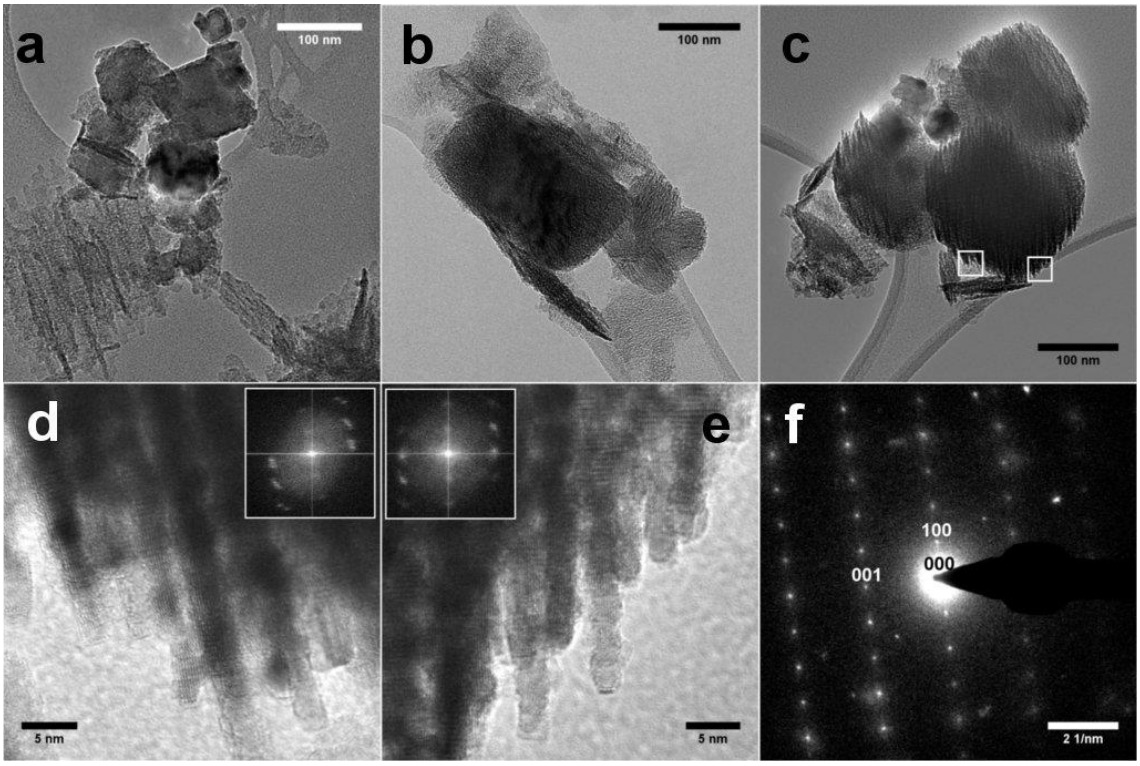

Figure A.11. (a-c) Bright field TEM images of mesocrystals of As-bearing Al-magnetite and Al-goethite in As-Al-Fe co-precipitated samples. The HRTEM images (d) and (e) were taken in the areas inside the white squares in (c). (f) SADP of Al-goethite along [010] ZA, taken from the darker, larger mesocrystal in (c). The 100 and 001 reflections are due to double diffraction events.

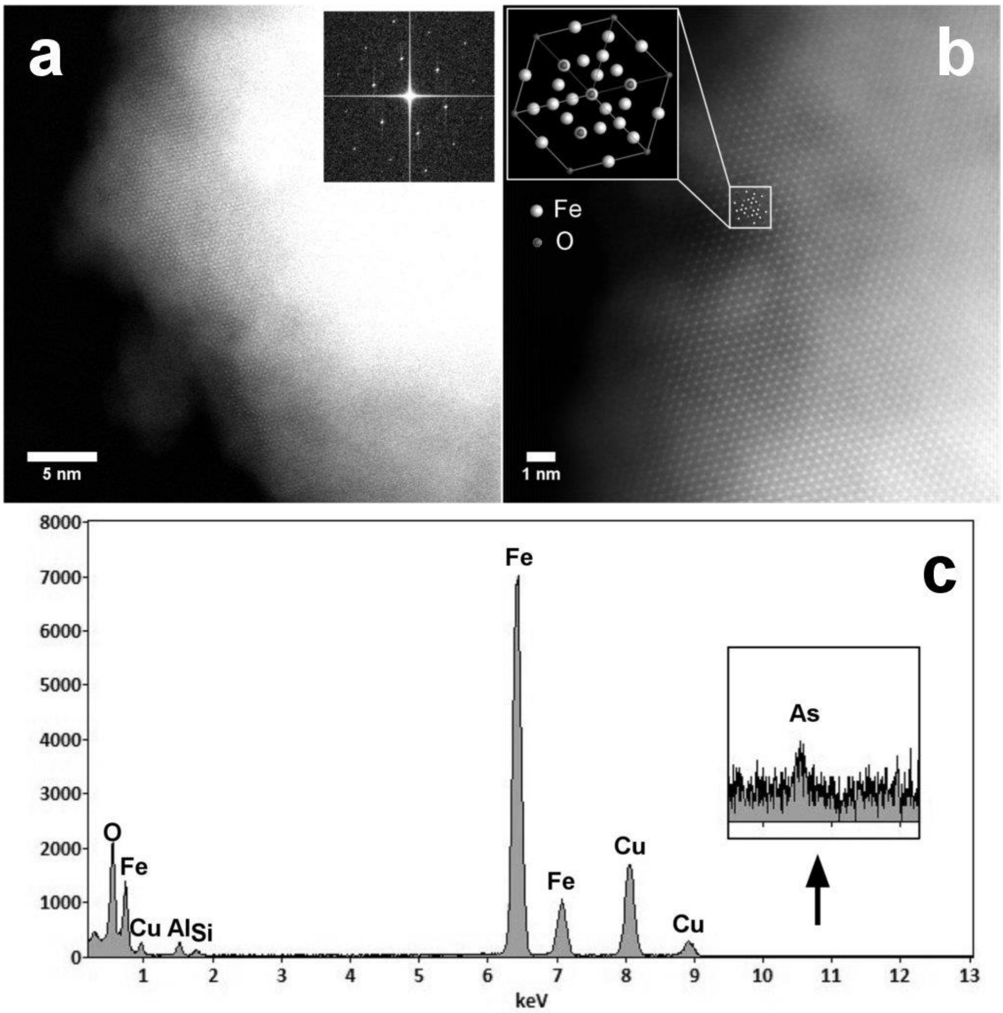

Figure A.12. (a) HRSTEM image of an oriented aggregate of As-bearing Al-magnetite. The FFT in the inset was taken from the whole image. (b) HRSTEM image of the same oriented aggregate at higher magnification. The inset shows the detailed simulated Fe and O atomic positions in a unit cell of magnetite along th <111> direction. (c) EDX spectrum showing the chemical composition of the aggregate and the presence of arsenic (As). The Cu signal is due to X-ray emitted from the TEM Cu-support grid.

Appendix 4. Additional information to the experiments of As adsorbed onto, and extracted from, Al-ferrihydrite

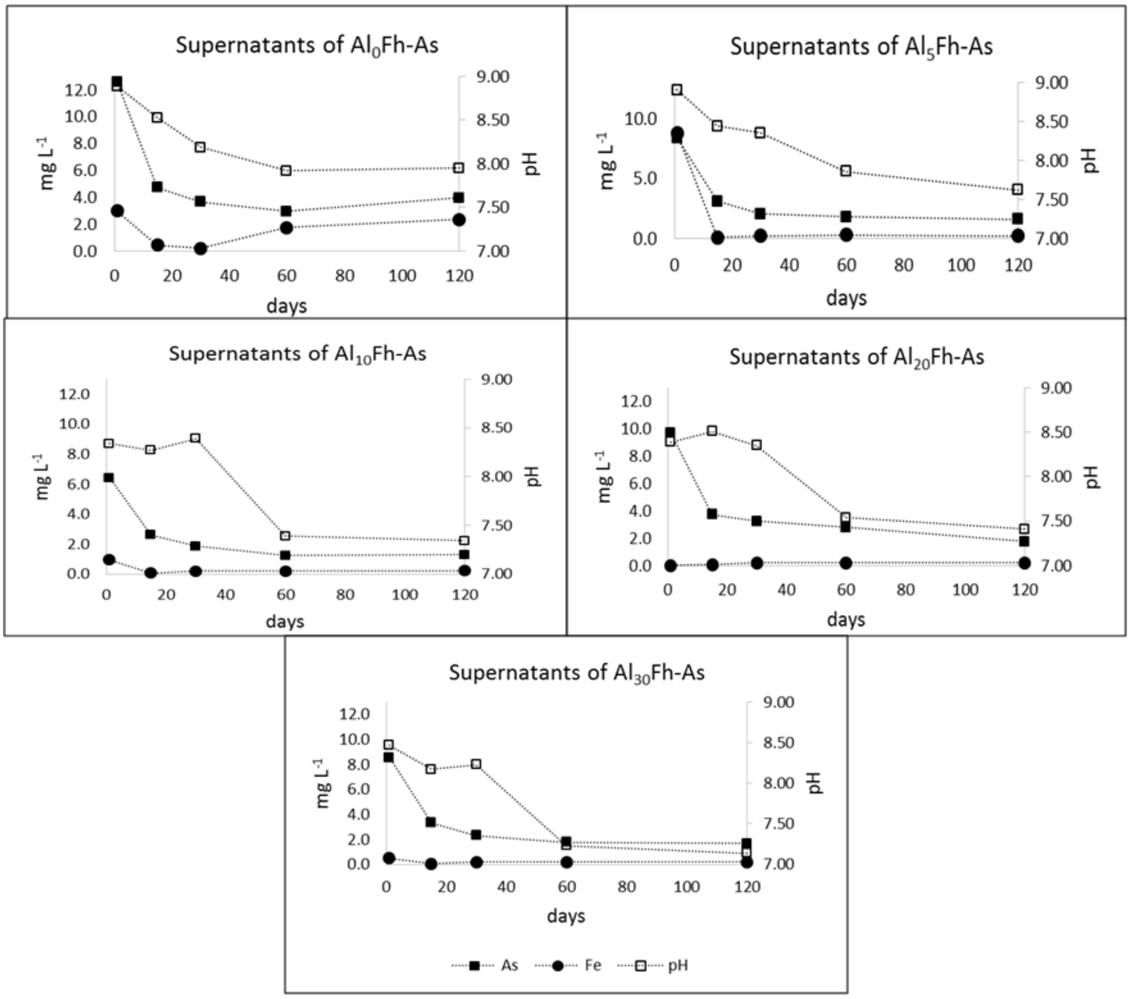

Figure A.13. Arsenic and iron concentrations (mg L^{-1}) in supernatants, and the pH, over the time for samples Al_RFh-As. R stands for the initial Al/(Al+Fe) molar ratio. The Al content was below the ICO-OES detection limit in all measurements.

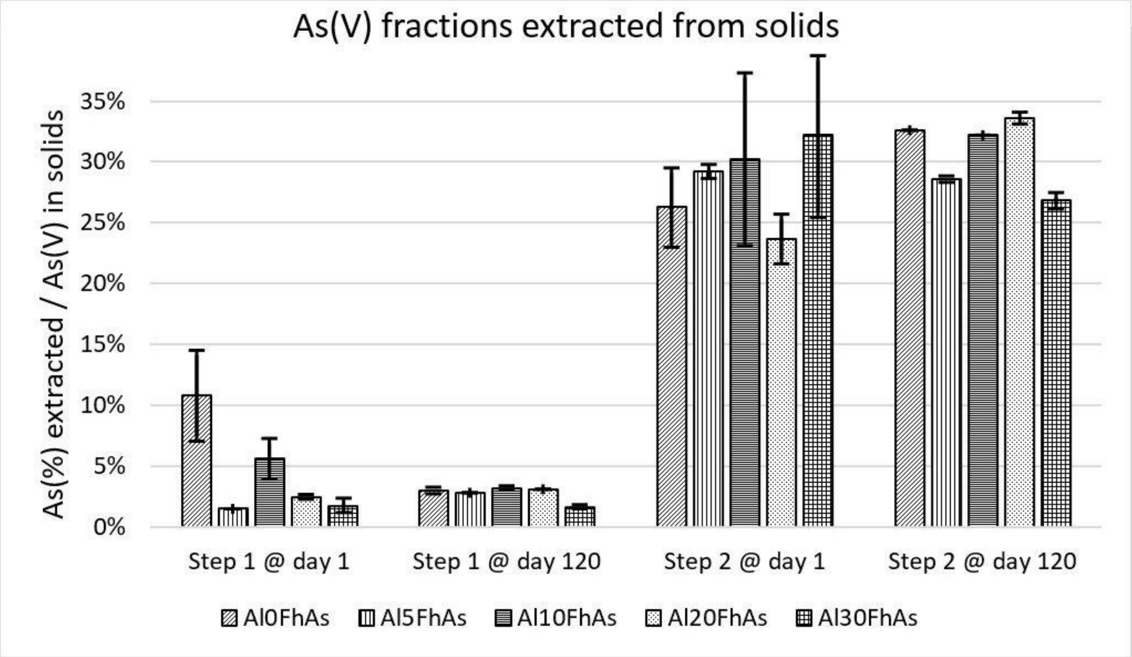

Figure A.14. Arsenic fractions extracted by water and by 0.2 mol L^{-1} phosphate, in steps 1 and 2, respectively, in the desorption experiments for samples Al_RFh-As. R stants for the initial Al/(Al+Fe) molar ratio in the formed ferrihydrite precipitates.